

Metal enrichment and evolution in four $z > 6.5$ quasar sightlines observed with JWST/NIRSpec

L. Christensen^{1,2} *, P. Jakobsen^{1,2}, C. Willott³, S. Arribas⁴, A. Bunker⁵, S. Charlot⁶, R. Maiolino^{7,8,9}, M. Marshall³, M. Perna⁴, and H. Übler^{7,8}

¹ Cosmic Dawn Center (DAWN), University of Copenhagen, Denmark

² Niels Bohr Institute, University of Copenhagen, Jagtvej 128, DK-2200 N, Copenhagen, Denmark

³ National Research Council of Canada, Herzberg Astronomy & Astrophysics Research Centre, 5071 West Saanich Road, Victoria, BC V9E 2E7, Canada

⁴ Centro de Astrobiología (CAB), CSIC-INTA, Ctra. de Ajalvir km 4, Torrejón de Ardoz, E-28850, Madrid, Spain

⁵ Department of Physics, University of Oxford, Denys Wilkinson Building, Keble Road, Oxford OX1 3RH, UK

⁶ Sorbonne Université, CNRS, UMR 7095, Institut d'Astrophysique de Paris, 98 bis bd Arago, 75014 Paris, France

⁷ Kavli Institute for Cosmology, University of Cambridge, Madingley Road, Cambridge, CB3 0HA, UK

⁸ Cavendish Laboratory, University of Cambridge, 19 JJ Thomson Avenue, Cambridge, CB3 0HE, UK

⁹ Department of Physics and Astronomy, University College London, Gower Street, London WC1E 6BT, UK

Received 12 September 2023; accepted 11 October 2023

ABSTRACT

We present JWST/NIRSpec $R \approx 2700$ spectra of four high-redshift quasars: VDES J0020–3653 ($z = 6.860$), DELS J0411–0907 ($z = 6.825$), UHS J0439+1634 ($z = 6.519$) and ULAS J1342+0928 ($z = 7.535$). The exquisite data quality, signal-to-noise ratio of 50–200, and large $0.86 \mu\text{m} \leq \lambda \leq 5.5 \mu\text{m}$ spectral coverage allows us to identify between 13 and 17 intervening and proximate metal absorption line systems in each quasar spectrum, with a total number of 61 absorption-line systems detected at $2.42 < z < 7.48$ including the highest redshift intervening O I $\lambda 1302$ and Mg II systems at $z = 7.37$ and $z = 7.44$. We investigate the evolution of the metal enrichment in the epoch of reionization (EoR) at $z > 6$ and find: *i*) A continued increase of the low-ionization O I, C II, and Si II incidence, *ii*) Decreasing high-ionization C IV and Si IV incidence with a transition from predominantly high- to low-ionization at $z \approx 6.0$, and *iii*) a constant Mg II incidence across all redshifts. The observations support a change in the ionization state of the intergalactic medium in the EoR rather than a change in metallicity. The abundance ratio of [Si/O] in five $z > 6$ absorption systems show enrichment signatures produced by low-mass Pop III pair instability supernovae, and possibly Pop III hypernovae. In the Gunn-Peterson troughs we detect transmission spikes where Ly α photons can escape. From 22 intervening absorption line systems at $z > 5.7$, only a single low-ionization system out of 13 lies within 2000 km s^{-1} from a spike, while four high-ionization systems out of nine lie within $\sim 2000 \text{ km s}^{-1}$ from a spike. Most spikes do not have associated metal absorbers close by. This confirms that star-forming galaxies responsible for producing the heavy elements that are transported to the circumgalactic medium via galaxy winds do so in predominantly high-density, neutral environments, while lower density environments are ionized without being polluted by metals at $z \approx 6 - 7$.

Key words. Cosmology: observations – (Cosmology:) dark ages, reionization, first stars – (galaxies:) quasars: absorption lines – Galaxies: high-redshift – (galaxies:) intergalactic medium

1. Introduction

Investigations of high redshift quasars contribute significantly to our knowledge of the physical conditions in the early Universe, including the growth of supermassive black holes (SMBH) and their co-evolution with galaxies, and their effect on the reionization history of the Universe. Quasars also serve as bright beacons to illuminate the baryonic material along their lines of sight since their high luminosity allow their detection to very large distances. Finding high-redshift quasars has been the focus of numerous scientific investigations. From color selection of sources in large imaging surveys (e.g. Fan et al. 2001; Willott et al. 2010; Wang et al. 2019; Matsuoka et al. 2022; Bañados et al. 2023), hundreds of quasars beyond redshift 6 have been discovered and compiled in databases (Inayoshi et al. 2020; Fan et al. 2023), while beyond redshift 7 only eight quasars have been discovered

to date (Mortlock et al. 2011; Bañados et al. 2018; Matsuoka et al. 2019b,a; Yang et al. 2019, 2021; Wang et al. 2018, 2021).

Spectra of quasars allow detailed studies of intervening baryonic material from absorption lines arising either in the environment near quasars as well as along random lines of sight through the Universe, and are invaluable probes to analyse the intergalactic medium (IGM) and the epoch of reionization (EoR). Due to the rapid decrease in quasar number densities compared to galaxies at the highest redshifts, quasars contribute only $< 7\%$ of the reionizing photon budget at $z \sim 6 - 6.6$ (Jiang et al. 2022). The neutral IGM will appear as a damping wing at the red part of the Ly α absorption in quasar spectra (Miralda-Escudé 1998), and the shape of this damping wing in quasar spectra at different redshift can be used to compute the neutral gas fraction $X_{\text{H I}}$ as the reionization progresses (Bañados et al. 2018; Davies et al. 2018, 2020). A complete absorption by the IGM in the Gunn-Peterson absorption trough (GP hereafter) (Gunn & Peterson 1965) detected in $z > 6$ quasar spectra (Fan et al. 2001; Mortlock et al.

* e-mail: lichrist@nbi.ku.dk

2011) reveals an increase in the Ly α optical depth with increasing redshift (Becker et al. 2021).

In the otherwise dark regions of the GP troughs, transmission spikes in the IGM start appearing at $z \lesssim 6$ where ionized regions allow the transmission of Ly α photons at those redshifts. Such spikes therefore need to lie near sources that produce ionizing radiation. Kakiichi et al. (2018) and Meyer et al. (2020) investigated the correlation between Ly α forest transmission spikes and location of Ly α -emitters and galaxies within a distance of 60 Mpc from the line of sight towards $z > 6$ quasars, and argue that reionization is primarily driven by a population of galaxies that are fainter than the detected galaxies.

Besides probing the EoR through studies of hydrogen absorption, quasar spectra can be used to measure the evolution of heavy element enrichment with cosmic time from intervening absorption line systems to $z \sim 6$ (see Becker et al. 2015, for a review of metal absorption lines). Quasars probe random lines of sight through the Universe, and intersect galaxies either in their circumgalactic medium (CGM) or interstellar medium (ISM) out to the quasar redshift, all of which imprint a spectral signature in the background quasar spectrum.

While the metallicity on the average increases with time, metal absorption lines also reflect the ionization state and are therefore sensitive to the ultraviolet background radiation. Early analyses of the Ly α forest clouds and their correlations with C IV $\lambda\lambda 1548, 1550$ absorption lines revealed that the IGM at $z = 3$ is enriched to a metallicity level of $\approx 10^{-3} Z_{\odot}$ (Cowie et al. 1995; Ellison et al. 2000). While metals seem to be prevalent, absorption line densities¹, defined as the number of absorption line systems detected per unit (comoving) redshift path length interval, can be used to map the evolution of the metal enrichment and ionization level. For example, C IV absorber line densities remain roughly constant with redshift out to $z \sim 4$ and then show a steep drop at $z > 5$ (Becker et al. 2011; Codoreanu et al. 2018; D’Odorico et al. 2022; Davies et al. 2023b). A similar trend is found for the other high-ionization line Si IV (Cooper et al. 2019; D’Odorico et al. 2022), suggesting a rapid physical change in the ionization state at these redshifts. The change of ionization state rather than a change in metal enrichment is supported from the observation of a change in the C IV/C II $\lambda 1334$ ratio (Simcoe et al. 2020; Davies et al. 2023b). Similarly, the line density of weak Mg II $\lambda 2796$ absorbers remain constant over a large redshift range of $2 < z < 7$ (Chen et al. 2017), whereas the line density of O I $\lambda 1302$ increases over the range $3.2 < z < 6.5$ (Becker et al. 2011, 2019) and is also interpreted as a change in the ionization state at the EoR, where the Universe becomes progressively more neutral.

Bright quasars also allow detailed analyses of individual absorption systems by measuring column densities of various atomic species, similar to studies of $2 < z < 3$ strong hydrogen absorption line systems (e.g. Prochaska et al. 2003). Focusing on the highest redshift absorbers at $z > 6$, this epoch approaches the time when the first population of massive stars produce the initial chemical enrichment. However, for intervening absorption lines systems the absence of measurable H I column densities in the quasars heavily absorbed Ly α forest or GP troughs makes it impossible to derive absolute metallicities, and only a few studies of relative metallicities at $z > 6$ have been performed to date. One example is the $z \sim 7.5$ quasar ULAS J1342+0928 whose absorption system at $z = 6.84$ with measured iron, carbon and

silicon suggests no alpha-element enhancement nor any special signatures of enrichment from very massive stars (Simcoe et al. 2020). When the absorption system lies close to the quasar redshift, in the so-called associated or proximate absorption systems, detailed metallicity measurements can be performed since the intrinsic H I column density can be modelled from fits to the H I damping wing (Bañados et al. 2019; Andika et al. 2022). However, proximate absorption systems do not trace a random population, but rather probe the high-density environments near the quasars (Ellison et al. 2010).

The connection between galaxies in emission and gas in absorption inform us of the transverse metal enrichment in the CGM of galaxies, albeit only along a single line of sight to the background quasar. Hence, combining the observations with simulations will reveal the spatial distribution of metals in the CGM of galaxies and its evolution with redshift (e.g. Finlator et al. 2018; Peebles et al. 2019). At $z \geq 5$ overdensities of line emitting galaxies either selected via Ly α emission (Díaz et al. 2021) or [O III] $\lambda 5007$ (Kashino et al. 2023) have been found within 200 kpc of the metal absorbers and approximately at the same redshifts.

Large amounts of ground-based telescope time have in recent years been devoted to spectroscopic studies of $z > 6$ quasars (e.g. D’Odorico et al. 2023). However, with the successful launch and commissioning of the James Webb Space Telescope (Gardner et al. 2023; Rigby et al. 2023), the question arises of what new insights observations of high redshift quasars obtained with JWST’s near infrared spectrograph, NIRSpec (Jakobsen et al. 2022), may bring to bear on the subject matter. While the highest spectral resolution possible with NIRSpec of $R \approx 2700$ is only just adequate for intervening absorption line studies, the benefits offered by the instrument’s very high sensitivity and wide ($0.81 \mu\text{m} \leq \lambda \leq 5.3 \mu\text{m}$) infrared spectral coverage free of the atmospheric telluric absorption and OH sky emission lines that hamper ground based near-IR observations are self-evident.

In this paper, we present high signal-to-noise ratio $R \approx 2700$ JWST/NIRSpec spectra of four well-studied quasars at $6.5 < z < 7.5$. We focus our analysis exclusively on the intervening absorption line systems detected. The paper is organised as follows. Section 2 describes the observations. The spectra are presented and analysed in Section 3. The measurements of metal absorption line systems and the redshift evolution of line densities of atomic transitions in oxygen, carbon, silicon and magnesium, calcium and sodium are discussed in Section 4. In Section 5 we compute metal abundance patterns and compare with the enrichment of Population III and Pop II massive star Supernova explosions, and in Section 6 we compare the metal absorption system redshifts with transmission spikes seen in the quasar GP troughs. In Section 7 we present a discussion and conclude in Section 8. Throughout the paper we assume a flat cosmological model with $H_0 = 67.4 \text{ km s}^{-1} \text{ Mpc}^{-1}$ and $\Omega_m = 0.315$ (Planck Collaboration et al. 2020).

2. NIRSpec observations

In this paper we present high signal-to-noise ratio ($S/N \approx 50 - 200$), $R \approx 2700$ NIRSpec spectra spanning $0.86 \mu\text{m} \leq \lambda \leq 5.3 \mu\text{m}$ of the four high redshift quasars: ULAS J1342+0928 (Bañados et al. 2018, $z = 7.54$, $J_{AB} = 20.3$), VDES J0020–3653 (Reed et al. 2019, $z = 6.83$, $J_{AB} = 20.4$), DELS J0411–0907 (a.k.a VHS J0411–0907, Pons et al. 2019; Wang et al. 2019, $z = 6.81$, $J_{AB} = 20.4$) and UHS J0439+1634 (Fan et al. 2019, $z = 6.51$, $J_{AB} = 17.4$). These data were obtained as part of the NIR-

¹ Line densities are also commonly called ‘incidence rate’ or simply ‘number densities’ in the literature. These terms are identical in their definition.

Table 1. Observation Epochs and Slit Orientations

Quasar	Mode	Date	PA [deg]
ULAS J1342+0928	FS	31 Jan 2023	66.8
	IFU	23 Jan 2023	55.1
VDES J0020–3653	FS	19 Nov 2022	187.2
	IFU	16 Oct 2022	160.2
	IFU	17 Nov 2022	189.2
DELS J0411–0907	FS	18 Sep 2022	50.6
	IFU	1 Oct 2022	61.9
UHS J0439+1634	FS	24 Jan 2023	210.8
	IFU	18 Jan 2023	210.4

Spec GTO programs 1219 (PI: N. Lützgendorf) and 1222 (PI: C. Willott).

The NIRSpec Band I ($0.86 \mu\text{m} \leq \lambda \leq 1.88 \mu\text{m}$) and Band II ($1.70 \mu\text{m} \leq \lambda \leq 3.15 \mu\text{m}$) spectra were taken with the NIRSpec Fixed Slits together with the G140H/F070LP and G235H/F170LP grating/filter combinations, whereas the long wavelength Band III ($2.88 \mu\text{m} \leq \lambda \leq 5.3 \mu\text{m}$) portions were obtained employing the NIRSpec Integral Field Unit (IFU) and the G395H/F290LP grating/filter combination (see Jakobsen et al. (2022) and Böker et al. (2022) for details of these NIRSpec observing modes). The dates on which the observations were carried out and the position angles of the slits employed are summarized in Table 1.

The Band I and Band II Fixed Slit observations all employed 65 group NRSIRS2RAPID (Rauscher et al. 2017) full frame detector sub-integrations. For ULAS J1342+0928, VDES J0020–3653, and DELS J0411–0907, spectra were obtained in both the S200A1 and S200A2 fixed slits in order to span the detector gap, with two integrations carried out in each of three nodded positions along the slit for G140H/F070LP (11554 s total exposure time) and one integration at each nod in G235H/F170LP (5778 s total exposure time). The brighter UHSJ0439+1634 was only observed in the S200A1 slit at three nodded integrations in both G140H/F070LP and G235H/F170LP (2889 s total exposure time). These data were reduced and combined using the NIRSpec GTO Team pipeline (Carniani et al. in preparation). The resulting flux-calibrated spectra refer to Barycentric vacuum wavelengths sampled at $\Delta\lambda = 2.36 \text{ \AA}$ per wavelength bin in Band I and $\Delta\lambda = 3.96 \text{ \AA}$ per wavelength bin in Band II, which by design is close to the average native pixel sampling for these dispersers.

One noteworthy aspect of the shortest wavelength Band I G140H observations is that they were taken with the F070LP order-separation filter, rather than the default F100LP filter. This was done to include wavelengths in the Gunn-Peterson troughs below emitted Ly α down to $0.813 \mu\text{m}$ with the S200A1 slit and down to $0.858 \mu\text{m}$ with the S200A2 slit. This is permissible in this case since there is little or no light from the quasar emerging in the trough and therefore no second order light (beyond that of the sky background, which is subtracted out in the reduction) to contaminate the primary first order spectrum at wavelengths $\lambda > 1.26 \mu\text{m}$. However this choice did require tricking the pipeline into reducing the full Band I spectrum in two steps. First by running it for the F070LP filter giving the correctly reduced spectrum over $0.85 \mu\text{m} \leq \lambda \leq 1.26 \mu\text{m}$ and then running it a second time pretending that the F100LP filter was used and then scaling the resulting red end of the spectrum covering the $1.0 \mu\text{m} \leq \lambda \leq 1.88 \mu\text{m}$ region by the known ratio of the trans-

mission of the F070LP and F100LP filters. The latter correction amounts to less than 4% in flux.

The Band III G395H/F290LP IFU observations of ULAS J1342+0928, VDES J0020–3653, and DELS J0411–0907 employed 25 group NRSIRS2 sub-integrations at 6 dithered IFU positions (11029 s total integration time) and UHSJ0439+1634 18 group NRSIRS2 integrations at 8 dithered positions (10620 s total integration time). The IFU observations of VDES J0020–3653, and DELS J0411–0907 are presented in Marshall et al. (2023), who along with Perna et al. (2023) also provide the details of how the IFU data were reduced. Here we merely employ the one dimensional G395H/F290LP spectra extracted from the four IFU data cubes over a $1''.0$ diameter aperture centered on the quasars to supplement the corresponding Band I and II Fixed Slit spectra of primary interest. The resulting Band III spectra are sampled at $\Delta\lambda = 6.65 \text{ \AA}$ per wavelength bin.

The final combined one-dimensional spectra of the quasars along with their 1σ error spectra are shown in Figures 1, 2, 3, and 4. The signal-to-noise ratios achieved in these four spectra are very high. This is illustrated for the representative case of VDES J0020–3653 in Figure 5. The lower panel plots the Band I and II signal-to-noise ratio per wavelength bin calculated as the ratio of the observed signal divided by the one sigma error spectrum output by the GTO pipeline after median smoothing over a 40 bin window to remove the absorption lines. It is apparent that $S/N \approx 50 - 100$ per wavelength bin is achieved at nearly all wavelengths. The overall variation with wavelength seen in this plot partly reflects the blaze functions of the two gratings employed and the variation in the continuum flux due to the broad emission lines in the quasar spectrum, but also the fact that not all wavelengths are exposed equally due to the gap between the two NIRSpec detector arrays. When employing the G140H grating with the S200A1 fixed slit the wavelength span $1.3021 - 1.3391 \mu\text{m}$ falls on the detector gap. For the S200A2 fixed slits the wavelength range $1.3479 - 1.3849 \mu\text{m}$ is lost to the gap. Similarly, for the G235H grating respectively $2.1825 - 2.2445 \mu\text{m}$ and $2.2594 - 2.3215 \mu\text{m}$ project to the gap for the S200A1 and S200A2 slits. Moreover, with the S200A1 slit, the G235M spectrum falls off the red edge of the detector for $\lambda > 3.0491 \mu\text{m}$ but for $\lambda > 3.1262 \mu\text{m}$ for the S200A2 slit. These unavoidable wavelength regions of reduced S/N only covered in one of the two slit spectra are indicated in Figure 5.

The high S/N ratio observations of the bright ($J_{AB} \approx 20$) quasars presented here represent a radically different and rarer regime of applicability for NIRSpec compared to the perhaps more familiar lower spectral resolution observations of the much fainter ($J_{AB} \approx 26 - 29$) highest redshift galaxies that the instrument was primarily designed for (cf. Curtis-Lake et al. 2023; Bunker et al. 2023). It is therefore worth pointing out a few further subtle quirks of NIRSpec revealed by these data that are usually masked at lower S/N ratio.

While NIRSpec grating observations of faint high redshift galaxies are invariably severely detector noise limited (cf. Appendix in Jakobsen et al. 2022), the photon noise in our quasar spectra typically exceeds the total detector read noise and dark current noise by a factor ≈ 4 . Furthermore, the quasar photon signals typically exceeds that of the (zodiacal light dominated) sky background experienced by JWST by a factor ≈ 20 . However, one important feature that these quasar spectra still share with their fainter counterparts is that they are rather coarsely sampled both in wavelength and spatially along the slit. As explained in Jakobsen et al. (2022), with the aim of optimizing the faint-end sensitivity limit of NIRSpec, the 194 mas angular

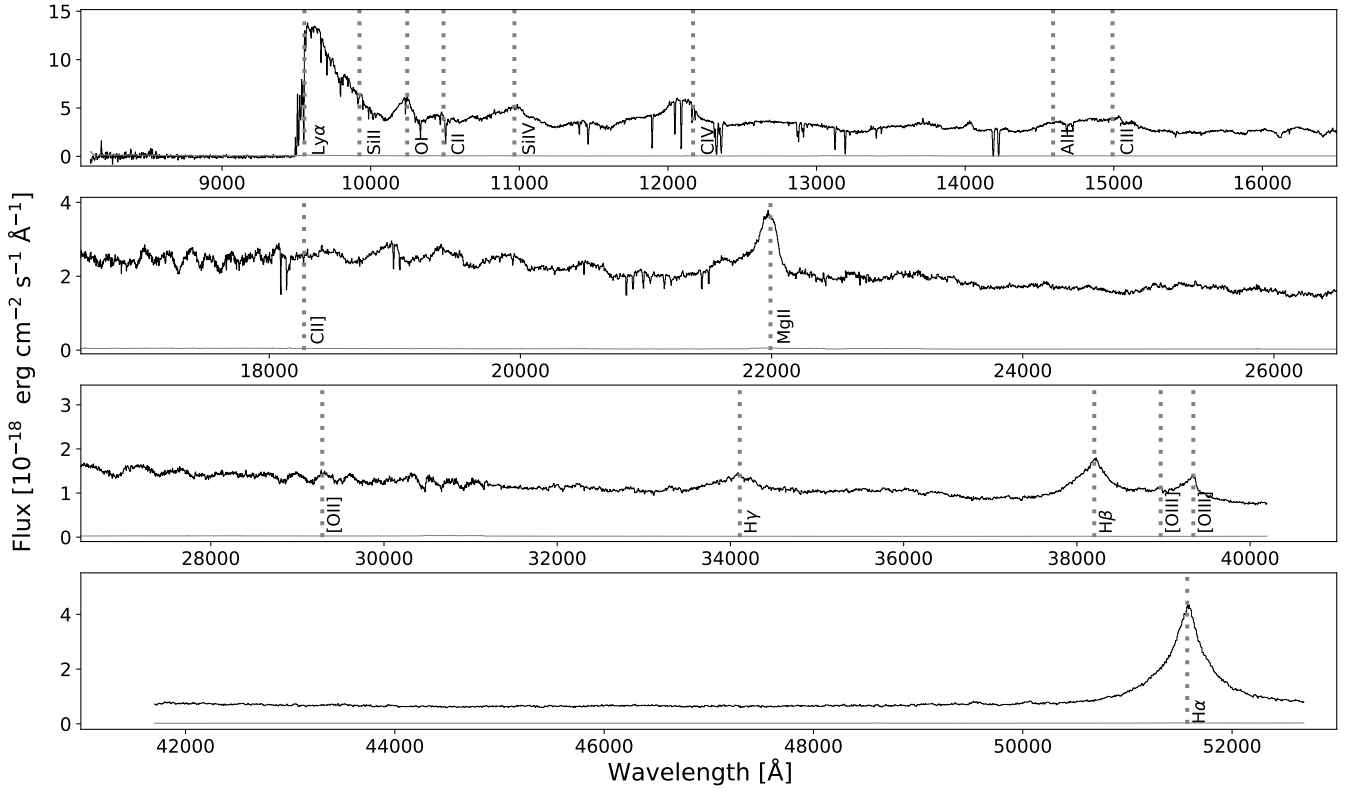


Fig. 1. NIRSpect fixed slit ($\lambda < 31160 \text{ \AA}$) and extracted 1D spectrum from the Band III data ($\lambda > 31160 \text{ \AA}$) of VDES J0020–3653. The modulation of the flux, which is particularly pronounced around ~ 18000 and $\sim 30000 \text{ \AA}$ here and also the other quasar spectra, is caused by the coarse sampling of the spectrum described in Sect. 2. The associated error spectrum is shown in gray. With the very high S/N ratio of the spectrum, the error spectrum appears virtually at the zero-flux level.

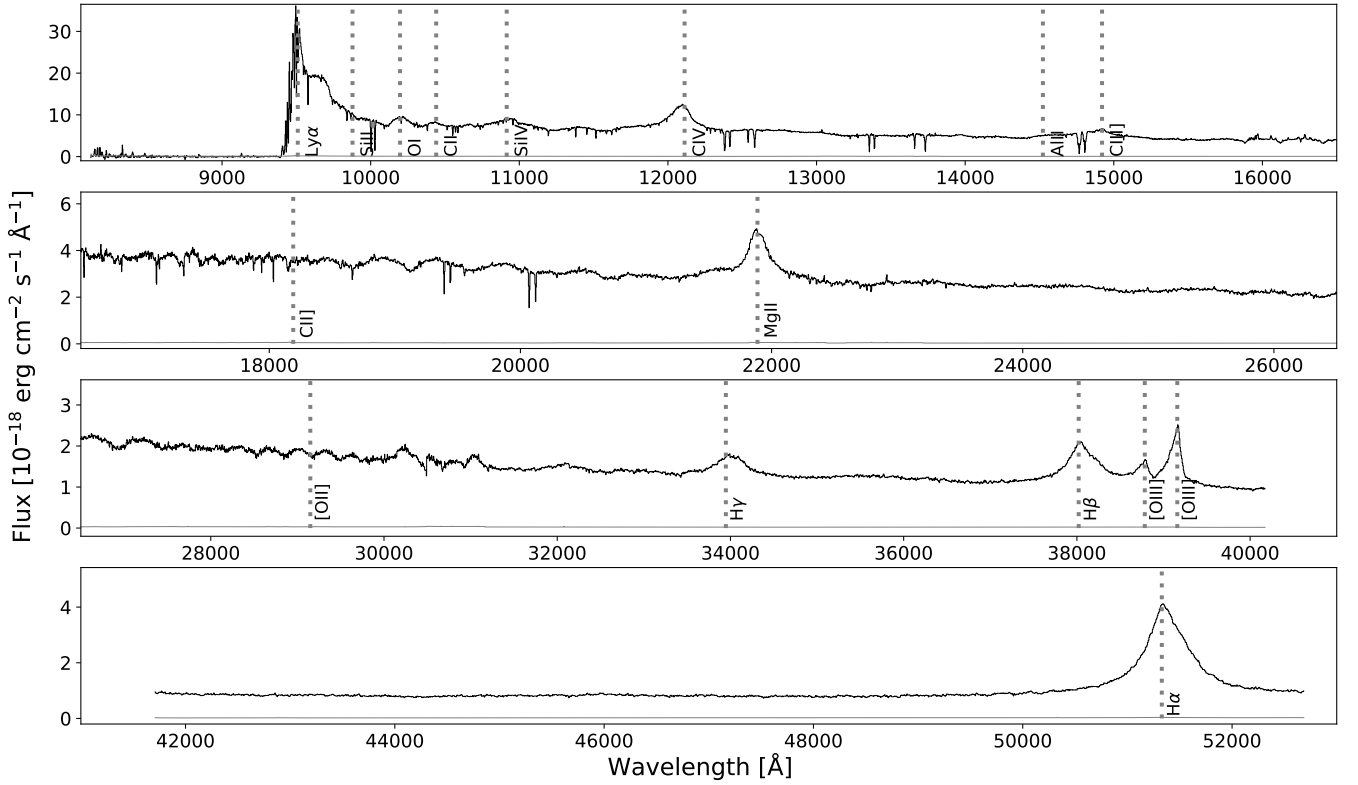


Fig. 2. NIRSpect fixed slit and extracted 1D spectrum from Band III data ($\lambda > 31160 \text{ \AA}$) of DELS J0411–0907.

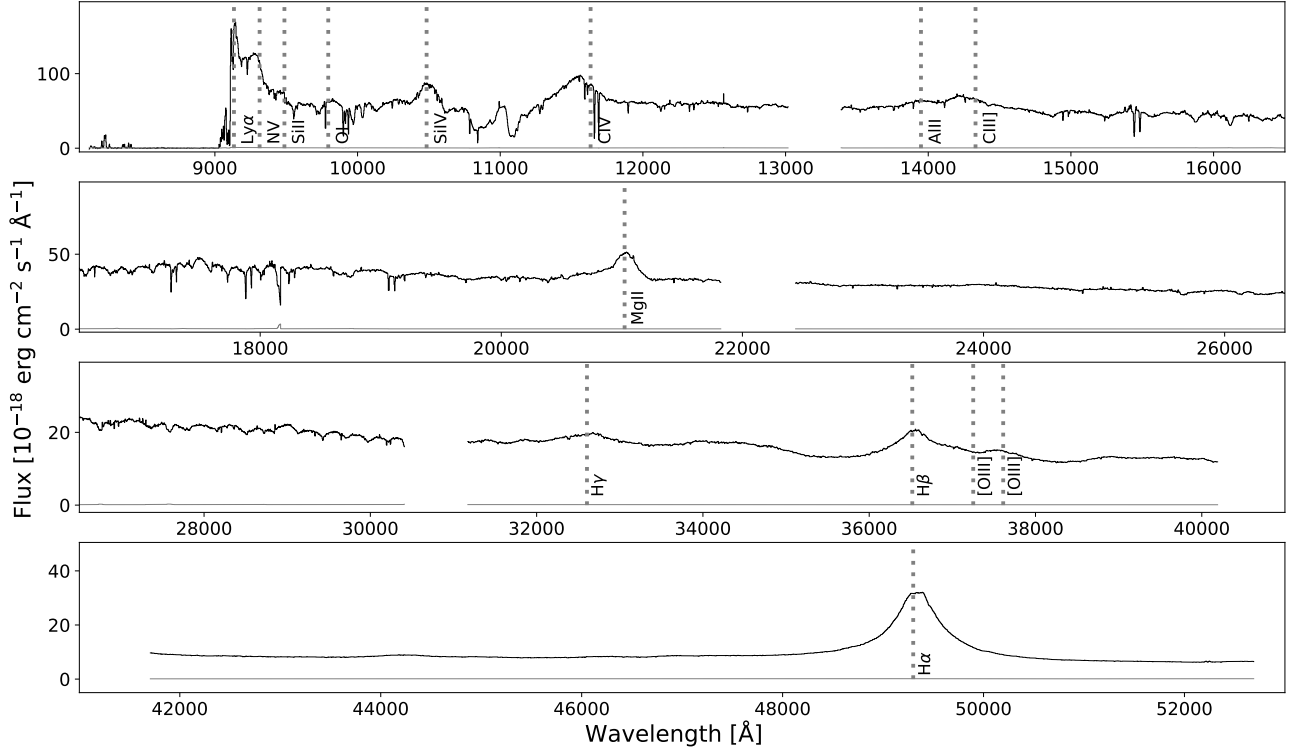


Fig. 3. NIRSpec fixed slit and 1D spectrum from Band III data ($\lambda > 31160 \text{ \AA}$) of UHS J0439+1634. The spectrum shows clear features from intrinsic broad absorption lines (BAL), particularly from C IV, but also at wavelengths between Ly α and Si IV, the underlying quasar continuum suggests an absorbed fraction when extending power-law function continuum fit obtained from wavelengths redwards of the C III] line.

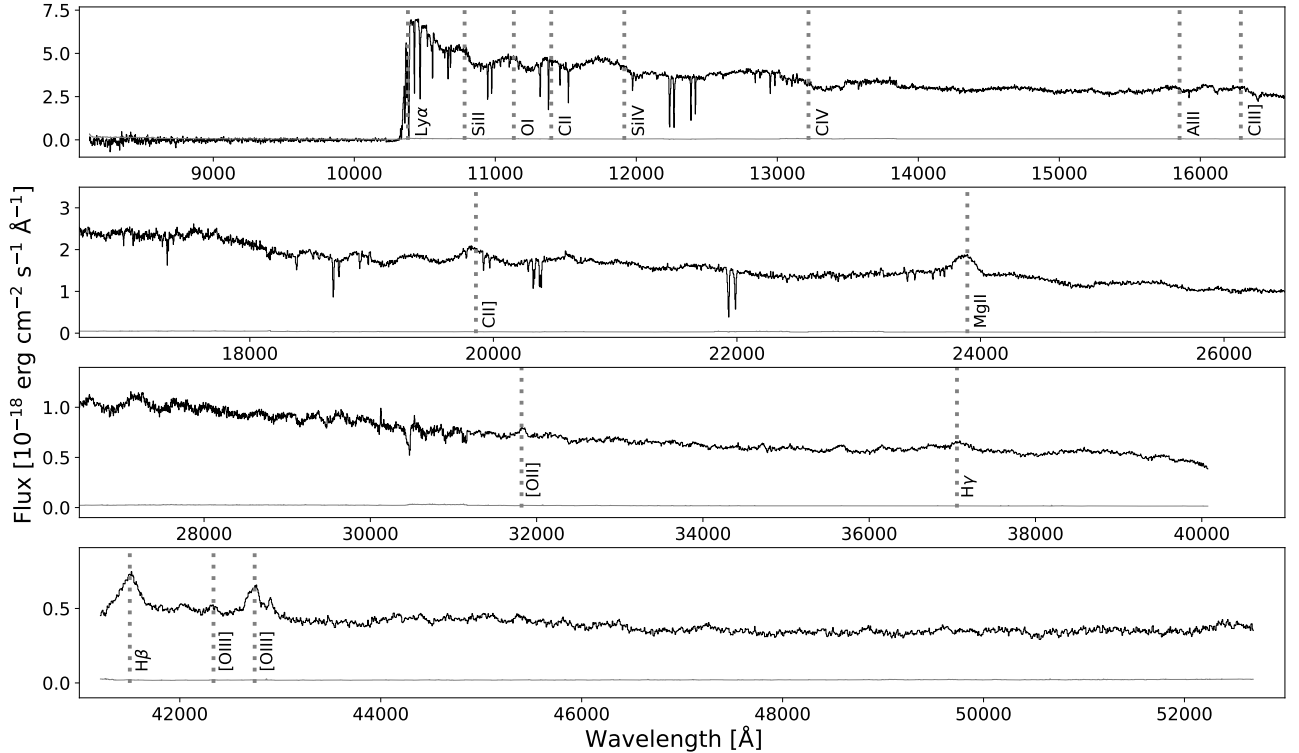


Fig. 4. NIRSpec fixed slit and extracted 1D spectrum from Band III data ($\lambda > 31700 \text{ \AA}$) of ULAS J1342+0928.

width of the NIRSpec S200A1 and S200A2 Fixed Slits projects on to just under two mean 104 mas pixels on the detector. As a result, the apparent line spread function in a given spectrum at a

given wavelength will depend on how precisely the slit width is sampled by the between two and three pixels that its monochromatic image happens to project to. This variable sampling is-

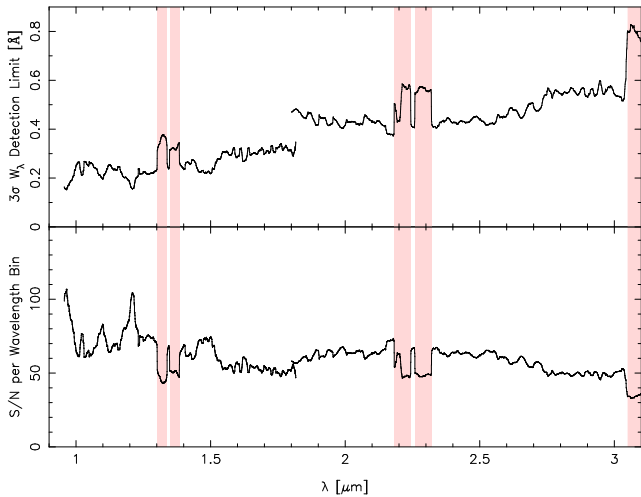


Fig. 5. *Lower panel:* Signal-to-noise ratio per wavelength bin as a function of wavelength for the combined Band I and Band II spectra of VDES J0020–3653. The regions of reduced total exposure caused by the detector gap are shown as shaded. *Upper panel:* Corresponding anticipated three sigma narrow absorption line equivalent width detection limit as a function of wavelength.

sue is further exacerbated by the slit tilt and optical distortion that NIRSpec spectra are subject to, which necessitate that significant resampling of the raw 2D spectra be performed in the NIRSpec reduction pipeline in order to rectify the spectra to a common wavelength and spatial scale that will allow accurate background subtraction and summation of the net quasar signal along the spatial direction. That the final spectra are assembled by co-adding several differently sampled dithered sub-exposures taken at different positions along the slit leads to further smearing of the apparent line spread function. Lastly, the fact that the targets observed here are point sources, whose monochromatic images at the shorter wavelengths are not expected to fill the full width of the slit, adds even further variation in the spectral sampling. The net impact of these effects can be readily seen in Figure 6 which shows close-ups of four representative narrow absorption lines detected in our final spectra, overlaid by their best fit Gaussian profiles. It is evident that the coarse sampling of NIRSpec spectra causes the apparent widths of the absorption lines to vary randomly at the ≈ 1 wavelength bin level, even among lines having comparable strengths. This stochastic variation in the apparent shape of the pixelated line spread function due to sampling noise clearly precludes performing meaningful detailed profile fits to our unresolved absorption lines. However, it ought not bias measurement of the main parameters of interest – line equivalent widths and centroid wavelengths – provided the error propagation calculation for these measured parameters correctly mirrors the noise level in the resampled spectra.

The top panel of Figure 5 shows the anticipated 3σ observed equivalent width sensitivity limit to detecting unresolved absorption lines calculated from the lower S/N curve per the expression

$$W_\lambda > 3 \frac{\Delta\lambda}{(S/N)} n_{\text{FWHM}}^{3/2} \quad (1)$$

assuming the FWHM of the NIRSpec line spread function to be a multiple of the wavelength bin size $\delta\lambda = n_{\text{FWHM}}\Delta\lambda$ with n_{FWHM} (the number of spectral pixels sampling the line spread function), conservatively set to $n_{\text{FWHM}} = 2.3$ for both bands.

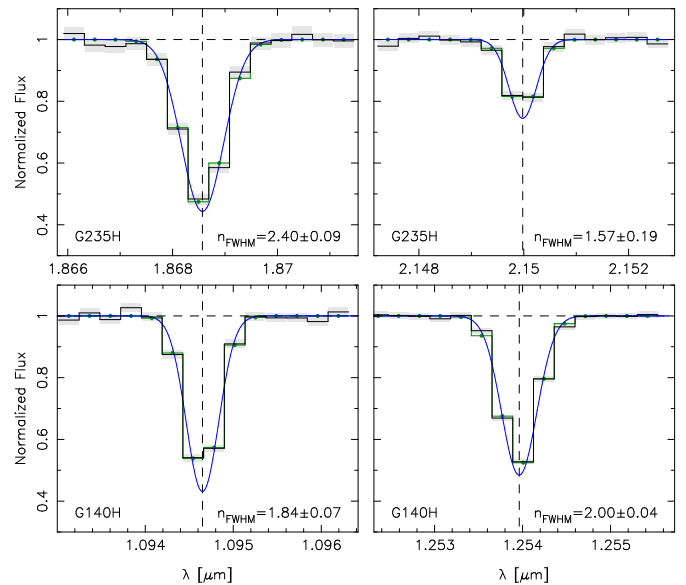


Fig. 6. Representative examples of normalized line profiles illustrating the coarse wavelength sampling of the NIRSpec spectra. The shaded error bars shown are $\pm 1\sigma$. The best-fit Gaussian fits and their FWHM expressed in spectral wavelength bins are also shown.

It follows that we anticipate being able to measure absorption lines having observed equivalent widths $W_\lambda > 0.2 \text{ \AA}$ in our spectrum of VDES J0020–3653. The equivalent S/N and line sensitivities achieved for DELS J0411–0907 and ULAS J1342+0928 are comparable to those of VDES J0020–3653 as shown in Figure 5. However, our spectrum of the considerably brighter UHS J0439+1634 reaches $S/N \approx 90 - 200$, albeit with actual gaps in the spectrum at the missing S200A1 wavelengths.

We have not attempted to quantify the S/N achieved in the IFU-based Band III G395H extensions to our spectra. One reason for this is that the STScI pipeline used to reduce the IFU data outputs an estimate of the error spectrum that significantly underestimates the actual noise level in the data. This does not affect our results, since we only detect a single NaI absorption feature in the Band III G395H data (Section 4.4.7).

A final consequence of the coarse sampling and optical distortion that NIRSpec spectra are subject to is worth mentioning. The NIRSpec GTO pipeline employs a strict photon conserving (pixel projection weighting) resampling scheme when rectifying the native 2D spectra to a common wavelength and spatial scale. Nonetheless, in the case of a point source, the coarse sampling of the native 2D spectrum gives rise to Moire-style numerical fringing in the resampled spectrum along any resampled spatial row (cf. Smith et al. 2007). The amplitude of this unavoidable numerical fringing (or ‘wobble’) at any given wavelength is effectively averaged out provided the net signal is integrated over a sufficient number of spatial rows large enough to capture most of the light from the target. In the spectra presented here the GTO pipeline performed this summation over a fixed five spatial rows. This is adequate to integrate down the fringing at wavelengths $\lambda < 2.8 \mu\text{m}$, but gradually fails at longer wavelengths and can be seen in our Band II G235H spectra due to the FWHM of the PSF increasing linearly with wavelength in the diffraction-limited NIRSpec, causing a varying amount of light to be missed in the five row summation. This numerical fringing effect is particularly pronounced in NIRSpec IFU data (Marshall et al. 2023; Perna et al. 2023), but is less obvious in our 1D Band III spectra

since these were extracted by summing over a large number of spaxels. In any event, since the effect causes a modulation of the entire spectrum it should not affect measured equivalent widths and line centroids as long as the local continuum is set to follow the modulation (Section 3.2).

3. Analysis of the spectra

The full one-dimensional spectra of the quasars are presented in Figures 1, 2, 3, and 4, with emission lines commonly seen in quasar spectra marked. We find a small shift in the absolute flux levels between the Fixed Slit and the IFU spectra, and have scaled the extracted one-dimensional Band III spectra by a factor of ≈ 0.7 to match the flux level at the overlapping wavelengths in the Fixed Slit Band II spectra.

3.1. Quasar systemic redshifts

In this paper, we focus on the analysis of intervening absorption line systems, and therefore re-visit the estimated quasar systemic redshifts in order to distinguish intervening from proximate metal absorbers arising less than 3000 km s^{-1} from the quasar redshifts. This velocity cut-off is chosen since absorbers nearer than this limit show different physical properties such as metallicities and ionisation levels compared to genuine intervening absorption systems (Ellison et al. 2010). UHS J0439+1634 is a broad absorption line (BAL) quasar, and therefore could potentially affect its environment to even larger velocities of $\sim 10,000 \text{ km s}^{-1}$. In this spectrum we find two absorption systems that are offset by 9000 km s^{-1} , and both systems show narrow lines. We choose to include both absorption systems in the statistical analysis having a uniform cut at 3000 km s^{-1} for the four quasar spectra.

Determining systemic redshifts for quasars is complex because of the dynamical effects that present themselves in quasar spectra. Broad emission lines can be blueshifted by several thousand km s^{-1} relative to the systemic redshift, and can be composed of multiple components with peaks at distinct wavelengths, reflecting distinct kinematic components in the broad line regions. With the extended coverage of the rest-frame optical Balmer lines and narrow lines from [O II] $\lambda\lambda 3727, 3729$ or [O III] $\lambda\lambda 4959, 5007$ afforded by the NIRSpec spectra, more accurate systemic redshifts can be derived.

Fits to $H\alpha$ lines from the Band III spectra of VDES J0020–3653 and DELS J0411–0907 and redshift measurements are presented in Marshall et al. (2023). The asymmetric [O III] line profile of VDES J0020–3653 is caused by excess emission from extended regions spatially offset by ~ 1 arcsec from the quasar (Marshall et al. 2023). Our fit to the $H\alpha$ emission line from VDES J0020–3653 is best reproduced by a combination of a broad Lorentzian and a broad Gaussian profile plus much weaker narrow components of $H\alpha$ and [N II] $\lambda 6584$ lines from the host galaxy, which gives a redshift of $z = 6.8601 \pm 0.0001$, i.e. slightly higher than $z = 6.855$ based on a fit of two Gaussian components reported by Marshall et al. (2023).

Fits of Lorentz profiles to $H\alpha$ and $H\beta$ emission from DELS J0411–0907 suggest a systemic redshift of $z = 6.8253 \pm 0.0002$ consistent with the initial redshift reported by Pons et al. (2019), and $z = 6.8260 \pm 0.0007$ based on [C II] $158 \mu\text{m}$ emission (Yang et al. 2021), while multi Gaussian component fits to [O III] $\lambda 5007$ and $H\alpha$ emission lines suggest a smaller redshift of $z = 6.818$ as the systemic one (Marshall et al. 2023). The difference in the inferred systemic redshift is caused by a narrow component of

$H\alpha$ that is blueshifted by $\sim 380 \text{ km s}^{-1}$ relative to the broad $H\alpha$ component (Marshall et al. 2023).

The [O III] $\lambda 5007$ line in the spectrum of ULAS J1342+0928 can be fit by a double Gaussian line profile, where the narrow component suggests a lower redshift of $z = 7.5317 \pm 0.0007$ compared to the centroid of the broad component at $z = 7.5435 \pm 0.0002$. In comparison, a single Gauss component fit to the $H\beta$ emission line provides an adequate fit with $z = 7.5353 \pm 0.0004$. The redshift derived from $H\beta$ is smaller by $211 \pm 35 \text{ km s}^{-1}$ compared to $z = 7.5413 \pm 0.0007$ measured from [C II] $158 \mu\text{m}$ emission from the quasar host (Venemans et al. 2017).

The Mg II line profile in the spectrum of UHS J0439+1634 is asymmetric with a significant blue wing. Fitting the broad line with a Lorentzian profile, we derive a redshift of $z = 6.5102 \pm 0.0005$ consistent with a fit to the same line in a GNIRS spectrum from the Gemini telescope that reveals $z = 6.511 \pm 0.003$ (Fan et al. 2019). The [C II] $158 \mu\text{m}$ emission from this object suggests a systemic redshift of $z = 6.5188 \pm 0.0004$ (Yang et al. 2019). The $H\alpha$ line is covered by the NIRSpec Band III data, and its line profile shows a broad component that is well fit by a single Lorentzian profile with narrow emission line components superimposed. The narrow emission lines are recognised as $H\alpha$ and [N II] $\lambda\lambda 6548, 6584$ from the host galaxy, suggesting a redshift of $z = 6.5185 \pm 0.0003$, consistent with that from the [C II] $158 \mu\text{m}$ emission.

The systemic quasar redshifts inferred from our spectra and used in the following analysis are summarized in Table 2.

3.2. Normalization of spectra

For computations of absorption line equivalent widths, we need to determine the level of the continuum emission around the lines. First, we make a global fit of the continuum level across the entire spectrum using the Astrocook code (Cupani et al. 2022), using nodes with a velocity spacing of 1000 km s^{-1} , and reject nodes that deviate at the 5σ level within each velocity-window. Some of these outliers are caused by the presence of absorption lines. A spline function is then fit between the remaining node-points. A small window-size is necessary in order to also fit the broad emission lines of the quasars. The spectra in Figures 1, 2, 3, and 4 show strong modulations in the continuum flux level in the fixed slit spectra around $1.8 \mu\text{m}$ and $3.0 \mu\text{m}$ as described in Section 2. We therefore choose to manually correct the continuum node points within Astrocook before the normalization of the spectra, $f_{\text{norm}}(\lambda)$, and their associated error spectra, $\sigma(f_{\text{norm},\lambda})$ are computed. The normalized spectra are shown in Appendix A with the lines belonging to the identified absorption systems at different redshifts overlaid.

With normalized spectra the observed equivalent widths (W_{obs}) and their uncertainties are computed by

$$W_{\text{obs}} = \sum_{\lambda_1}^{\lambda_2} (1 - f_{\text{norm}}(\lambda)) \Delta\lambda \quad (2)$$

$$\sigma(W_{\text{obs}}) = \sqrt{\sum_{\lambda_1}^{\lambda_2} \sigma^2(f_{\text{norm},\lambda}) \Delta\lambda^2} \quad (3)$$

where $\Delta\lambda$ is the wavelength bin per pixel in the spectra.

In order to analyse the quasar spectra bluewards of their Ly α emission, we have to take a different approach to normalize the quasar spectra since the IGM has effectively absorbed most of the emission in the Gunn-Peterson trough at these redshifts. We

Quasar	$z_{\text{sys,JWST}}$	$z_{\text{sys,[C II]}}$	J_{AB}
VDES J0020–3653	6.8601 ± 0.0001		20.40 ± 0.10
DELS J0411–0907	6.8253 ± 0.0002	6.8260 ± 0.0007	20.02 ± 0.14
UHS J0439+1634	6.5185 ± 0.0003	6.5188 ± 0.0004	17.46 ± 0.02
ULAS J1342+0928	7.5353 ± 0.0004	7.5413 ± 0.0007	20.30 ± 0.02

Table 2. Systemic quasar redshifts derived from fits to the Balmer emission lines in the NIRSpec spectra. The third column lists the quasar systemic redshifts derived from [C II] 158 μm emission (Venemans et al. 2017; Yang et al. 2019, 2021), and the last column the J band magnitude (Yang et al. 2021; Reed et al. 2019).

use the python module PyQSOFit (Guo et al. 2018) to construct a model of the quasar continuum emission and broad Ly α emission line. We choose to model the continuum as a power-law function at wavelengths not affected by broad emission lines and superimpose best fits of the quasar Ly α emission line on top of the continuum, using a set of Gaussian functions with different widths, including both broad and narrow components. The observed spectra are divided by the constructed model spectra and the normalized spectra show the relative transmission in the IGM. We use these normalized spectra to explore the connection between the metal absorption line systems and transmission spikes in the IGM in Section 6.

4. Metal-line absorption systems

In the four quasar spectra we identify metal absorption line systems at several different intervening redshifts as well as in the vicinity of the quasar redshifts. Compared to the IGM where metal ions are typically highly ionized, intervening ISM or CGM lines are typically recognised via low-ionization absorption lines from O I, Si II, C II, S II, Al II, Zn II, Cr II, Mn II, Fe II, Mg II, and Mg I, but also may have higher ionization lines from Al III, C IV, and Si IV. We used the atomic line list in Krogager (2018), which is compiled from the Vienna Atomic Line Data Base (Piskunov et al. 1995; Ryabchikova et al. 2015).

The discovery and classification is done through visual inspection searching for systems of lines commonly detected in quasar damped Ly α systems (e.g. Prochaska et al. 2003) and Gamma-ray burst afterglow spectra that include strong damped Ly α systems (e.g. Christensen et al. 2011). Visual identifications, just as machine generated ones, are aided by the presence of line doublets, such as Mg II $\lambda\lambda 2796, 2803$ or C IV $\lambda\lambda 1548, 1550$ whose wavelength separations and fixed relative strengths given by their oscillator strengths are well known. The relative line strengths are different by a factor of two in the optically thin regime, while in the optically thick regime, the line strengths are identical. In addition, absorption lines may have multiple kinematic components and blending with other lines makes the identification of line doublets more complex. In order to identify an absorption line system, we require that at least two or more lines are found for each system such that the identity of the lines and the redshift of the absorption system is uniquely determined.

In the spectrum of VDES J0020–3653 we identify 16 absorption systems, in DELS J0411–0907 we find 13 systems, in UHS J0439+1634 17 systems, and in ULAS J1342+0928 we find 15 individual absorption systems. In total, 61 identified systems are detected at $2.4 \lesssim z \lesssim 7.5$. Appendix A presents the four normalized quasar spectra with identified absorption line systems overlaid. The systems and individual absorption lines are presented in both graphical and tabular form in Appendix B.

4.1. Distinguishing C IV doublets from O I/Si II absorbers

We need to pay particular attention to the identification of C IV $\lambda\lambda 1548, 1550$ doublet and O I $\lambda 1302$ –Si II $\lambda 1304$ absorbers since the two pairs of transitions have transition wavelength ratios of 0.99834 and 0.99831, respectively. These two separations cannot be distinguished at the $R \simeq 2700$ spectral resolution of the NIRSpec spectra, and weak systems may not be detected at the signal-to-noise level needed to unambiguously detect the C IV $\lambda\lambda 1548, 1550$ doublet. To single out potential O I $\lambda 1302$ –Si II $\lambda 1304$ absorption systems, absorption lines from Si II $\lambda 1260$ and Si II $\lambda 1526$ should be detected too, since they are stronger by a factor of 8.9 and 1.6, respectively, relative to the Si II $\lambda 1304$ line. The Si II $\lambda 1260$ line may, however, fall in the Ly α forest region and be completely absorbed in the GP troughs. In addition to other silicon transitions, we also search for other associated lines from C II $\lambda 1334$ or Mg II $\lambda\lambda 2796, 2803$. When none of these lines are detected, we classify the absorber as a C IV system.

4.2. Comparison with known absorption systems

As surveys detect more and more high-redshift quasars, an increasing number of studies of intervening absorption lines have been performed. The recent XQR-30 survey is based on a sample of 30 quasars at $5.8 < z < 6.6$ observed with VLT/X-shooter at higher-resolution (D’Odorico et al. 2023). The only quasar in common with the NIRSpec sample is UHS J0439+1634, where Davies et al. (2023a) identify a total of 43 absorption line systems from $z = 2.2 - 6.48$. All of the 17 systems we detect, apart from the Mg II doublet at $z = 6.208$, are also detected in Davies et al. (2023a). In contrast, in our lower spectral resolution data we are not able to clearly identify and detect the other absorption line systems. In particular, Davies et al. (2023b) find several weak C IV doublets in the range from $z = 5.0 - 5.3$ and also weak rest-frame equivalent width ($W_r < 0.05 \text{ \AA}$) Mg II absorbers at $z \approx 2.3 - 5$ that we cannot confirm in the NIRSpec data. The non-confirmation is either due to blending with other stronger absorption lines from different redshifts, or the fact that only one of the two lines in the doublet can be detected in the NIRSpec data, while the other component is clearly ruled out from the knowledge of the fixed line strengths between the two doublet lines. We are also not able to confirm several of the reported Si IV doublets. We note that around $z \sim 5$ C IV falls in a wavelength region affected by (weaker) telluric absorption lines and also strong sky emission lines, that Davies et al. (2023a) do, however, correct for in their analysis.

Turning to absorption line systems at $z > 5$, Cooper et al. (2019) report two systems at $z = 5.936$ and 6.178 towards DELS J0411–0907, and at $z = 5.889$, 6.271 and 6.843 towards ULAS J1342+0928. These strong systems are all clearly detected in the NIRSpec spectra. In addition, we also detect a few weaker $z > 5$ Mg II or C IV doublets towards DELS J0411–0907,

whereas towards ULAS J1342+0928, we also find several additional low-ionization systems at $z > 7$ identified through multiple lines. ULAS J1342+0928 was observed with both X-shooter at the VLT and with FIRE at the Magellan Telescope at a higher spectral resolution as presented in a detailed case study of the $z = 6.84$ absorption system in [Simcoe et al. \(2020\)](#). We retrieved the processed 2-dimensional X-shooter spectra Advanced Data Products from the ESO archive in order to verify whether the high-redshift absorption line systems detected in the NIRSpec data are also present in the higher resolution spectra. For the higher redshift system at $z = 7.368$, the X-shooter data reveals a clear detection of Si II $\lambda 1260$ whereas Mg II falls in a noisy region of the spectrum and is not detected. None of the absorption lines from the $z = 7.443$ or $z = 7.476$ systems can be detected in the X-shooter data, consistent with the less sensitive detection-limit in the ground-based data.

4.3. Line densities

Theoretically we expect a detection limit of absorption lines observed equivalent widths at $W_{\text{obs}} = 0.2 - 0.5 \text{ \AA}$ as described in Sect. 2 and Fig. 5. With the wide redshift range of the absorption systems, this implies that the detection limit on the rest-frame equivalent width $W_r = W_{\text{obs}}/(1 + z_{\text{abs}})$ depends on the absorber redshift. The typical detection limit of W_r is $0.025 - 0.03 \text{ \AA}$. When comparing line densities with those of from the literature, we adopt the same W_r cut-off.

To compute line densities, we combine all tables in Appendix B, extract the individual absorption transitions of interest, e.g. C IV $\lambda 1548$, O I $\lambda 1302$, or Mg II $\lambda 2796$ and compute their W_r . Line densities from metal-absorption lines should represent random lines of sight through the Universe, and we therefore exclude absorbers at redshifts closer than 3000 km s^{-1} from the quasar systemic redshift, since these absorption lines represent proximate systems that may be influenced by the quasars.

We compute the redshift path length, which is defined as the full spectral range in each spectrum where it would be possible to detect the chosen absorption line. For each quasar we determine the minimum and maximum redshift where a chosen absorption line can be discovered, excluding regions in the spectra where there are gaps or where the signal-to-noise ratio is low. The sum of this gives the sensitivity function, $g(z)$, which presents for each redshift the number of lines of sight probing the absorption line of interest with an observed $W_{\text{obs}} > 0.3 \text{ \AA}$. The result is presented in Fig. 7 which illustrates that the NIRSpec observations in this study are sensitive to intervening O I $\lambda 1302$ and C II $\lambda 1334$ absorbers at $6 \lesssim z \lesssim 7.5$, Si II $\lambda 1526$ and C IV absorbers at $5 \lesssim z \lesssim 7.5$, Mg II at $2.2 \lesssim z \lesssim 7.5$, and Si IV at $5.5 \lesssim z \lesssim 7.5$.

By integrating the sensitivity function one can compute the line density dn/dz , defined as the number of absorbers n within a chosen redshift interval dz . However, when analysing the line density over a very large redshift range it is conventional to instead analyse the comoving density ([Bahcall & Peebles 1969](#)) and use the comoving absorption path length X defined as:

$$dX = \frac{(1+z)^2}{\sqrt{\Omega_M(1+z)^3 + \Omega_\Lambda}} dz. \quad (4)$$

The line density is then computed as

$$dn/dX = \frac{\sum_{z_1}^{z_2} n_i}{\int_{z_1}^{z_2} g(z) dX}, \quad (5)$$

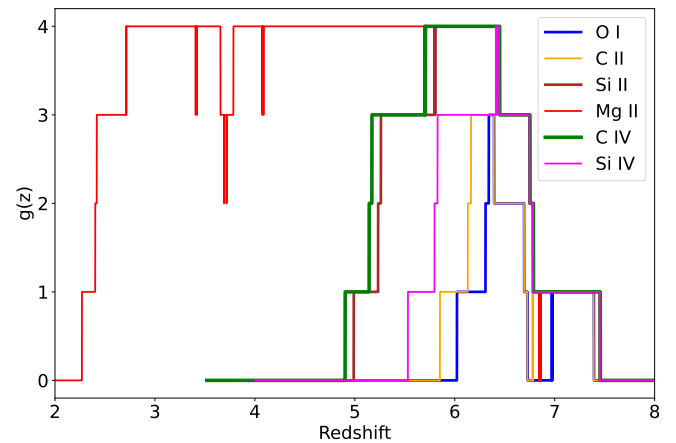


Fig. 7. Sensitivity functions, $g(z)$, for the coverage of O I $\lambda 1302$, C II $\lambda 1334$, Si II $\lambda 1526$, C IV $\lambda 1548$, Si IV $\lambda 1393$, and Mg II $\lambda 2796$. The colored lines illustrate how many of the quasar spectra contribute to the search of metal absorption lines as a function of redshift.

where n_i is the number of absorbers of the chosen species in quasar number i , summed over the redshift interval between z_1 and z_2 in all the quasar spectra. The denominator is the integral of the absorption path length in that redshift interval.

To derive uncertainties of the line densities we assume that the distribution of absorbers is Poissonian in nature. For the small number statistics relevant in this work we use the upper- and lower 68% confidence intervals tabulated in [Gehrels \(1986\)](#).

4.4. Absorption line density redshift evolution

Among the many different atomic species detected in the four quasar spectra, in this work we focus on the previously well-studied ones among the low-ionization and high-ionization lines.

For each atomic transition we compute the line density as a function of redshift and compare the JWST data with line densities at lower redshifts from the literature. Additionally, we compare the line densities with the predicted evolution of both low- and high-ionizations column density distribution from simulations in the redshift range $5 < z < 8$ ([Huscher et al. in prep.](#)). The simulations are based on updates to the TECHNICOLOR DAWN cosmological hydrodynamic simulation ([Finlator et al. 2018, 2020](#)). By probing random lines of sight through the simulation volumes from redshifts $z = 5$ to $z = 10$, one can identify various absorption lines (e.g. [Doughty & Finlator 2019, 2023](#)) and compute their equivalent widths and column densities. Compared to previous simulations, the model of Huscher et al. includes predictions of equivalent widths and column densities of other atomic transitions for the modelled absorbers, allowing us to compare with the observations of a range of elements in different redshift bins from $z = 5$ to $z = 10$. For comparison with the NIRSpec observations, we restrict our attention to the relevant redshift interval $5 < z < 7.5$.

4.4.1. O I $\lambda 1302$ absorbers

We detect seven O I $\lambda 1302$ absorbers listed in Table 3 within the total absorber path length interval $\Delta X = 7.68$. The highest redshift absorption system at $z = 7.476$ lies close to the ULAS J1342+0928 quasar redshift at $z = 7.535$, and is considered proximate according to the cut-off of at 3000 km s^{-1} , and is not included in the analysis of the statistics of line densities. The

Table 3. O I $\lambda 1302$ systems

Quasar	z_{abs}	$W_{\text{rest}} (\text{\AA})$
VDES J0020–3653	6.4535	0.091 ± 0.007
VDES J0020–3653	6.5625	0.062 ± 0.008
VDES J0020–3653	6.6690	0.115 ± 0.010
UHS J0439+1634	6.2880	0.119 ± 0.006
ULAS J1342+0928	7.3680	0.061 ± 0.011
ULAS J1342+0928	7.4430	0.031 ± 0.010
ULAS J1342+0928	7.4760^\dagger	0.045 ± 0.010

[†]The highest redshift system at $z = 7.4760$ lies $\approx 2000 \text{ km s}^{-1}$ from the quasar redshift and is considered as a proximate system, and therefore not included in the computation of line densities.

Table 4. C II $\lambda 1334$ systems

Quasar	z_{abs}	$W_{\text{rest}} (\text{\AA})$
VDES J0020–3653	6.4535	0.103 ± 0.010
VDES J0020–3653	6.6690	0.168 ± 0.010
DELS J0411–0907	6.1774	0.215 ± 0.006
UHS J0439+1634	5.9280	0.008 ± 0.007
UHS J0439+1634	6.2880	$< 0.086 \pm 0.007^\dagger$
ULAS J1342+0928	6.8427	0.626 ± 0.011
ULAS J1342+0928	7.3680	$< 0.063 \pm 0.010^\dagger$
ULAS J1342+0928	7.4430	0.072 ± 0.009

[†]The upper limit to the equivalent width is quoted because the line is blended with another absorption line at a different redshift (See Appendix B).

two other O I systems at $z > 7$ represent the highest redshift detections of neutral oxygen absorption along the line of sight to high-redshift quasars reported to date. In all cases, when O I is detected, we also detect more than one other line at the same redshift, so we can be confident to clearly identify the O I absorption systems (See Appendix B).

Figure 8 shows the line density of O I absorbers with $W_r > 0.05 \text{ \AA}$ as a function of redshift for the new NIRSpect measurement compared with values at lower redshifts from Becker et al. (2019). The line density for the highest redshift point has a significant uncertainty, implying that even though the line density shows an increase from $z = 6$ to $z = 7$ the values are also consistent with being constant.

For O I as well as for other low-ionization line species, the model predicts an increase in line density with increasing redshift up to $z \sim 7$ and at higher redshifts ($z > 7$) the line density decreases. The reason for this behaviour is a combination of a decreasing metallicity of the CGM with increasing redshift, while the turnover from $z = 7 \rightarrow 6$ is caused by the increasing level of ionization of the CGM with time (Doughty & Finlator 2019). With increasing cosmic time, O I absorbers have a smaller covering fraction as the clouds' outskirts become increasingly ionized while the total metallicity of oxygen and its distribution in the CGM of galaxies does increase with time (Doughty & Finlator 2019).

4.4.2. C II $\lambda 1334$ absorbers

In the JWST spectra we identify eight intervening C II $\lambda 1334$ absorption systems listed in Table 4 over a full path length interval of $\Delta X = 11.10$ at $5.9 < z < 7.5$. Due to the available search path, some of the C II lines do not have detected O I absorption, since these lie blueward of the quasar Ly α wavelength. The upper right hand panel in Fig. 8 illustrates the C II line densities with $W_r > 0.03 \text{ \AA}$.

In comparison, Becker et al. (2019) find that most of their O I absorbers also have C II lines, but this is primarily caused by selection since to identify O I absorption lines, the presence of other lines (e.g from C II) at the same redshift is required. The line density of C II at $z < 5$ therefore shows a redshift evolution similar to that of O I. Using the absorption line catalog of carbon absorbers in Davies et al. (2023a), we compute the C II line densities in three redshift bins at $5.0 < z < 6.5$ as illustrated in Fig. 8. Including the line density at $z > 6$ from the NIRSpect data we find a general trend of an increasing line density with redshift.

4.4.3. Si II $\lambda 1526$ absorbers

Several Si II transitions can be detected in the spectra with UV transitions at rest-frame wavelengths at 1260, 1304, 1526, and 1808 \AA . Due to the wide range of oscillator strengths and possible contamination with other absorption lines, not all absorption lines are detected for any given system. When deriving the line density of Si II it is convenient to use a line which is both a strong transition and also has a large redshift path length. The 1808 \AA line has the longest redshift path length, but it is the weakest transition of the four, whereas the strongest 1260 \AA line can only be detected in a very short path length interval because its wavelength is close to Ly α . Therefore we choose to investigate the line density based on the 1526 \AA line, which is also a strong transition, and has a larger redshift path length interval.

In the JWST spectra we identify 12 intervening Si II absorption systems listed in Table 5 over a full path length interval of $\Delta X = 29.0$ at $5 < z < 7.45$. We compare the inferred line density with that derived from the database in Davies et al. (2023a) in the lower left hand panel Figure 8. It is apparent that the evolution of the Si II line density could either be constant or show a mild increase with redshift to $z \approx 7$.

In the models of Huscher et al. in prep., rest-frame equivalent widths are computed for the Si II $\lambda 1260$ transition. For non-saturated lines, the relation between two lines in the linear part of the curve of growth scale as $W_{r1}/W_{r2} = \lambda_1^2 f_1 / (\lambda_2^2 f_2)$, where λ_1 and λ_2 are the rest-frame wavelength of the two transitions and f_1 and f_2 are the oscillator strengths. We can therefore convert the estimated Si II $\lambda 1260$ line densities to that for Si II $\lambda 1526$. The model predicts a constant line density of $dn/dX \approx 0.04$ from $z = 5$ to $z = 8$ for absorbers with $W_r < 0.025 \text{ \AA}$, which is smaller by a factor of ~ 12 compared to the NIRSpect observations. Alternatively, the model predicts Si II equivalent widths that are a factor of 2.5 smaller than the observed ones.

4.4.4. Mg II $\lambda 2796$ absorbers

The classical Mg II $\lambda 2796, 2803$ doublet is one of the most commonly studied atomic transitions in quasar spectra (e.g. Bergeron & Boissé 1991; Churchill et al. 1999). It is easily distinguishable in absorption because of its known line separation and the fact that the 2796 line has twice the oscillator strength as the 2803 line. The line doublet enters the optical range at $z = 0.3$ and can be traced up to $z \sim 7$ in ground-based near-IR spectra (Matejek & Simcoe 2012; Chen et al. 2017). In comparison to ground-based observations of Mg II absorbers at $z > 2.5$ that

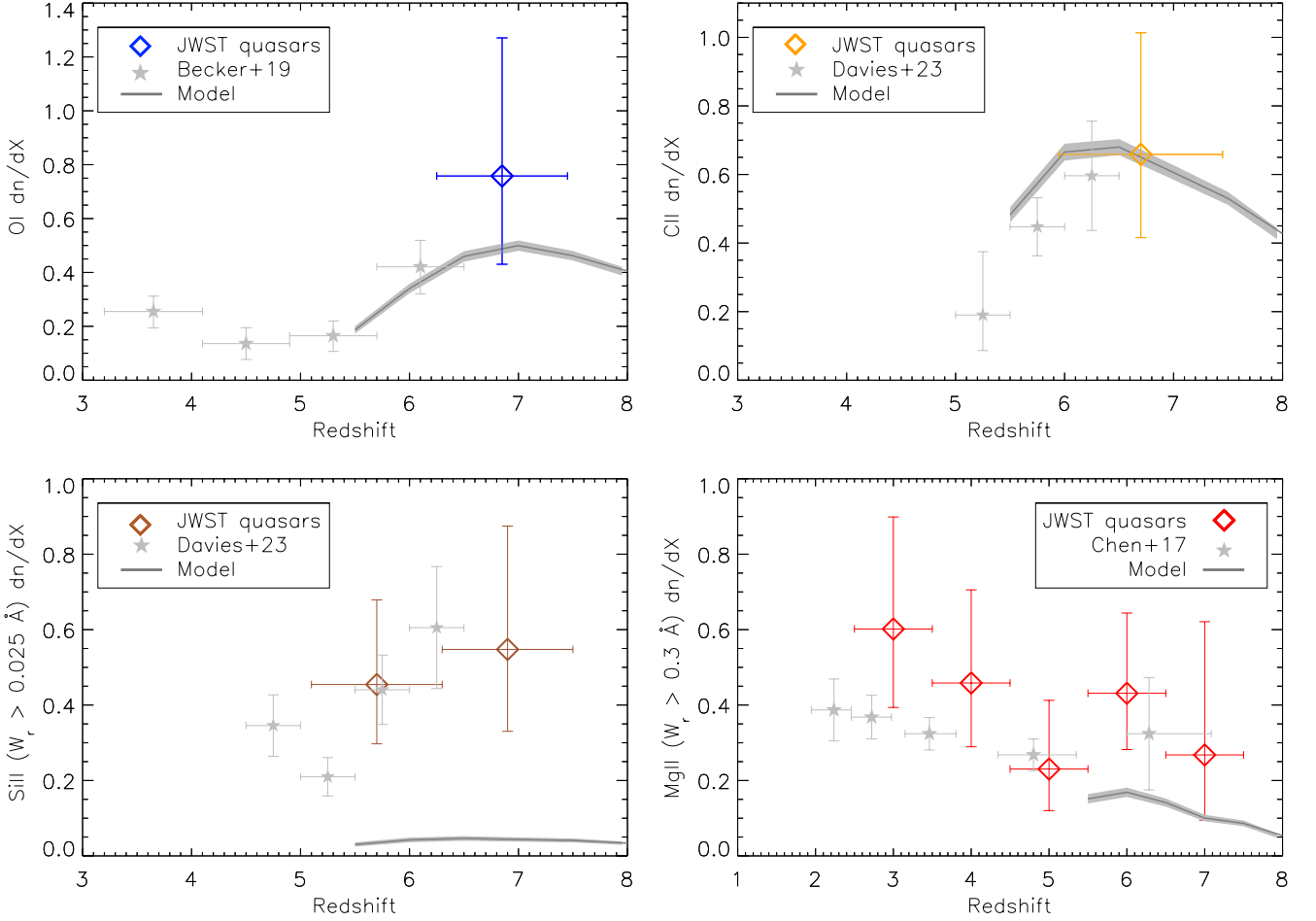


Fig. 8. Line densities as a function of redshift for low-ionization lines. In all panels, colored symbols represent the JWST data, where error bars for the line densities represent 68% confidence intervals for small-number Poisson uncertainties (Gehrels 1986). The line densities are compared to predictions from numerical models (Huscher et al. in prep.) computed from the same selection of W_r as from the NIRSpec observations. *Upper left panel:* O I $\lambda 1302$ absorption line densities for systems with $W_r > 0.05$ Å showing an increase in line density at $z > 6.5$ from the NIRSpec data compared to lower redshifts (Becker et al. 2019). *Upper right panel:* C II $\lambda 1334$ absorption line densities for systems with $W_r > 0.03$ Å compared to lower redshift values derived from the catalog in Davies et al. (2023a). *Lower left panel:* Si II $\lambda 1526$ absorption line densities for systems with $W_r > 0.025$ Å compared to that derived from the absorption database in Davies et al. (2023a). The model prediction at $dn/dX \approx 0.04$ under-produces the Si II line densities by a factor of ≈ 12 . *Lower right panel:* Mg II $\lambda 2796$ absorption line densities for systems with $W_r > 0.3$ Å. Compared to the Mg II study in (Chen et al. 2017), the NIRSpec data suggest that the line density could be constant or have a shallow decrease with increasing redshifts in agreement with the model prediction.

are heavily affected by the presence of sky emission- and telluric absorption lines, the NIRSpec spectra are much cleaner, allowing easy visual identification of Mg II absorbers even at the highest redshifts. It is therefore not surprising that we find some previously undetected absorption systems in these well-studied high-redshift quasars.

The 3σ detection limit of the W_{obs} for Mg II systems in the NIRSpec spectra is 0.3 Å. Above this limit, we find 49 Mg II absorbers from $z = 2.4$ to $z = 7.45$ including the highest redshift detection of an intervening absorption system to date (see Appendix B). As for the other lines, absorption line systems that lie closer than 3000 km s^{-1} to the quasar redshift are omitted in the computation of line densities. The highest redshift proximate absorption system at $z = 7.476$ is also detected in Mg II, and is excluded in the line density computation.

The total redshift path length for Mg II absorption systems covered by the four spectra is $\Delta X = 73.3$. To compare with other studies, we focus on the absorbers with $W_r > 0.3$ Å, where we

detect 30 systems. The lower right hand panel in Fig. 8 illustrates that the line density for Mg II absorbers with $W_r > 0.3$ Å remains constant or at most exhibits a shallow decrease to the highest redshifts in agreement with previous findings at $z \lesssim 6$ (Matejek & Simcoe 2012; Chen et al. 2017; Bosman et al. 2017). The observed distribution agrees with the model prediction of a shallow decrease in line density with redshift at $z > 6$.

Focusing on all the detected Mg II systems including both strong- and weak lines, we derive the rest-frame equivalent width distribution described by a powerlaw function

$$\frac{dn}{dW} = \frac{n_*}{W_*} \exp(-W/W_*) \quad (6)$$

where dW is the rest-frame equivalent width increment. We do not include a redshift dependence, since the line density is constant with redshift. The best fit parameters are $W_* = 0.758$ and $n_* = 1.82$. Figure 9 presents the distribution compared to a large quasar sample examined in Chen et al. (2017), and compared to

Table 5. Si II $\lambda 1526$ systems

Quasar	z_{abs}	$W_{\text{rest}} (\text{\AA})$
VDES J0020–3653	5.4695	0.028 ± 0.011
VDES J0020–3653	5.7910	0.074 ± 0.014
VDES J0020–3653	6.4535	0.028 ± 0.012
VDES J0020–3653	6.5625	0.059 ± 0.012
VDES J0020–3653	6.6690	0.092 ± 0.013
DELS J0411–0907	5.9350	0.143 ± 0.010
DELS J0411–0907	6.1774	0.127 ± 0.008
UHS J0439+1634	5.8190	0.047 ± 0.006
UHS J0439+1634	6.2840	0.286 ± 0.009
ULAS J1342+0928	6.8427	0.186 ± 0.012
ULAS J1342+0928	7.3680	$< 0.03^\dagger$
ULAS J1342+0928	7.4430	0.018 ± 0.010

[†]The Si II $\lambda 1526$ line is not detected in the spectrum, but the system is nevertheless included in the analysis since both Si II $\lambda 1260$ and Si II $\lambda 1304$ are detected at this redshift.

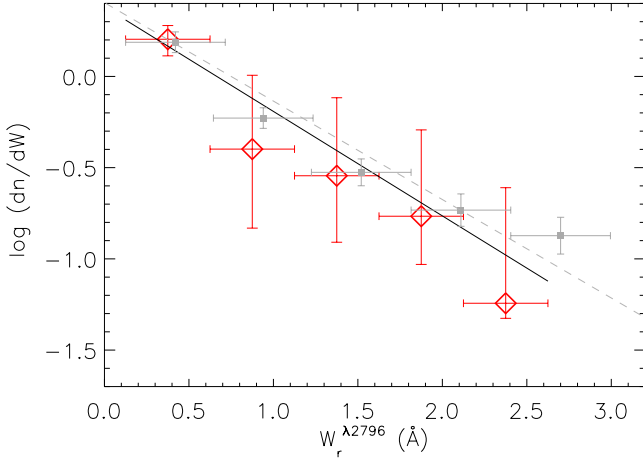


Fig. 9. Distribution of Mg II equivalent widths from all systems across the redshift interval from $z = 2.5 - 7.5$. The best fit is illustrated by the solid line. Compared to much larger quasar surveys at lower redshifts (Chen et al. 2017), where the dashed line is the best fit, there is no evidence for a different distribution in the NIRSpec data.

ground-based observations, we see no evidence for a change in the W_r distribution in the NIRSpec spectra.

Strong Mg II $\lambda 2796$ absorption lines with rest-frame $W_r > 1 \text{ \AA}$ have received particular attention since these absorbers are found to have the same redshift evolution as that derived from the integrated [O II] luminosity of galaxies and are proposed to trace the cosmic star-formation rate density at $z \approx 1$ (Prochter et al. 2006; Ménard et al. 2011). It is therefore relevant to investigate the strongest Mg II lines at the highest redshifts with the new NIRSpec data. We identify 11 strong Mg II $\lambda 2796$ absorbers with $W_r > 1 \text{ \AA}$ listed in Table 6. The line density dn/dX is illustrated in Fig. 10. Since we only have four JWST spectra, small-number Poisson statistics dominate the uncertainties (Gehrels 1986), but overall we see that the line density is consistent with other high-redshift quasar and gamma-ray burst afterglow samples that find a decrease in strong $W_r > 1 \text{ \AA}$ systems at $z > 3$ (Chen et al. 2017; Christensen et al. 2017; Zou et al. 2021). None of the absorbers detected at $z > 7$ fall in the strong-line category.

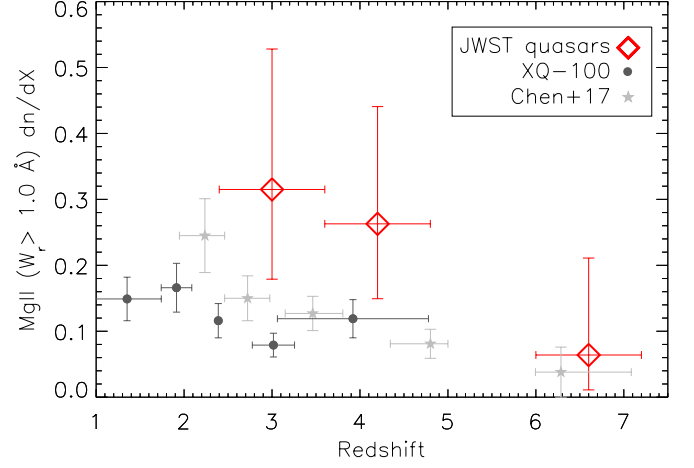


Fig. 10. Strong Mg II $\lambda 2796$ absorption line densities for systems with $W_r > 1 \text{ \AA}$. The JWST data are compared with the strong Mg II line densities in a large quasar sample (Chen et al. 2017) and with the XQ-100 survey (Christensen et al. 2017), and are consistent with a decrease in the line densities to the highest redshifts.

Table 6. Strong Mg II systems

Quasar	z_{abs}	$W_{\text{rest}} (\text{\AA})$
VDES J0020–3653	3.4087	2.72 ± 0.02
VDES J0020–3653	3.6040	1.39 ± 0.02
VDES J0020–3653	4.0738	2.08 ± 0.02
DELS J0411–0907	2.5771	1.77 ± 0.02
DELS J0411–0907	3.4290	1.79 ± 0.02
DELS J0411–0907	3.7760	1.00 ± 0.02
DELS J0411–0907	4.2815	2.54 ± 0.01
UHS J0439+1634	3.1700	1.31 ± 0.01
UHS J0439+1634	4.5230	1.16 ± 0.01
ULAS J1342+0928	3.3758	1.48 ± 0.02
ULAS J1342+0928	6.8427	1.38 ± 0.04

4.4.5. C IV absorbers

Turning to the high-ionization transitions, we identify 17 C IV $\lambda \lambda 1548, 1550$ absorption systems at $5.20 < z < 6.86$ in our spectra as listed in Table 7. The total path length interval for C IV is $\Delta X = 30.8$. Two of the absorbers lie closer than 3000 km s^{-1} from the quasar systemic redshifts, and are excluded in the computation of absorption line density shown in Figure 11. The NIRSpec data reveal that the C IV line density continues to decrease with redshift beyond $z > 6$. Compared to the observed line densities, the model predicts a much lower line density. This discrepancy was also noted in D’Odorico et al. (2022), who discussed the mismatching C IV as a problem in the models in Finlator et al. (2020). If models are forced to match the line density of C IV, then the line densities for Si IV would be over-predicted.

4.4.6. Si IV absorbers

In the spectrum of ULAS J1342+0928 we detect a candidate Si IV $\lambda 1393$ line at $z = 6.476$, which is also detected in C IV. The spectrum does not clearly reveal the fainter Si IV $\lambda 1402$ line. In the spectrum of J0439+1634 we detect a single Si IV doublet, also reported by Davies et al. (2023a), but we note that both transitions in this doublet lie at the wings of two broad absorption

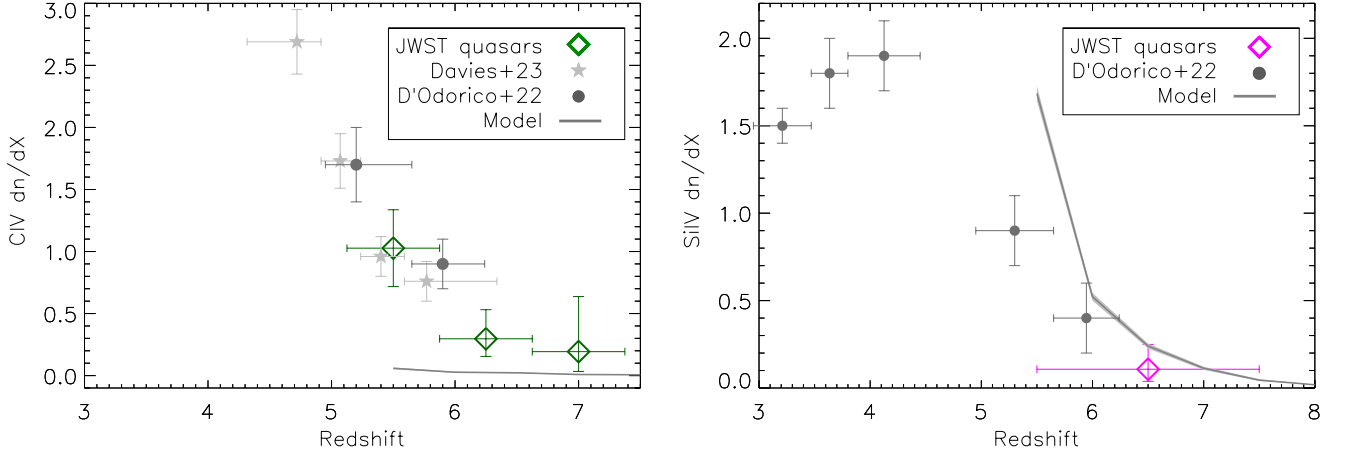


Fig. 11. Line densities of high-ionization lines. The left hand panels shows the CIV absorption line densities with $W_r > 0.05$ Å. The CIV line densities at the highest redshifts from the E-XQR-30 survey (D’Odorico et al. 2022) are illustrated for comparison. The same E-XQR-30 data set was analysed in Davies et al. (2023b) and has been corrected for incompleteness. The right hand panel shows SiIV absorption line densities. The SiIV line densities for systems with $W_r > 0.03$ Å from D’Odorico et al. (2022) are illustrated for comparison.

Table 7. CIV systems

Quasar	z_{abs}	W_{rest} (Å)
VDES J0020–3653	5.2005	0.044±0.008
VDES J0020–3653	5.3275	0.170±0.008
VDES J0020–3653	5.4699	0.228±0.013
VDES J0020–3653	5.7913	0.357±0.014
VDES J0020–3653	6.5030	0.070±0.013
VDES J0020–3653	6.8550 [†]	0.201±0.007
DELS J0411–0907	5.4258	0.052±0.009
DELS J0411–0907	5.9349	0.067±0.009
UHS J0439+1634	5.2740	0.179±0.007
UHS J0439+1634	5.3945	0.808±0.006
UHS J0439+1634	5.3945	0.808±0.006
UHS J0439+1634	5.5228	0.108±0.007
UHS J0439+1634	5.7360	0.123±0.006
UHS J0439+1634	6.2840	0.390±0.007
UHS J0439+1634	6.4877 [†]	0.238±0.004
ULAS J1342+0928	5.8888	0.263±0.010
ULAS J1342+0928	6.7490	0.103±0.010

[†]These absorption systems lie within 3000 km s^{−1} of the quasar systemic redshift and are excluded from the line density computation.

line features in the quasar spectrum. These absorbers are listed in Table 8.

The total path length for SiIV systems in the JWST spectra is $\Delta X = 18.60$. Fig. 11 compares the SiIV line density from the highest redshift NIRSpec data to the lower redshift measurements of D’Odorico et al. (2022). As for the CIV systems, SiIV line densities are known to exhibit a rapid decrease in line density at $z > 5$ (D’Odorico et al. 2022), which we confirm with our very few detections of SiIV absorption lines.

4.4.7. Ca II and Na I lines

Most of the strong absorption lines arising in the ISM, CGM and IGM are from rest-frame UV lines, but the extended NIR wave-

Table 8. SiIV $\lambda 1393$ systems

Quasar	z_{abs}	W_{rest} (Å)
UHS J0439+1634	6.173	0.096±0.007
ULAS J1342+0928	6.746	0.041±0.012

length coverage of the NIRSpec Band III G395H data allows us to search for rest-frame optical absorption lines associated with any of the absorption systems. Since the ionization potential of Ca II $\lambda\lambda 3934, 3969$ and Na I $\lambda\lambda 5891, 5897$ is less than that of hydrogen, these absorption lines arise in neutral regions and are frequently associated with dusty absorbers at lower redshifts detected in quasar spectra ($z \lesssim 1$) (Heckman et al. 2000; Wild et al. 2006). Weak and strong Ca II absorbers, with a division at $W_r = 0.7$ Å, probe either galaxy disc gas or halo-components, respectively (Fang et al. 2023). We detect Ca II lines in three absorption systems at $z = 3.17, 3.631$, and 3.37 , however, the signal is not sufficient to recover both lines in the doublet in any of the systems. Two of the absorbers fall into the weak line category with $W_{r,3934} < 0.7$ Å, while the $z = 3.631$ system towards ULAS J1342+0928 is a strong one.

The other rest-frame optical line of interest, the doublet Na I $\lambda\lambda 5891, 5897$ is covered by the Band III data for the highest redshift absorbers. However, as discussed in Section 2, the statistical errors on the Band III portions of the spectra are poorly defined. We therefore choose to only focus on absorption line systems that were identified in the Bands I and II Fixed Slit data, and test whether an associated Na I doublet is present in any of the $z > 3.9$ systems. Only a single high-redshift absorber at $z = 5.6814$ towards ULAS J1342+0928 has a potential Na I absorption line doublet detection.

4.5. Combined line density redshift evolution

To compare the evolution of the atomic species, all the line densities in previous subsections are combined in Fig. 12, which shows the evolution with redshifts for different elements derived in the literature with an extension to the highest redshifts

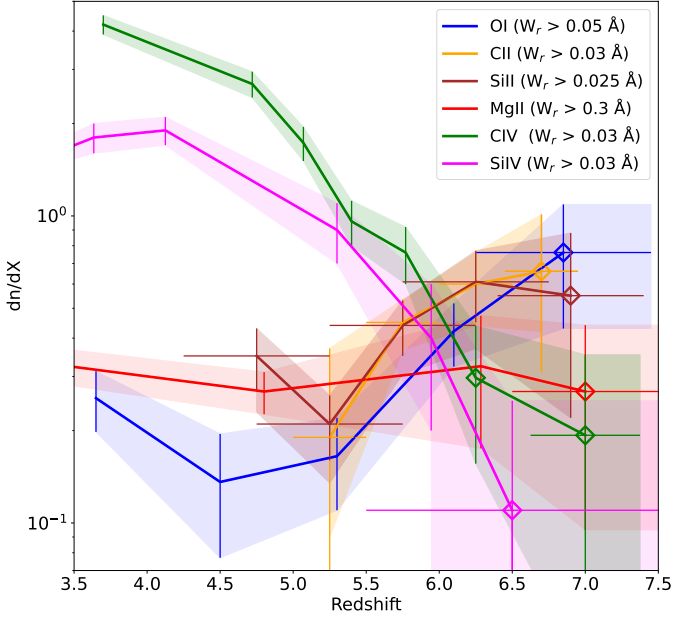


Fig. 12. Comparison of the redshift evolution of the line densities of O I $\lambda 1302$, C II $\lambda 1334$, Si II $\lambda 1526$, Mg II $\lambda 2796$, C IV $\lambda 1548$, and Si IV $\lambda 1393$. The highest redshift data points for each of the colored curves represent the NIRSpec analyses in this work, extending from the lower-redshift line densities from O I (Becker et al. 2019), Si II and C II from the catalog in Davies et al. (2023a), C IV (D’Odorico et al. 2022; Davies et al. 2023b), Si IV (D’Odorico et al. 2022), and Mg II (Chen et al. 2017).

($z > 6.0$) detected in the NIRSpec data. All the computed line densities from the JWST data are listed in Table 9.

Both C IV and Si IV experience a drastic drop in line densities continuing at the highest redshifts ($z > 6.5$) detected in the NIRSpec data, while the line densities of the low-ionization species O I and C II continue to increase at these redshifts. The evolution of Si II from low redshift ($z < 5$) is not constrained, and with the large uncertainties from the NIRSpec data, the Si II line density could be constant at the redshifts covered in this work, but could also trace the same increase in line density as detected for O I and C II. The transition in line densities of both carbon and silicon from predominantly low-ionization at high redshifts to high-ionization species at low-redshifts occurs at $z \approx 6.0$. In contrast, the line density of Mg II remains constant throughout the range from $z = 3$ to $z = 7$, or may even experience a shallow decline towards higher redshifts as predicted by the model.

5. Metal abundances

5.1. Metal abundance ratios

The spectral resolution and sampling (Section 2) of our NIRSpec spectra is insufficient to accurately model the absorption line profiles via Voigt profile fitting techniques with the aim of deriving column densities for the different ions. However in simple cases, we can extract the same information from the measurements of the rest-frame equivalent widths. In the optically thin regime when the optical depth is $\tau_\lambda \ll 1$, the column density N scales linearly with the rest-frame equivalent width (Spitzer 1978):

$$N = 1.13 \times 10^{20} \frac{W_r(\text{\AA})}{f\lambda^2(\text{\AA})} [\text{cm}^{-2}], \quad (7)$$

where f is the oscillator strength, and λ the rest-frame transition wavelength.

We derive the relative abundances assuming that the singly ionized atoms and neutral oxygen are the dominant state of ionization in the absorption systems. This is a reasonable assumption, since none of the systems with O I absorption show any associated high-ionization transitions. Moreover at the highest redshifts, the metallicities are expected to be low, so the optical depths of the transitions are low too. Finally, the column density ratios are compared to the solar photosphere abundances in Asplund et al. (2021). The silicon-to-oxygen and carbon-to-oxygen ratios are computed as:

$$[\text{Si}/\text{O}] = \log\left(\frac{N_{\text{SiII}}}{N_{\text{OI}}}\right) - \log\left(\frac{N_{\text{Si}}}{N_{\text{O}}}\right)_\odot \quad (8)$$

$$[\text{C}/\text{O}] = \log\left(\frac{N_{\text{CII}}}{N_{\text{OI}}}\right) - \log\left(\frac{N_{\text{C}}}{N_{\text{O}}}\right)_\odot, \quad (9)$$

where the solar values are $\log\left(\frac{N_{\text{Si}}}{N_{\text{O}}}\right)_\odot = -1.18 \pm 0.05$ and $\log\left(\frac{N_{\text{C}}}{N_{\text{O}}}\right)_\odot = -0.23 \pm 0.06$ (Asplund et al. 2021).

5.2. Pop III enrichment signatures in [Si/O]

To date, no secure discovery of metal-free Pop-III stars has been made and the nature of the first generation of stars remains unknown. Pop-III stars leave behind a signature in the form of distinct metal-abundance patterns created by the stellar explosions of the massive stars. These patterns make their imprint on the chemical abundances of extremely metal-poor halo stars in the Milky Way (e.g. Frebel & Norris 2015), but also absorption line systems at high redshifts can be used to trace the nature of the first stars, since the time span for metal-enrichment of gas in the Universe is small.

In this section we focus on the six systems at $z_{\text{abs}} > 6.5$ with identified O I $\lambda 1302$ absorption lines in Table 3. Since no high-ionization lines are detected in these absorption systems, they are predominantly neutral and we do not require ionization corrections to derive metal abundance ratios. We examine whether the absorption lines are likely to be intrinsically saturated. Even though the spectra in Figures B1–B61 in Appendix B suggest that none of the lines are saturated, at the low spectral resolution some lines could have hidden saturation. Indeed some of the lower-redshift strong absorption lines like the strong Mg II lines are clearly saturated. For each of the absorption line systems we construct a conventional curve-of-growth with a best fit Doppler parameter between 20 and 40 km s⁻¹ from unblended Si II lines, where two or three separate transitions are detected. For the uncontaminated O I, C II, and Fe II lines, we verify that the transitions in W_r/λ vs. $Nf\lambda$ fall on a straight line in the linear, non-saturated part of the curve of growth. This confirms that most lines are not saturated and that we can reliably derive the metal abundance ratios listed in Table 10.

Figure 13 shows the abundance ratios in a diagram of [Si/O] vs. [C/O] for the six $z > 6$ O I absorbers in our sample. Since C II in two of the six absorbers is partly contaminated by other absorption lines at other redshifts, and one is not detected, we provide only upper limits for three [C/O] ratios.

To compare the observed abundance pattern with the chemical enrichment from various types of stellar explosions, Figure 13 illustrates the predicted ratios where the combined yields are weighted by the number of stars in a Salpeter initial mass

Table 9. Compilation of line densities for all elements from the NIRSpec data. Column (2) presents the redshift range, (3) the absorption path-length interval, (4) the number of detected absorbers, and (5) the line density.

Element (1)	z (2)	ΔX (3)	n (4)	dn/dX (5)
O I $\lambda 1302$ ($W_r > 0.03 \text{ \AA}$)	6.25 – 7.45	6.60	6	$0.91^{+0.54}_{-0.36}$
O I $\lambda 1302$ ($W_r > 0.05 \text{ \AA}$)	6.25 – 7.45	6.60	5	$0.76^{+0.51}_{-0.33}$
C II $\lambda 1334$ ($W_r > 0.03 \text{ \AA}$)	5.95 – 7.45	10.64	6	$0.66^{+0.35}_{-0.24}$
Si II $\lambda 1526$ ($W_r > 0.025 \text{ \AA}$)	5.1 – 6.3	17.60	6	$0.45^{+0.22}_{-0.16}$
Si II $\lambda 1526$	6.3 – 7.5	10.96	6	$0.55^{+0.33}_{-0.22}$
Si IV $\lambda 1394$ ($W_r > 0.03 \text{ \AA}$)	5.5 – 7.5	18.60	2	$0.11^{+0.14}_{-0.07}$
C IV $\lambda 1548$ ($W_r > 0.05 \text{ \AA}$)	5.13 – 5.88	10.70	11	$1.03^{+0.31}_{-0.31}$
C IV $\lambda 1548$	5.88 – 6.63	13.49	4	$0.30^{+0.23}_{-0.14}$
C IV $\lambda 1548$	6.63 – 7.38	5.19	1	$0.19^{+0.44}_{-0.16}$
Mg II $\lambda 2796$ ($W_r > 0.3 \text{ \AA}$)	2.5 – 3.5	13.30	8	$0.60^{+0.30}_{-0.21}$
Mg II $\lambda 2796$	3.5 – 4.5	15.27	7	$0.46^{+0.25}_{-0.17}$
Mg II $\lambda 2796$	4.5 – 5.5	17.36	4	$0.23^{+0.18}_{-0.11}$
Mg II $\lambda 2796$	5.5 – 6.5	18.56	8	$0.43^{+0.21}_{-0.15}$
Mg II $\lambda 2796$	6.5 – 7.5	7.49	2	$0.27^{+0.35}_{-0.17}$

function (IMF), reflecting the combined enrichment pattern generated by a stellar population. Pop III pair-instability SNe (PISN) with initial masses of $140\text{--}260 M_\odot$ are illustrated by red coloured contours, and occupy a distinct region with a high [Si/O] and low [C/O] ratio (Heger & Woosley 2002). Pop III hypernovae (shown in green contours) and Pop III supernovae (blue contours) with a range of energies and initial masses of $10\text{--}100 M_\odot$ also display distinct abundance patterns (Heger & Woosley 2010). Hypernovae are defined as having explosion energies of $> 10^{52}$ erg, roughly ten times more than that of core-collapse SNe.

Several theoretical works have computed yields from metal-enriched Pop II. Using the yields table in Nomoto et al. (2013), stars with initial stellar masses between $10\text{--}40 M_\odot$ and $5\%\text{--}100\%$ solar metallicity (illustrated in gray color in Fig. 13) produce an abundance pattern that overlaps with that of hypernovae. The yields in Kobayashi et al. (2006) gives more or less identical results. A more recent yields table that includes Pop II stars with higher initial stellar masses between $13\text{--}120 M_\odot$ (Limongi & Chieffi 2018) (purple contours) produce an IMF weighted yield with a higher concentration around [C/O] ≈ 0.1 and [Si/O] ≈ 0.3 .

Variations of abundance ratios from Pop III and Pop II stellar yields have been used to infer the enrichment patterns predicted in Gamma-ray burst hosts (Ma et al. 2017), observed in low-metallicity absorption-line systems (Cooke et al. 2017; Welsh et al. 2019, 2023), and used to predict the yields in absorbers at the highest redshifts (Jeon et al. 2019). Stars in the local Universe also retain chemical signatures originating from the first populations of stars reflecting distinct abundance ratio patterns (Vanni et al. 2023a,b; Salvadori et al. 2023). See also Ma et al. (2017), Vanni et al. in prep and D’Odorico et al. in prep. for abundance ratio diagrams other than [Si/O] and [C/O].

Figure 13 illustrates that also other intervening absorption-line systems at $4.5 < z < 6$ (orange circles) (Becker et al. 2019; Cooper et al. 2019) fall in the same region as the JWST absorption systems. However, several of these other absorption line systems at $z < 5$ have detected Si IV and C IV absorption lines that display different kinematical profiles and therefore arise in a different medium than the low-ionization lines (Becker et al. 2019). In such cases a direct conversion from W_r of Si II and C II to a total Si and C column density is not valid. In fact, some of

the absorption systems at $z < 4.2$ in Becker et al. (2019) have hydrogen column densities $N(\text{H I}) < 10^{20} \text{ cm}^{-2}$ for which ionization corrections are necessary, and when these are included, all the absorbers at $3.0 < z < 4.2$ have [Si/O] < 0.4 (Saccardi et al. 2023). For seven absorption systems at $5 < z < 6.2$ their [Si/O] ratios without ionization corrections remain close to the solar value (Becker et al. 2012), suggesting that Pop III enrichment does not dominate these systems.

In higher H I column density Damped-Ly α systems (DLAs), where the hydrogen column density is $N(\text{H I}) > 2 \times 10^{20} \text{ cm}^{-2}$, the clouds are self shielded, such that the dominant contributions to the metal column densities are from the low-ionization species. Above metallicities of 1% solar, C, N, O absorption lines are saturated in DLA systems and only lower limits on the column densities can be derived (e.g. Berg et al. 2016). The gray circles in Fig. 13 illustrate that metal-poor DLAs at $z_{\text{abs}} \sim 3$ with metallicities from 10^{-3} to $10^{-2} Z_\odot$ in oxygen (Cooke et al. 2011, 2017; Welsh et al. 2019) generally have abundance patterns similar to solar values and consistent with Pop II SNe enrichment patterns, albeit with an overlap from the high-mass Pop III hypernovae enrichment pattern. However, when analysing other elements (Fe and Al), one of the DLA systems has an enrichment pattern which is better matched by Pop III SNe (Cooke et al. 2017; Welsh et al. 2023).

For the three absorption systems detected by NIRSpec with limits on the carbon abundance the enrichment could possibly be created by Pop III PISN. Two of the other absorbers show abundance ratios with high values of [Si/O] that are consistent with either enrichment by primarily lower mass ($< 15 M_\odot$) Pop III hypernovae or even Pop III core-collapse SNe for one of them. Models predict that the abundance ratio $0.5 < [\text{Si}/\text{O}] < 1.0$ is produced by energetic Pop III SNe (with explosion energies $> 10^{51}$ erg) from stars with initial stellar masses in the range from $10\text{--}15 M_\odot$ (Heger & Woosley 2010). However, also single $15 M_\odot$ star Pop II explosions produce a high [Si/O] ≈ 0.5 ratio (Woosley & Weaver 1995; Thielemann et al. 1996; Nomoto et al. 2006, 2013), so the enrichment by a single Pop II star remains a possibility. We do have to consider that gas clouds seen in absorption may not only be polluted by a single star alone, but by several SNe explosions over a range of stellar masses. When in-

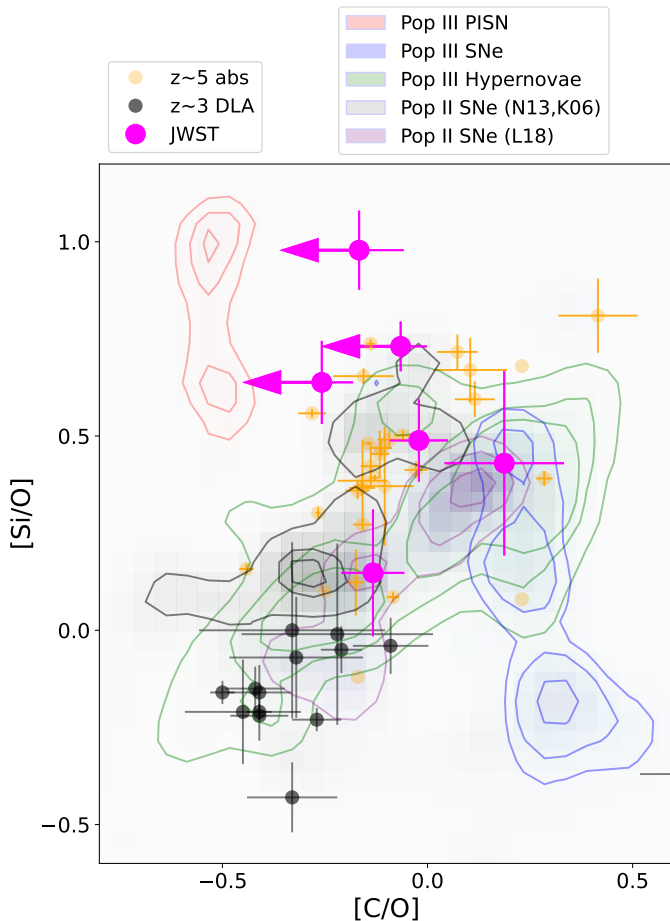


Fig. 13. Abundance ratios of [Si/O] versus [C/O]. The background colored map with contours illustrates the metal yields from different stellar explosions colored as follows: *Red region:* Pop III Pair-instability Supernovae (PISN), *Green:* Pop III Hypernovae, *Blue:* Pop III Core-collapse Supernovae, *Gray and Purple:* Pop II Supernovae. Yields from the different stellar populations are scaled assuming a Salpeter IMF. The *Magenta circles* illustrate that the NIRSpc absorption systems listed in Table 10 have values of [Si/O] similar to Pop III models, although some overlap with the yields of a single $15 M_{\odot}$ Pop II star. Other intervening absorption-line systems at $4.5 < z_{\text{abs}} < 6$ (Becker et al. 2019; Cooper et al. 2019) (*orange circles*) fall in the same region of the abundance pattern space, whereas the *gray circles* representing very metal-poor damped Ly α absorbers at $z_{\text{abs}} \sim 3$ (Cooke et al. 2011, 2017; Welsh et al. 2019) are also consistent with enrichment of Pop II core collapse SNe (Kobayashi et al. 2006; Nomoto et al. 2013; Limongi & Chieffi 2018, annotated as K06, N13, and L18).

tegrating the yields over the IMF, stars with masses in the range from $13 - 40 M_{\odot}$ with initial population metallicities less than solar all produce an integrated ratio of $[\text{Si}/\text{O}] \lesssim 0.1$ (Woosley & Weaver 1995; Kobayashi et al. 2006; Nomoto et al. 2013).

6. Transmission spikes in the Gunn-Peterson trough

One of the most debated questions arising from studies of the high-redshift Universe in the past decades, is what sources reionized the IGM? To further investigate this, we examine whether the sources associated with metal absorbers have ionized their surroundings.

We investigate the narrow transmission spikes at $z > 5.7$ in the Ly α forest region and in the GP troughs covered by the NIR-

Table 10. Metal abundance ratios of absorption systems

Quasar	z_{abs}	[Si/O]	[C/O]
ULAS J1342+0928	7.3680 [†]	0.98 ± 0.10	$< -0.17 \pm 0.11$
ULAS J1342+0928	7.4430	0.43 ± 0.24	0.19 ± 0.15
VDES J0020–3653	6.4535	0.15 ± 0.16	-0.13 ± 0.08
VDES J0020–3653	6.5625 [†]	0.64 ± 0.11	< -0.26
VDES J0020–3653	6.6690	0.49 ± 0.11	-0.02 ± 0.07
UHS J0439+1634	6.2880 [†]	0.73 ± 0.06	$< -0.07 \pm 0.06$

[†]Upper limits for [C/O] are computed because the column densities of carbon lines are overestimated due to line contamination from other systems, or an upper detection limit on C II in the case of the $z = 6.5625$ system.

Spec data using the normalized quasar spectra bluewards of the quasars Ly α lines described in Sect. 3.2. To locate narrow transmission spikes we search for peaks with a $3\text{-}\sigma$ prominence above zero, using the normalized spectrum divided by the normalized noise spectrum, i.e. a spectrum of the S/N ratio. We require that the peaks extend over three or more pixels to avoid detections from a single noisy pixel. The identified spikes have relative transmissions of 2–5% or higher. Figure 14 illustrates the location of the Ly α wavelengths for the identified metal-absorption line system redshifts plotted on the normalized spectrum in the GP trough region of the four spectra. The blue and red colored dashed lines mark high- and low-ionisation absorption systems, respectively. The green triangles mark the spikes in the IGM where there is a significant transmission of Ly α photons, and Table 11 lists the redshifts of the encountered Ly α transmission spikes.

We briefly compare the detected IGM transmission spikes with previously published results. Yang et al. (2020) examine transmission spikes at $z > 5.5$ based on ground-based spectra of a large sample of high-redshift quasars including two of the quasars in this paper (DELS J0411–0907 and VDES J0020–3653). They list four spikes in DELS J0411–0907, with three being multiple peaks at an almost identical redshift of $z \sim 5.7$. We also detect these four spikes in the NIRSpc data but in addition we also detect spikes at even higher redshift. For VDES J0020–3653, Yang et al. (2020) do not report spike redshifts. Due to the higher S/N ratio of the JWST spectra and the absence of noise due to telluric features, we can detect weaker spikes in the GP troughs.

Only a single low-ionization absorption system (at $z = 5.928$ towards UHS J0439+1634) out of the total of 13 intervening low-ionization absorption systems (red dashed lines in Fig. 14) match the transmission spikes in the IGM to within a velocity offset of 2000 km s^{-1} , whereas four out of nine of the high-ionization system lie within $\approx 2000 \text{ km s}^{-1}$ of transmission spikes, all of which at $z \sim 5.8$. Not surprisingly, the two proximate absorption systems in the spectra of UHS J0439+1634 and VDES J0020–3653 are indeed high-ionization systems. Conversely, from the total of 21 absorption systems at $z > 5.7$, 16 spikes do not match any metal-absorption system within $\pm 2000 \text{ km s}^{-1}$. The fact that most of the low-ionization systems are not associated with a transmission spike supports the hypothesis that the metal-enrichment arises from star-formation followed by heavy element productions by supernova explosions preferentially in higher density regions that may be the last regions to be reionized (Oh 2002). On the other hand, half of the high-ionization systems at $5.7 < z < 6.8$ appear in regions of the

Table 11. Redshifts of transmission spikes in the GP troughs

Quasar	z_{spikes}
ULAS J1342+0928	5.9214
VDES J0020–3653	5.7333, 6.0125
DELS J0411–0907	5.7178, 5.8497, 5.9059 5.9756, 6.2781, 6.5127
UHS J0439+1634	5.70232, 5.7702, 5.8787 5.9117, 6.1017

IGM that are ionized to a degree that allows the escape of Ly α photons.

7. Discussion

7.1. A forest of lines or discrete absorption line systems?

Oh (2002) has suggested that as the Universe becomes progressively more neutral, a forest of weak metal lines may appear at redshifts close to the EoR. Analogous to the H I Ly α forest arising from neutral clouds of hydrogen in the IGM that becomes more numerous towards higher redshifts, metals in the IGM would also progressively become more neutral. For example an O I λ 1302 forest could give rise to a depression of the quasar continuum at the 10–20% level (Oh 2002). Other atoms such as C II, or Si II have ionization potentials close to that of H I and have oscillator strengths that also make the lines useful as tracers of the enrichment and the increasing neutral IGM towards the reionization epoch. Likewise, the Mg II λ 2796,2803 doublet is easily detected, and could give rise to a continuous Mg II forest provided the neutral IGM is globally enriched with metals (Hennawi et al. 2021). However, ground-based spectra of high redshift quasars have not yet revealed any signature from a Mg II forest (Tie et al. 2023). In the NIRSpec data we detect a line density of Mg II that remains constant out to $z = 7.5$. Mg II lines are identified as discrete absorption systems rather than a global decrease in the continuum in the form of a Mg II forest. Also in the case of O I, we are only able to detect discrete absorbers that likely arise in the CGM or ISM of intervening galaxies. Further analysis of JWST/NIRSpec data using more advanced methods such as auto-correlation techniques may be able to find a metal forest, but that is beyond the scope of the analysis of individual absorption systems in this work. Detecting a Mg II metal-line forest with a global decrease in the continuum flux at the few percent level is difficult due to the wiggles in the NIRSpec data described in Section 2, but also the broad emission-line composite from Mg II and Fe II in the quasar spectrum will make it difficult to accurately determine the level of the unabsorbed continuum emission.

7.2. High-redshift metallicities

In the absence of measurable H I column densities, we can only measure relative metallicities. In the redshift interval $2 < z < 6$ absorption systems display a relatively constant relative abundance pattern in [Si/O] and [C/Fe] with redshift and do not reveal clear signatures of Pop III SNe enrichment (Becker et al. 2012; Kulkarni et al. 2014), with a couple of possible exceptions from DLA systems at $z \approx 3$ (Welsh et al. 2023). A relevant question is therefore if we have overestimated the [Si/O] or [C/O] ratios for the $z > 6$ absorption systems. In comparison with ground-based

spectroscopic studies, the NIRSpec data have low spectral resolution and could potentially have hidden saturation, or be composed of multiple components rather than a single one assumed for the O I systems in this work. We argue against the possibility of hidden saturation based on the analysis of the curve of growth for the absorption lines in any of the O I absorbers where we find that they are consistent with being on the linear, optically thin region of the curve of growth. In agreement with our finding, numerical simulations at $z \sim 7$ also find that O I absorption lines along random sight-lines are optically thin (Doughty & Finlator 2019).

Alternatively, multiple absorption components in the observed spectra could have variations in abundance patterns between them, but in order to display a high [Si/O] ratio, some of the components will inevitably have to have an extreme value. Ultimately, we need higher spectral resolution measurements to reveal and decompose the absorption lines in distinct components but this may have to wait until the arrival of high-resolution spectrographs on future extremely large telescopes (e.g. Maiolino et al. 2013).

Another possibility leading to inaccurate abundance ratios arises if the atoms exist predominantly in ionization states other than Si II or C II in which case ionization corrections are needed to derive [Si/O] and [C/O] ratios accurately. However, we do not regard this as likely for following reasons. Firstly, the intervening absorption systems are primarily neutral because there are no high-ionization C IV or Si IV lines associated with the O I systems. Secondly, the O I absorbers are not associated with a transmission spike in the GP troughs at these redshifts, and consequently the environment is predominantly neutral. O I is charge-exchanged locked with H I, so O I is the dominant state of oxygen. Possibly, Si III and C III could be present, but these atomic states do not have absorption lines in the spectral range covered by the NIRSpec data. However, if that were the case, then the total [Si/O] and [C/O] would be even higher than detected in the high-redshift absorbers. For similar $z \sim 6$ absorption systems, Cooper et al. (2019) argue that the low-ionization systems are equivalents to $z \sim 3$ DLA systems in which metallicities derived without ionization corrections are reliable.

7.3. Ionization state of the CGM

Our finding that the number density of the high-ionization ions C IV and Si IV continues to drop at $z > 6.5$ extends the trends observed at slightly lower redshifts (Cooper et al. 2019; D’Odorico et al. 2022; Davies et al. 2023b). The disappearing of these absorption lines cannot be attributed to a change in metallicity, since C II and Si II are frequently detected with column densities that are ten times higher than in the high-ionization states (Becker et al. 2011; Bosman et al. 2017; Cooper et al. 2019). Moreover, we find that the Mg II line density appears to be constant throughout the redshift range probed out to $z \sim 7.5$, or at least only display a modest decrease to the highest redshifts covered, $z \sim 7.5$. This supports the contention that the change in the high-ionization line densities is caused by a softening of the UV radiation field dominated by star-forming galaxies rather than by the harder radiation of active galactic nuclei at these redshifts.

The under-production of C IV at $z > 6$ is known to be a problem in cosmological simulations (Keating et al. 2016; Finlator et al. 2018; Doughty et al. 2018) although interestingly we find that the number density of C II absorbers agrees with observations. We detect only two Si IV absorbers in the JWST spectra, and confirm that the line density of this transition continues to decrease with redshift consistent with model predictions. The

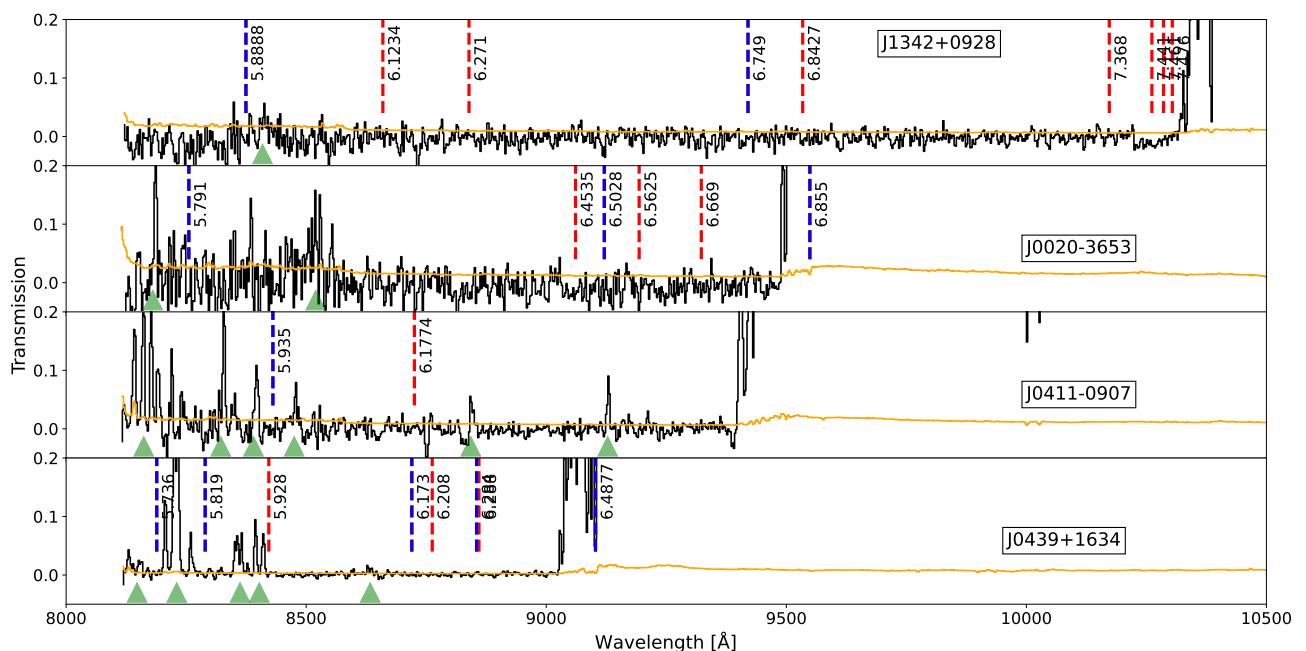


Fig. 14. The panels show the relative transmission in the GP trough after normalizing the spectra to a model of the quasar continuum in the Ly α forest. The individual absorber redshifts are marked where their expected Ly α wavelength falls. Red dashed lines are absorbers that are only low-ionization systems, and blue dashed lines mark absorbers with high-ionization lines from C iv. Two of the absorbers lie close to the quasar redshift, and their Ly α wavelengths fall in the proximity region of the quasar spectrum. A single low-ionization absorber at $z = 5.928$ is associated with a transmission spike in the intervening IGM illustrated by the green triangles, while four of the high-ionization absorbers lie within ± 2000 km s $^{-1}$ from the IGM transmission spikes at $z \sim 5.8$.

fact that the observed line density of Si iv at $z > 5.5$ matches the simulations (D’Odorico et al. 2022), whereas the observed Si ii line density is higher than in simulations, is not likely due to the hardness of the UV background in the simulations, because the ratio of these lines does not depend on the spectral hardness (Doughty et al. 2018). In the epoch where reionization has not yet been completed, the low-ionization ions will be the dominant ones, and may be present out to large distances from the galaxies (Doughty & Finlator 2023).

7.4. Environments of the metal absorbers

To date, not many studies have attempted to match metal-absorption lines to galaxies at $z > 6$ primarily due to the lack of instrument sensitivity since the galaxies are very faint. From ground-based observations, targeting Ly α emitters has recently been the best option due to the increased contrast of the emission lines above the background. By studying correlations of high-ionization C iv systems at $z \sim 5$ with Ly α emitters Díaz et al. (2021) found emitters within 200 kpc in projection from the absorbers. The environments of the even higher redshift low-ionization systems are less clear from observations. Using JWST/NIRcam slitless spectra of one $z = 6.3$ quasar field Kashino et al. (2023) identify galaxies with [O iii] emission lines at $5.3 < z < 6.2$ and find that most of the detected galaxy redshifts match either high- or low-ionizations absorption-line systems in the quasar spectrum. Conversely, out of the eight intervening absorption line systems, only four of the systems have detected galaxies within 200 kpc of the quasar sight line (Kashino et al. 2023), where most of the non-detections are from low-ionization absorber systems.

In a survey of eight quasars at $z > 6$, Meyer et al. (2020) detect a weak correlation between transmission spikes and $z \approx 6$

Ly α -emitters and Lyman-break galaxies (LBGs) within 1–10 proper Mpc in projection along the line of sight, but argue that fainter galaxies below the detection threshold are necessary to drive the reionization. In a similar analysis of a single quasar at $z = 6.4$ Kakiichi et al. (2018) find that three out of six LBGs lie close in redshift space to the IGM transmission spikes, and also conclude that fainter galaxies clustered around the brighter LBGs are needed to drive reionization, but also argue that luminous quasars do contribute to the ionizing flux at the latest stages of the reionization. In a recent analysis of JWST NIRcam slitless data, Kashino et al. (2023) measure a clear correlation between galaxy redshifts at $5.7 < z < 6.1$ and transmission spikes in the Ly α forest, but find that metal-absorption systems are not connected to the transmission spikes. This is consistent with our finding of no clear association of low-ionization absorbers with IGM transmission peaks.

Whether any of the absorption systems have detectable galaxy counterparts nearby can be investigated with the Band III JWST integral field spectra. The 3 arcsec field of view of the IFU limits the search to within 7–10 kpc in projection from the quasar, which is much smaller than the typical size of 100 kpc of the metal-enriched CGM around high-redshift galaxies (Tumlinson et al. 2017). The sizes and covering fractions of the metal-enriched CGM depend on the galaxy masses and redshifts, where simulations predict that the median separation of an O i absorber at $z = 7$ to its host galaxy is about $250 h^{-1}$ comoving kpc or a physical size of about 45 kpc, and that the absorber may probe either the CGM or the ISM of the host (Doughty & Finlator 2019). Even though the IFU of NIRSpec has a small field of view, there is a non-negligible chance of detecting the associated galaxy through emission lines at the absorber redshift in the IFS data cube, especially if the strongest absorbers probe the ISM. This association of metal absorption lines with galaxies will be investigated in forthcoming papers.

8. Summary and conclusions

We have presented JWST/NIRSpec spectra of four $z > 6.5$ quasars covering the wide spectral range 0.8–5.3 μm . Targeting luminous quasars with magnitudes of $J_{\text{AB}}=17\text{--}20$, the data shows an exquisite signal with a S/N ratio of 50–200 per spectral bin allowing for an in-depth analysis of each of the quasar lines of sight. We detect metal-absorption line systems from intervening absorbers and systems associated with the quasars. In each of the four spectra we identify between 13 and 17 absorption line systems with a total of 61 systems at redshifts ranging from $z = 2.4$ to $z = 7.5$. Since the line of sight towards the quasars probe random locations, the identifications include detections of intervening metal-enriched gas in the CGM or the ISM of intervening galaxies at the highest redshift to date. Most absorption line systems are identified in multiple atomic transitions due to the high quality of the NIRSpec data, while some weaker systems are only detected through Mg II or C IV doublets.

At the quasar redshifts, the Ly α transitions of each absorption system fall in the Gunn-Peterson trough, so deriving hydrogen column densities or metallicities based on the JWST data is impossible, and likewise is it impossible to derive the neutral hydrogen gas fractions. Instead, we use low-ionization lines such as O I as a proxy to examine the changing ionization state of the IGM (Oh 2002). Rather than detecting a forest of metal lines in the IGM at the end of the EoR, we detect instead a number of discrete O I (and Mg II) absorbers, as logically expected since winds from galaxies are responsible for distributing the heavy elements out into the CGM of the host galaxies.

From the number statistics of the low-ionization absorbers O I $\lambda 1302$, C II $\lambda 1334$, Si II $\lambda 1526$, and Mg II $\lambda 2796$, we derive the redshift evolution of the line densities beyond $z > 6$. Combined with other studies of lower redshift quasar spectra (Becker et al. 2019; Chen et al. 2017; Davies et al. 2023a), we find that the line densities of O I, C II, and Si II derived from the NIRSpec data reveal a continued increase beyond $z > 6$, whereas Mg II shows a redshift evolution that is consistent with being constant or mildly decreasing with increasing redshift. In all atomic species, the number of detected absorbers remains small and the redshift path-length interval is also limited in our NIRSpec data set of just four quasars. Consequently, the Poisson uncertainties are large and the line density evolution could also be constant to within $\sim 1\sigma$ uncertainties for all atomic species. Nevertheless, compared to numerical simulations, the observations follow the predicted redshift dependence for the low-ionization lines at $z = 5 \rightarrow 8$, where the model predicts an increase with increasing redshift to $z \sim 7$ due to the increased neutral content and a decreasing UV ionizing background flux. At $z > 7$ the model predicts that line densities decrease with redshift as a consequence of the decreasing metal enrichment of the CGM.

For the high-ionization transitions C IV and Si IV we derive a decrease in line density beyond $z > 6$ following the previously reported rapid decrease seen for these lines from $z = 4 \rightarrow 6$ (D’Odorico et al. 2022; Davies et al. 2023b). Again, the drop is consistent with the model prediction. The transitions in line densities from a predominantly low-ionization level to a high-ionization level occurs at $z \approx 6.0$ for both carbon and silicon. The observations therefore suggest that there is a continuous change in the ionization state rather than a drastic change in the distribution of metals at $z > 6$.

We matched the redshifts of the absorption line systems at $z > 5.7$ with spikes of transmission of Ly α photons in the GP troughs, and find that half of the intervening absorbers that have high-ionization absorption lines fall within $\pm 2000 \text{ km s}^{-1}$

of the Ly α redshift of a matching transmission spike. For low-ionization absorbers on the other hand, only a single system out of 13 intervening absorbers falls within $\pm 2000 \text{ km s}^{-1}$ of a spike. This demonstrates that low-ionization systems are found in environments that are not ionized sufficiently to allow Ly α photons to escape. Low-ionization metal-absorption line systems therefore likely trace higher density environments in the Universe that are among the last ones to become reionized.

While we are not able to derive absolute metallicities, our relative metallicity ratios are accurate provided that the absorption lines are not saturated, and that ionization corrections are insignificant. We argue that the systems traced through O I absorption lines are reliable tracers, since in none of the cases do we detect high-ionization lines and they are not associated with IGM transmission spikes. Focusing on silicon, carbon and oxygen atoms, we derive high values of the metal line ratio [Si/O] in the range from 0.5–1.0 in five of the $z > 6$ absorption systems. Such high values of [Si/O] are consistent with the enrichment pattern expected from energetic Pop III hypernovae with initial stellar masses from 10–15 M_{\odot} , or even from Pop III core-collapse SNe (Heger & Woosley 2010). However, explosions of single Pop II stars with a stellar mass of 15 M_{\odot} can also produce a high [Si/O] ratio (Woosley & Weaver 1995; Kobayashi et al. 2006; Nomoto et al. 2013), so this scenario cannot be ruled out if the absorption system happen to probe a gas cloud enriched by a single star alone. Absorbers with the highest [Si/O] ratios and upper limits on [C/O] could be enriched by Pop III pair instability supernovae. The high [Si/O] ratio and limit on the carbon abundance cannot be explained by the yields produced by Pop II SNe. We therefore suggest that the CGM of the neutral absorption systems at $z > 6$ are dominated by the enrichment from Pop III explosions.

In the near future, surveys from LSST and Euclid will detect an increasing number of (fainter) quasars at $z > 7$. Also with the increasing depth and completed wide-field surveys with JWST, new detections of quasars at $z > 10$ are being made (Goulding et al. 2023; Maiolino et al. 2023). Follow-up near-IR spectroscopic observations with NIRSpec and future ELT spectrographs will allow to extend this work to even higher redshifts into the first half of the reionization epoch beyond $z > 7.5$. Higher resolution spectra compared to the $R \approx 2700$ NIRSpec observations are needed to fit the absorption line profiles with conventional Voigt fitting techniques to verify metal column densities, and with an increasing number of high redshift quasar spectra the larger path length interval will provide line densities with smaller Poisson uncertainties. Future observations of the fields surrounding the four quasars presented in this paper may be able to identify the galaxies responsible for the intervening absorption line systems and single out the galaxies that are possibly responsible for the Pop III metal-enrichment at $z > 6$.

Acknowledgements. We thank Kristian Finlator for useful discussions, and Ezra Huscher for sharing results from their simulations. We also thank Stefania Salvadori for valuable insights into Pop III enrichment. L.C. is supported by DFF/Independent Research Fund Denmark, grant-ID 2032–00071. The Cosmic Dawn Center is funded by the Danish National Research Foundation under grant no. 140. A.J.B. has received funding from the European Research Council (ERC) under the European Union’s Horizon 2020 Advanced Grant 789056 “First Galaxies” MP acknowledges support from the research project PID2021-127718NB-I00 of the Spanish Ministry of Science and Innovation/State Agency of Research (MICIN/AEI), and the Programa Atracción de Talento de la Comunidad de Madrid via grant 2018-T2/TIC-11715. H.Ü. gratefully acknowledges support by the Isaac Newton Trust and by the Kavli Foundation through a Newton-Kavli Junior Fellowship. The work is based on data obtained by the European Southern Observatory, Paranal, Chile, Program IDs: 098.B-0537, 0100.A-0446 and 0100.A-0898. This work is based on observations made with the NASA/ESA/CSA James Webb Space Telescope. The data were obtained from

the Mikulski Archive for Space Telescopes at the Space Telescope Science Institute, which is operated by the Association of Universities for Research in Astronomy, Inc., under NASA contract NAS 5-03127 for JWST. These observations are associated with GTO programs 1219 and 1222.

References

- Andika, I. T., Jahnke, K., Bañados, E., et al. 2022, *AJ*, 163, 251
- Asplund, M., Amarsi, A. M., & Grevesse, N. 2021, *A&A*, 653, A141
- Bañados, E., Rauch, M., Decarli, R., et al. 2019, *ApJ*, 885, 59
- Bañados, E., Schindler, J.-T., Venemans, B. P., et al. 2023, *ApJS*, 265, 29
- Bañados, E., Venemans, B. P., Mazzucchelli, C., et al. 2018, *Nature*, 553, 473
- Bahcall, J. N. & Peebles, P. J. E. 1969, *ApJ*, 156, L7
- Becker, G. D., Bolton, J. S., & Lidz, A. 2015, *PASA*, 32, e045
- Becker, G. D., D’Aloisio, A., Christenson, H. M., et al. 2021, *MNRAS*, 508, 1853
- Becker, G. D., Pettini, M., Rafelski, M., et al. 2019, *ApJ*, 883, 163
- Becker, G. D., Sargent, W. L. W., Rauch, M., & Calverley, A. P. 2011, *ApJ*, 735, 93
- Becker, G. D., Sargent, W. L. W., Rauch, M., & Carswell, R. F. 2012, *ApJ*, 744, 91
- Berg, T. A. M., Ellison, S. L., Sánchez-Ramírez, R., et al. 2016, *MNRAS*, 463, 3021
- Bergeron, J. & Boissé, P. 1991, *A&A*, 243, 344
- Böker, T., Arribas, S., Lützgendorf, N., et al. 2022, *A&A*, 661, A82
- Bosman, S. E. I., Becker, G. D., Haehnelt, M. G., et al. 2017, *MNRAS*, 470, 1919
- Bunker, A. J., Cameron, A. J., Curtis-Lake, E., et al. 2023, *arXiv e-prints*, arXiv:2306.02467
- Chen, S.-F. S., Simcoe, R. A., Torrey, P., et al. 2017, *ApJ*, 850, 188
- Christensen, L., Fynbo, J. P. U., Prochaska, J. X., et al. 2011, *ApJ*, 727, 73
- Christensen, L., Vergani, S. D., Schulze, S., et al. 2017, *A&A*, 608, A84
- Churchill, C. W., Rigby, J. R., Charlton, J. C., & Vogt, S. S. 1999, *ApJS*, 120, 51
- Codoreanu, A., Ryan-Weber, E. V., García, L. Á., et al. 2018, *MNRAS*, 481, 4940
- Cooke, R., Pettini, M., Steidel, C. C., Rudie, G. C., & Nissen, P. E. 2011, *MNRAS*, 417, 1534
- Cooke, R. J., Pettini, M., & Steidel, C. C. 2017, *MNRAS*, 467, 802
- Cooper, T. J., Simcoe, R. A., Cooksey, K. L., et al. 2019, *ApJ*, 882, 77
- Cowie, L. L., Songaila, A., Kim, T.-S., & Hu, E. M. 1995, *AJ*, 109, 1522
- Cupani, G., D’Odorico, V., Cristiani, S., et al. 2022, in *Astronomical Society of the Pacific Conference Series*, Vol. 532, *Astronomical Society of the Pacific Conference Series*, ed. J. E. Ruiz, F. Pierfederici, & P. Teuben, 207
- Curtis-Lake, E., Carniani, S., Cameron, A., et al. 2023, *Nature Astronomy*, 7, 622
- Davies, F. B., Hennawi, J. F., Bañados, E., et al. 2018, *ApJ*, 864, 142
- Davies, F. B., Wang, F., Eilers, A.-C., & Hennawi, J. F. 2020, *ApJ*, 904, L32
- Davies, R. L., Ryan-Weber, E., D’Odorico, V., et al. 2023a, *MNRAS*, 521, 289
- Davies, R. L., Ryan-Weber, E., D’Odorico, V., et al. 2023b, *MNRAS*, 521, 314
- Díaz, C. G., Ryan-Weber, E. V., Karman, W., et al. 2021, *MNRAS*, 502, 2645
- D’Odorico, V., Bañados, E., Becker, G. D., et al. 2023, *MNRAS*, 523, 1399
- D’Odorico, V., Finlator, K., Cristiani, S., et al. 2022, *MNRAS*, 512, 2389
- Doughty, C. & Finlator, K. 2019, *MNRAS*, 489, 2755
- Doughty, C., Finlator, K., Oppenheimer, B. D., Davé, R., & Zackrisson, E. 2018, *MNRAS*, 475, 4717
- Doughty, C. C. & Finlator, K. M. 2023, *MNRAS*, 518, 4159
- Ellison, S. L., Prochaska, J. X., Hennawi, J., et al. 2010, *MNRAS*, 406, 1435
- Ellison, S. L., Songaila, A., Schaye, J., & Pettini, M. 2000, *AJ*, 120, 1175
- Fan, X., Bañados, E., & Simcoe, R. A. 2023, *Annual Review of Astronomy and Astrophysics*, 61, null
- Fan, X., Narayanan, V. K., Lupton, R. H., et al. 2001, *AJ*, 122, 2833
- Fan, X., Wang, F., Yang, J., et al. 2019, *ApJ*, 870, L11
- Fang, H., Xia, L., Ge, J., Willis, K., & Zhao, Y. 2023, *MNRAS*, 518, 5590
- Finlator, K., Doughty, C., Cai, Z., & Díaz, G. 2020, *MNRAS*, 493, 3223
- Finlator, K., Keating, L., Oppenheimer, B. D., Davé, R., & Zackrisson, E. 2018, *MNRAS*, 480, 2628
- Frebel, A. & Norris, J. E. 2015, *ARA&A*, 53, 631
- Gardner, J. P., Mather, J. C., Abbott, R., et al. 2023, *PASP*, 135, 068001
- Gehrels, N. 1986, *ApJ*, 303, 336
- Goulding, A. D., Greene, J. E., Setton, D. J., et al. 2023, *ApJ*, 955, L24
- Gunn, J. E. & Peterson, B. A. 1965, *ApJ*, 142, 1633
- Guo, H., Shen, Y., & Wang, S. 2018, *PyQSOFit: Python code to fit the spectrum of quasars*, *Astrophysics Source Code Library*
- Heckman, T. M., Lehnert, M. D., Strickland, D. K., & Armus, L. 2000, *ApJS*, 129, 493
- Heger, A. & Woosley, S. E. 2002, *ApJ*, 567, 532
- Heger, A. & Woosley, S. E. 2010, *ApJ*, 724, 341
- Hennawi, J. F., Davies, F. B., Wang, F., & Oñorbe, J. 2021, *MNRAS*, 506, 2963
- Inayoshi, K., Visbal, E., & Haiman, Z. 2020, *ARA&A*, 58, 27
- Jakobsen, P., Ferruit, P., Alves de Oliveira, C., et al. 2022, *A&A*, 661, A80
- Jeon, M., Besla, G., & Bromm, V. 2019, *ApJ*, 878, 98
- Jiang, L., Ning, Y., Fan, X., et al. 2022, *Nature Astronomy*, 6, 850
- Kakiichi, K., Ellis, R. S., Laporte, N., et al. 2018, *MNRAS*, 479, 43
- Kashino, D., Lilly, S. J., Matthee, J., et al. 2023, *ApJ*, 950, 66
- Keating, L. C., Puchwein, E., Haehnelt, M. G., Bird, S., & Bolton, J. S. 2016, *MNRAS*, 461, 606
- Kobayashi, C., Umeda, H., Nomoto, K., Tominaga, N., & Ohkubo, T. 2006, *ApJ*, 653, 1145
- Krogager, J.-K. 2018, *arXiv e-prints*, arXiv:1803.01187
- Kulkarni, G., Hennawi, J. F., Rollinde, E., & Vangioni, E. 2014, *ApJ*, 787, 64
- Limongi, M. & Chieffi, A. 2018, *ApJS*, 237, 13
- Ma, Q., Maio, U., Ciardi, B., & Salvaterra, R. 2017, *MNRAS*, 466, 1140
- Maiolino, R., Haehnelt, M., Murphy, M. T., et al. 2013, *arXiv e-prints*, arXiv:1310.3163
- Maiolino, R., Scholtz, J., Curtis-Lake, E., et al. 2023, *arXiv e-prints*, arXiv:2308.01230
- Marshall, M. A., Perna, M., Willott, C. J., et al. 2023, *arXiv e-prints*, arXiv:2302.04795
- Matejek, M. S. & Simcoe, R. A. 2012, *ApJ*, 761, 112
- Matsuoka, Y., Iwasawa, K., Onoue, M., et al. 2022, *ApJS*, 259, 18
- Matsuoka, Y., Iwasawa, K., Onoue, M., et al. 2019a, *ApJ*, 883, 183
- Matsuoka, Y., Onoue, M., Kashikawa, N., et al. 2019b, *ApJ*, 872, L2
- Ménard, B., Wild, V., Nestor, D., et al. 2011, *MNRAS*, 417, 801
- Meyer, R. A., Kakiichi, K., Bosman, S. E. I., et al. 2020, *MNRAS*, 494, 1560
- Miralda-Escudé, J. 1998, *ApJ*, 501, 15
- Mortlock, D. J., Warren, S. J., Venemans, B. P., et al. 2011, *Nature*, 474, 616
- Nomoto, K., Kobayashi, C., & Tominaga, N. 2013, *ARA&A*, 51, 457
- Nomoto, K., Tominaga, N., Umeda, H., Kobayashi, C., & Maeda, K. 2006, *Nucl. Phys. A*, 777, 424
- Oh, S. P. 2002, *MNRAS*, 336, 1021
- Peeples, M. S., Corlies, L., Tumlinson, J., et al. 2019, *ApJ*, 873, 129
- Perna, M., Arribas, S., Marshall, M., et al. 2023, *arXiv e-prints*, arXiv:2304.06756
- Piskunov, N. E., Kupka, F., Ryabchikova, T. A., Weiss, W. W., & Jeffery, C. S. 1995, *A&AS*, 112, 525
- Planck Collaboration, Aghanim, N., Akrami, Y., et al. 2020, *A&A*, 641, A6
- Pons, E., McMahon, R. G., Simcoe, R. A., et al. 2019, *MNRAS*, 484, 5142
- Prochaska, J. X., Gawiser, E., Wolfe, A. M., Cooke, J., & Gelino, D. 2003, *ApJS*, 147, 227
- Prochter, G. E., Prochaska, J. X., & Burles, S. M. 2006, *ApJ*, 639, 766
- Rauscher, B. J., Arendt, R. G., Fixsen, D. J., et al. 2017, *PASP*, 129, 105003
- Reed, S. L., Banerji, M., Becker, G. D., et al. 2019, *MNRAS*, 487, 1874
- Rigby, J., Perrin, M., McElwain, M., et al. 2023, *PASP*, 135, 048001
- Ryabchikova, T., Piskunov, N., Kurucz, R. L., et al. 2015, *Phys. Scr*, 90, 054005
- Saccardi, A., Salvadori, S., D’Odorico, V., et al. 2023, *ApJ*, 948, 35
- Salvadori, S., D’Odorico, V., Saccardi, A., Skúladóttir, Á., & Vanni, I. 2023, *arXiv e-prints*, arXiv:2305.07706
- Simcoe, R. A., Onoue, M., Eilers, A.-C., et al. 2020, *arXiv e-prints*, arXiv:2011.10582
- Smith, J. D. T., Armus, L., Dale, D. A., et al. 2007, *PASP*, 119, 1133
- Spitzer, L. 1978, *Physical processes in the interstellar medium* (John Wiley & Sons)
- Thielemann, F.-K., Nomoto, K., & Hashimoto, M.-A. 1996, *ApJ*, 460, 408
- Tie, S. S., Hennawi, J. F., Wang, F., et al. 2023, *arXiv e-prints*, arXiv:2308.11888
- Tumlinson, J., Peeples, M. S., & Werk, J. K. 2017, *ARA&A*, 55, 389
- Vanni, I., Salvadori, S., & Skúladóttir, Á. 2023a, *arXiv e-prints*, arXiv:2305.02358
- Vanni, I., Salvadori, S., Skúladóttir, Á., Rossi, M., & Koutsouridou, I. 2023b, *MNRAS*, 526, 2620
- Venemans, B. P., Walter, F., Decarli, R., et al. 2017, *ApJ*, 851, L8
- Wang, F., Yang, J., Fan, X., et al. 2021, *ApJ*, 907, L1
- Wang, F., Yang, J., Fan, X., et al. 2019, *ApJ*, 884, 30
- Wang, F., Yang, J., Fan, X., et al. 2018, *ApJ*, 869, L9
- Welsh, L., Cooke, R., & Fumagalli, M. 2019, *MNRAS*, 487, 3363
- Welsh, L., Cooke, R., Fumagalli, M., & Pettini, M. 2023, *MNRAS*, 525, 527
- Wild, V., Hewett, P. C., & Pettini, M. 2006, *MNRAS*, 367, 211
- Willott, C. J., Delorme, P., Reyly, C., et al. 2010, *AJ*, 139, 906
- Woosley, S. E. & Weaver, T. A. 1995, *ApJS*, 101, 181
- Yang, J., Venemans, B., Wang, F., et al. 2019, *ApJ*, 880, 153
- Yang, J., Wang, F., Fan, X., et al. 2021, *ApJ*, 923, 262
- Yang, J., Wang, F., Fan, X., et al. 2020, *ApJ*, 904, 26
- Zou, S., Jiang, L., Shen, Y., et al. 2021, *ApJ*, 906, 32

Appendix A: Normalised spectra and absorption line systems

For visualisation purposes the normalized Fixed Slit spectra of the quasars are shown here, with all the different intervening and proximate absorption line systems overlaid. Absorption lines are color coded to mark lines belonging to the same redshift absorbers. Figures with zoom in on individually detected absorption lines for each system are presented in Appendix B. Note that the Ly α forest is ignored, and we do not include the Band III data from 3-5.3 μm , because only a very few absorption lines are detected at these wavelengths.

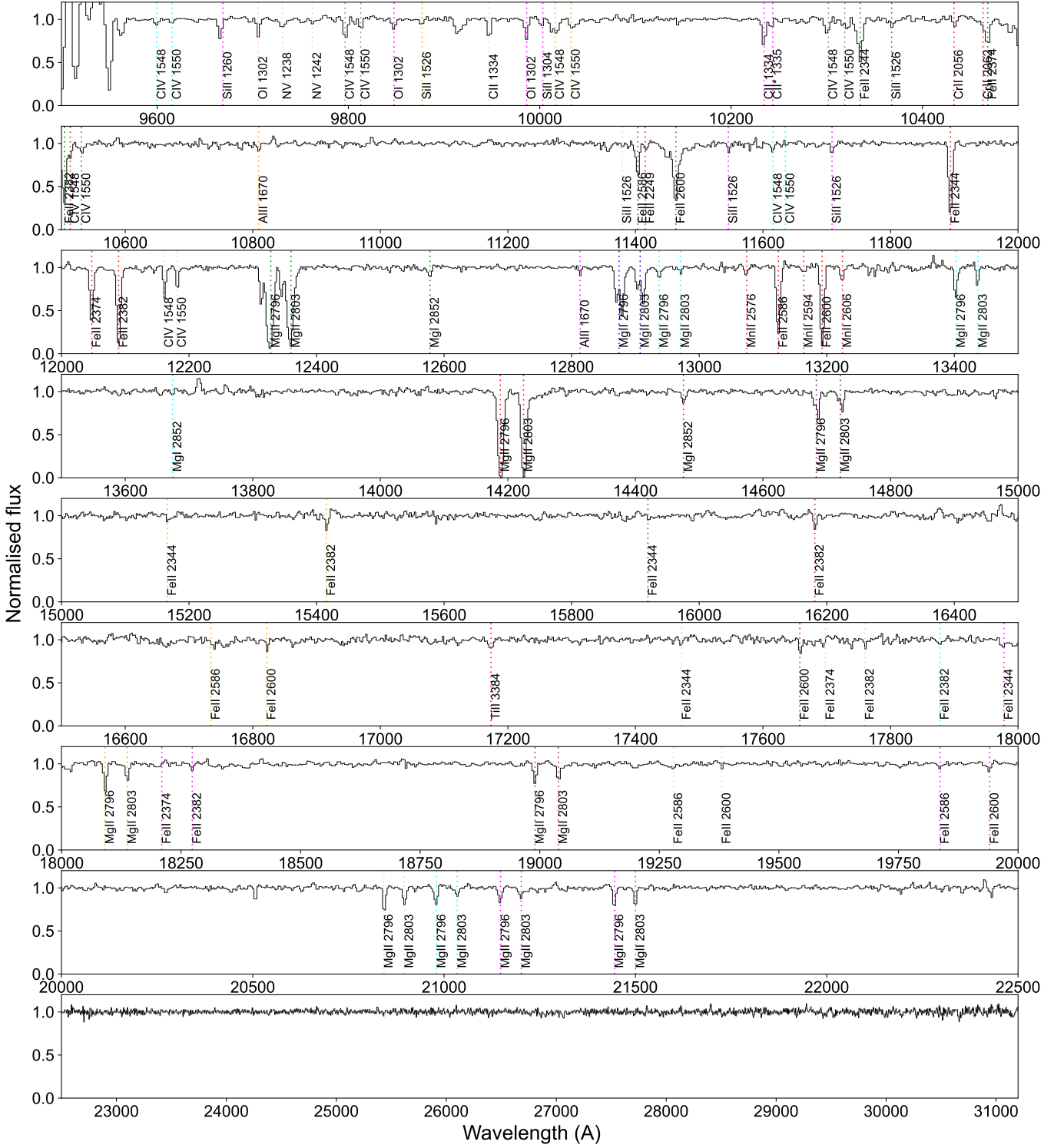


Fig. A.1. Normalized spectrum of VDES J0020-3653. Absorption line systems are identified via multiple absorption lines at the same redshifts. Here, 16 different absorption systems are detected at $z = 3.4087, 3.6040, 3.6265, 3.7930, 4.0738, 4.2510, 5.2005, 5.3277, 5.4695, 5.6540, 5.7910, 6.4535, 6.5028, 6.5625, 6.669,$ and 6.855 . Each absorption system is specified with a distinct colour. The absorber at the highest redshift lies at the quasar redshift.

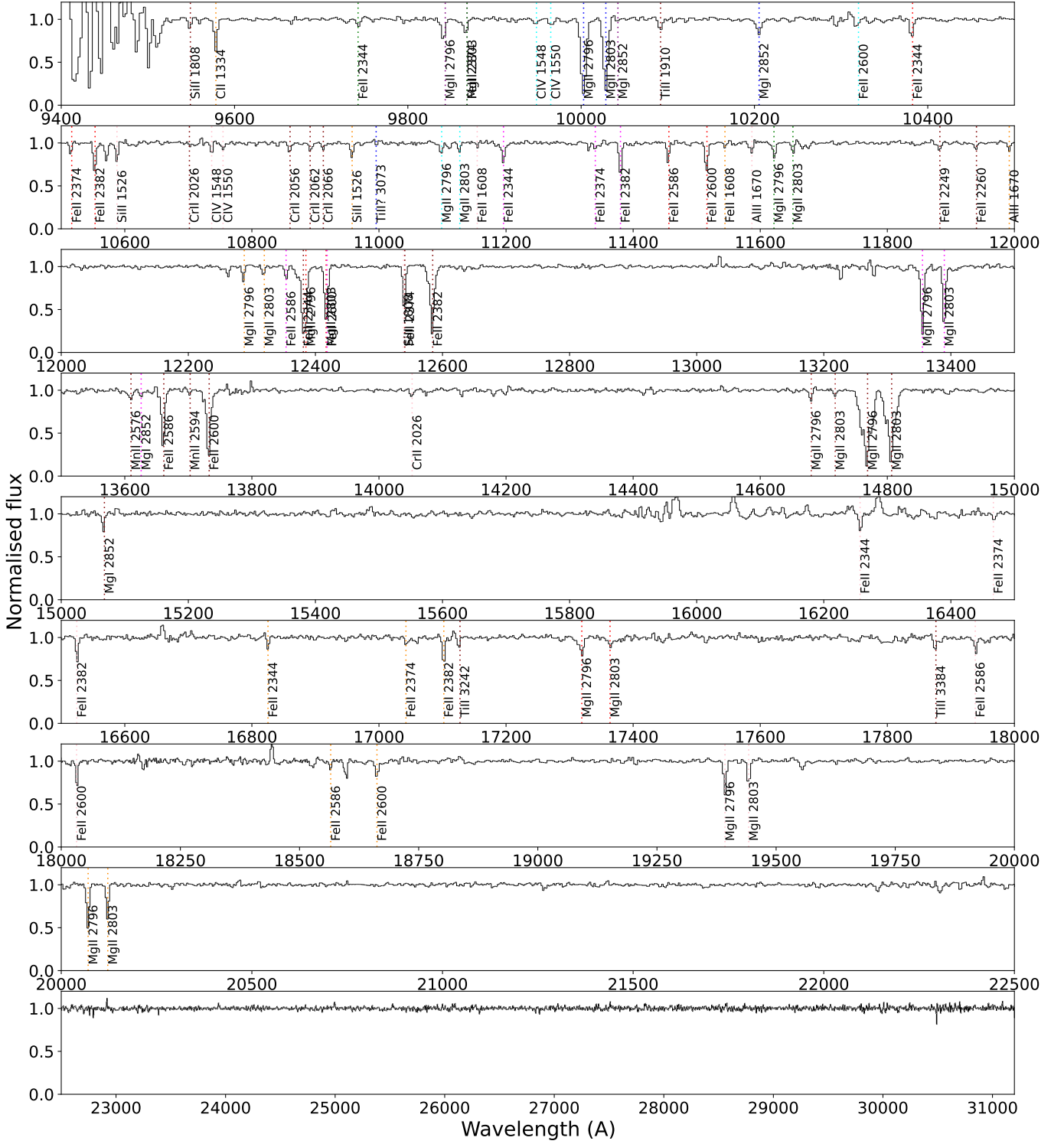


Fig. A.2. Normalized spectrum of DELS J0411-0907. Absorption line systems are identified via multiple absorption lines at the same redshifts. Here, 13 different absorption systems are detected at $z = 2.52, 2.5771, 2.969, 3.156, 3.3943, 3.4290, 3.7760, 4.2498, 4.2815, 5.1935, 5.4258, 5.935,$ and 6.1774 .

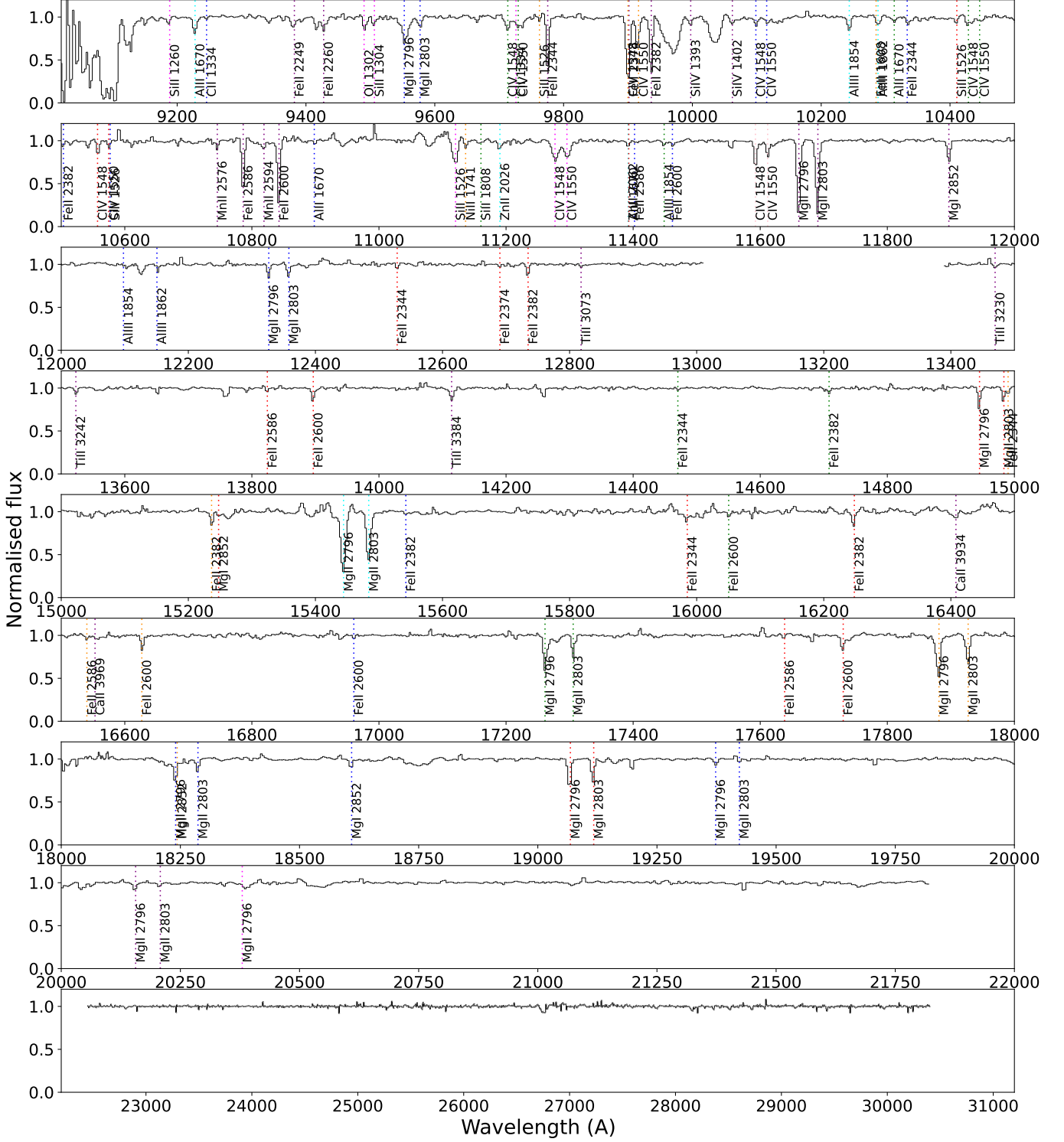


Fig. A.3. Full spectrum of UHS J0439+1634. The normalization of the quasar continuum emission is not accurate around 10,000–11,000 Å, where the quasar spectrum has strong BAL features. Absorption line systems are identified via multiple absorption lines at the same redshifts. Here, 17 different absorption systems are detected at $z = 2.4161, 3.170, 3.4081, 4.3445, 4.523, 5.1728, 5.274, 5.3945, 5.5228, 5.736, 5.819, 5.928, 6.028, 6.173, 6.284, 6.288,$ and 6.4877 . The highest redshift absorber is at the quasar redshift.

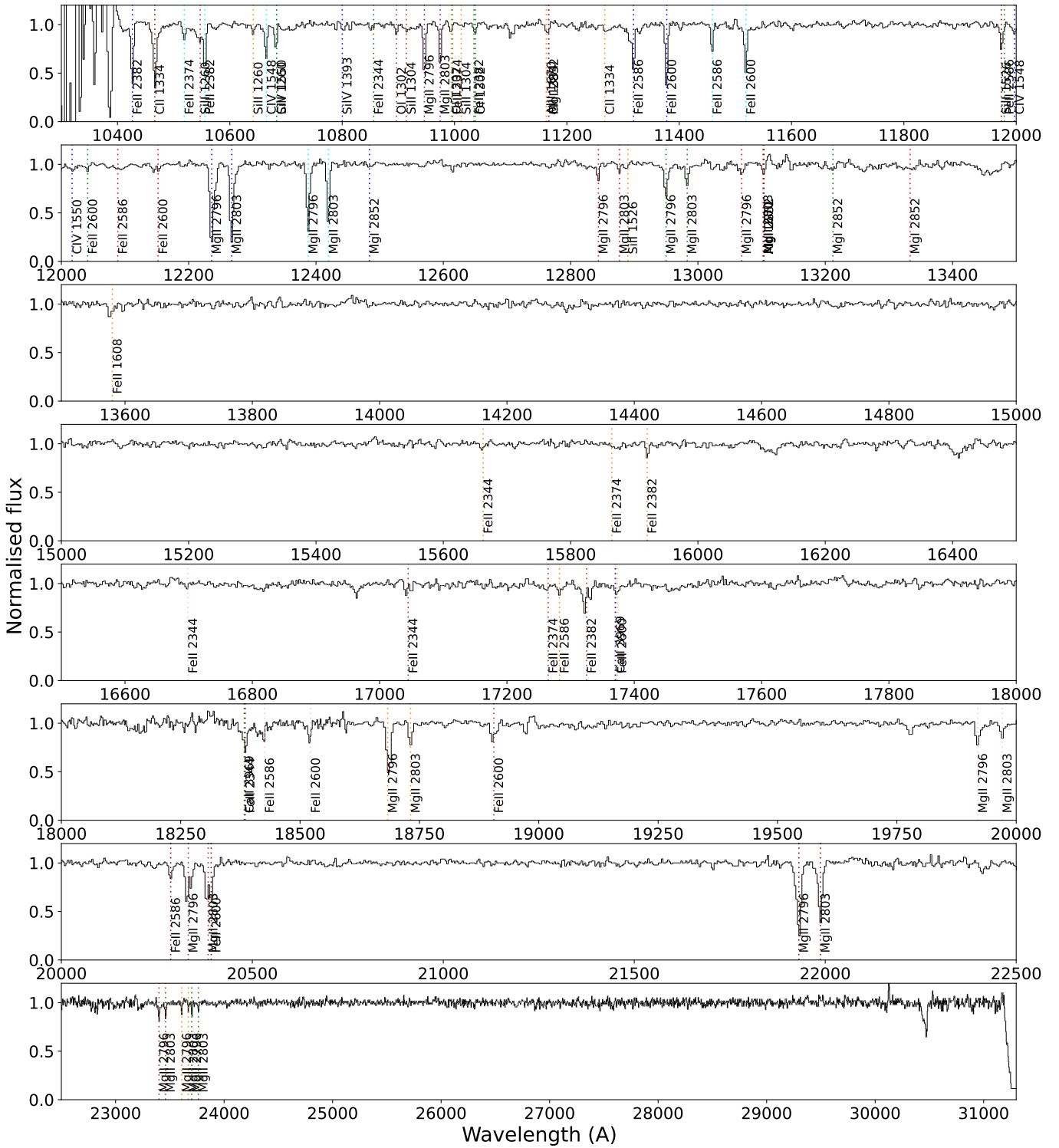


Fig. A.4. Full spectrum of ULAS J1342+0928. Absorption line systems are identified via multiple absorption lines at the same redshifts. Here, 15 different absorption systems are detected at $z = 2.9145, 3.3758, 3.430, 3.593, 3.631, 3.6735, 5.6814, 5.8888, 6.1234, 6.271, 6.749, 6.8427, 7.368, 7.443, \text{ and } 7.476$. The highest redshift absorber is associated with the quasar, being offset by $\approx 2000 \text{ km s}^{-1}$ from the quasar systemic redshift.

Appendix B: Individual absorption systems

The appendix presents each of the detected absorption line systems. In each of the quasar spectra we have identified between 13–17 intervening absorption line systems at different redshifts, ranging from lower redshifts ($z = 2.4$) to absorbers located at the quasar redshifts.

In the figures in this appendix all panels illustrate the normalised quasar spectrum around the detected absorption line species within $\pm 600 \text{ km s}^{-1}$ for each of the absorption systems. Flux errors per spectral pixel are overlaid, and the y-axis of each absorption line is scaled to match the depth of the line. Equivalent widths in the observed frame are computed by integrating the lines from within $\pm 200 \text{ km s}^{-1}$, while for the stronger systems that display broader lines, the lines are integrated within $\pm 300 \text{ km s}^{-1}$. The reported wavelengths of the absorption lines in all tables are computed from weighted mean flux values rather than based on absorption line fits. Line profiles for narrow line systems for a single absorption system may appear visually different as explained in Fig. 6 in Section 2. Some lines are blended or partially contaminated with other identified lines from other absorption systems. We describe in the comments to the tables which lines are blended with a line from another system. Some weak lines or lines towards longer wavelengths are dominated by errors from the complex normalization of the quasar spectrum.

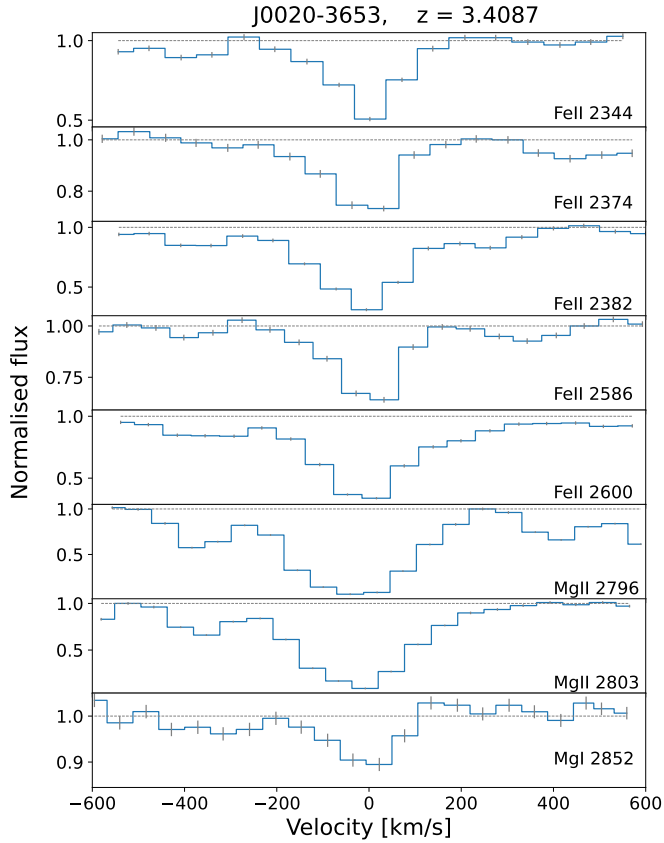


Fig. B.1. Absorption system at $z = 3.4087$ toward J0020–3653. Note that the y-axis range changes according to the strengths of the absorption lines in this and all other panels.

Table B.1. J0020–3653 $z = 3.4087$

λ_{obs}	ID	W_{obs}
10334.94	Fe II 2344.21	2.821 ± 0.119
10468.29	Fe II 2374.46	$1.916 \pm 0.098^{\dagger}$
10504.90	Fe II 2382.76	$6.216 \pm 0.104^{\ddagger}$
11403.76	Fe II 2586.65	2.574 ± 0.104
11463.38	Fe II 2600.17	7.266 ± 0.095
12328.28	Mg II 2796.35	12.011 ± 0.081
12359.93	Mg II 2803.53	11.204 ± 0.081
12577.86	Mg I 2852.96	0.700 ± 0.107

[†] Line blended with Cr II $\lambda 2062$ at $z = 4.0738$

[‡] Line partly blended with C IV $\lambda 1548$ at $z = 5.791$

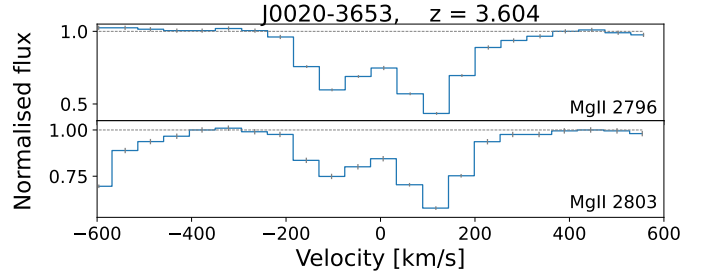


Fig. B.2. Absorption system at $z = 3.604$ toward J0020–3653.

Table B.2. J0020–3653 $z = 3.604$

λ_{obs}	ID	W_{obs}
12874.40	Mg II 2796.35	6.396 ± 0.095
12907.46	Mg II 2803.53	4.372 ± 0.105

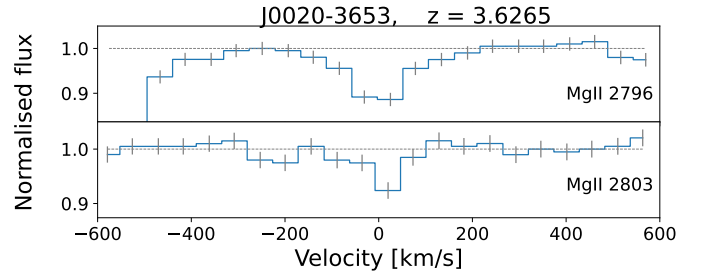


Fig. B.3. Absorption system at $z = 3.6265$ toward J0020–3653.

Table B.3. J0020–3653 $z = 3.6265$

λ_{obs}	ID	W_{obs}
12937.32	Mg II 2796.35	0.872 ± 0.098
12970.54	Mg II 2803.53	0.320 ± 0.102

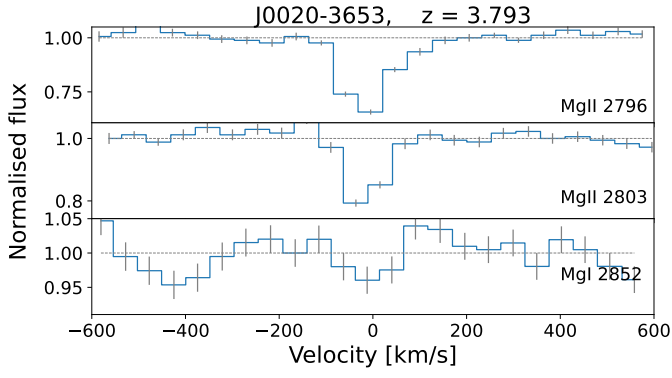
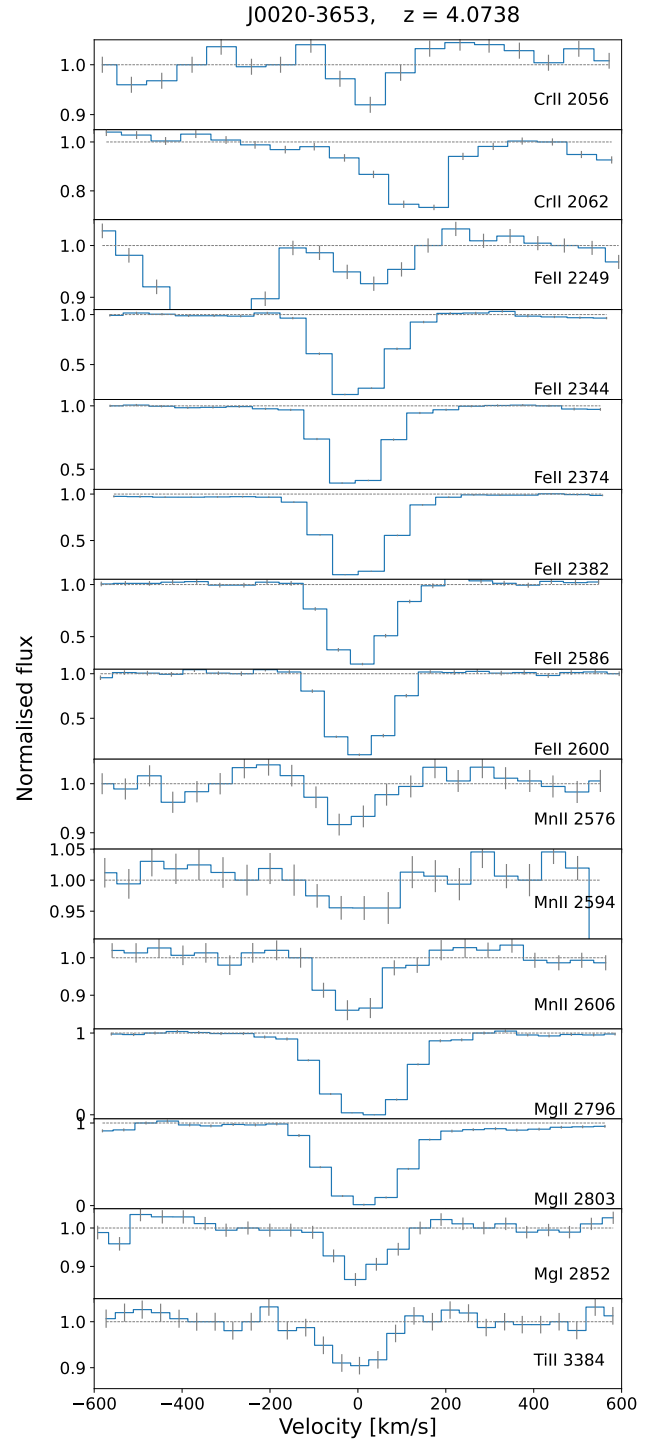

Fig. B.4. Absorption system at $z = 3.793$ toward J0020–3653.

Table B.4. J0020–3653 $z = 3.793$

λ_{obs}	ID	W_{obs}
13402.92	Mg II 2796.35	1.977 ± 0.070
13437.32	Mg II 2803.53	0.770 ± 0.089
13674.26	Mg I 2852.96	0.190 ± 0.125

Table B.5. J0020–3653 $z = 4.0738$

λ_{obs}	ID	W_{obs}
10433.02	Cr II 2056.25	0.128 ± 0.093
10463.36	Cr II 2062.23	$1.813 \pm 0.085^{\dagger}$
11415.42	Fe II 2249.88	0.614 ± 0.093
11894.07	Fe II 2344.21	5.535 ± 0.073
12047.54	Fe II 2374.46	4.390 ± 0.053
12089.67	Fe II 2382.76	6.750 ± 0.052
13124.14	Fe II 2586.65	5.113 ± 0.140
13192.76	Fe II 2600.17	6.237 ± 0.135
13074.56	Mn II 2576.88	0.265 ± 0.157
13163.97	Mn II 2594.50	0.289 ± 0.156
13224.65	Mn II 2606.46	0.866 ± 0.163
14188.13	Mg II 2796.35	10.553 ± 0.095
14224.56	Mg II 2803.53	10.212 ± 0.097
14475.37	Mg I 2852.96	0.842 ± 0.118
17173.49	Ti II 3384.74	0.718 ± 0.150

[†] Line blended with Fe II $\lambda 2374$ at $z = 3.4087$

Fig. B.5. Absorption system at $z = 4.0738$ toward J0020–3653.

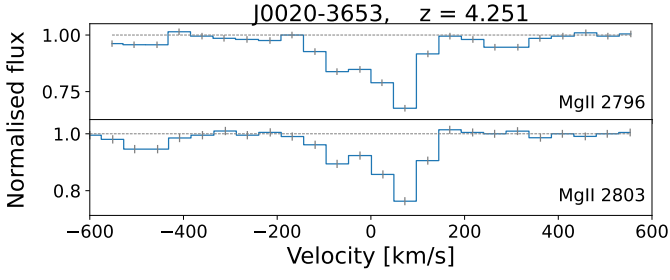


Fig. B.6. Absorption system at $z = 4.251$ toward J0020–3653.

Table B.6. J0020–3653 $z = 4.251$

λ_{obs}	ID	W_{obs}
14683.64	Mg II 2796.35	2.392 ± 0.098
14721.34	Mg II 2803.53	1.630 ± 0.096

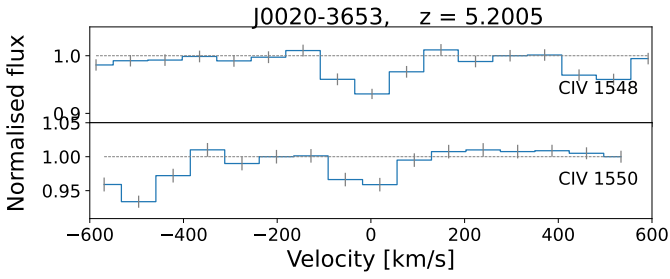


Fig. B.7. Absorption system at $z = 5.2005$ toward J0020–3653.

Table B.7. J0020–3653 $z = 5.2005$

λ_{obs}	ID	W_{obs}
9599.58	C IV 1548.19	0.274 ± 0.052
9615.55	C IV 1550.77	0.168 ± 0.053

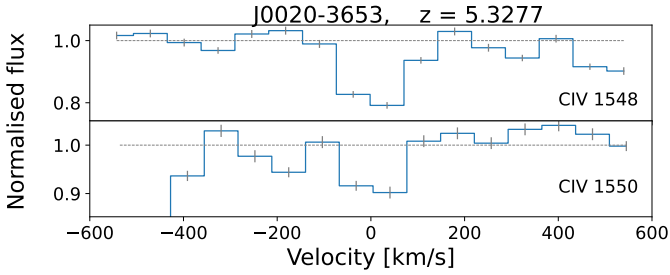


Fig. B.8. Absorption system at $z = 5.3277$ toward J0020–3653.

Table B.8. J0020–3653 $z = 5.3277$

λ_{obs}	ID	W_{obs}
9796.51	C IV 1548.19	1.075 ± 0.053
9812.81	C IV 1550.77	0.396 ± 0.056

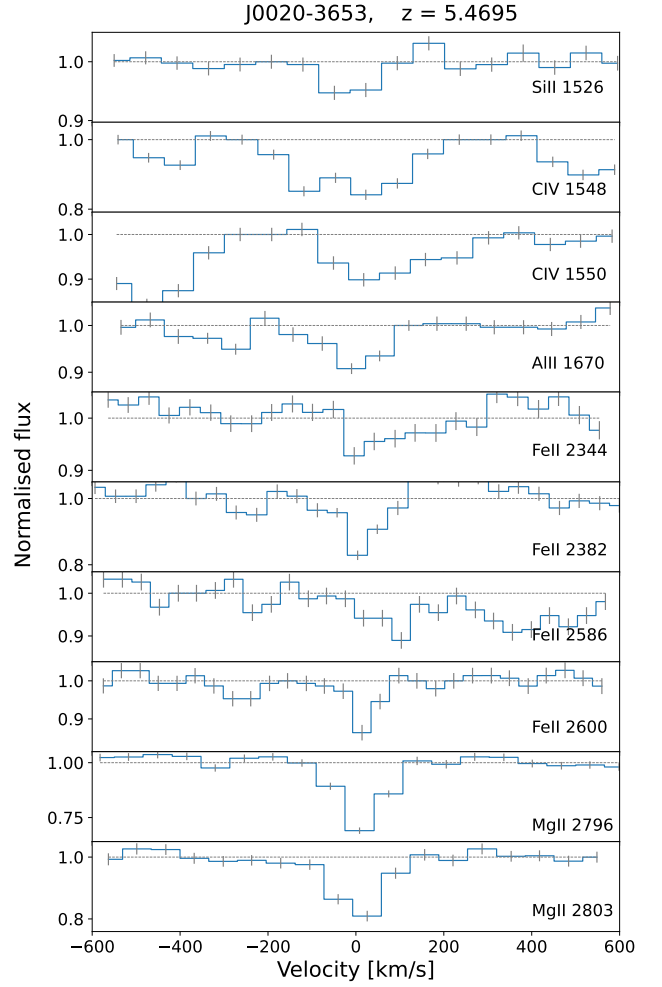


Fig. B.9. Absorption system at $z = 5.4695$ toward J0020–3653.

Table B.9. J0020–3653 $z = 5.4695$

λ_{obs}	ID	W_{obs}
9877.03	Si II 1526.71	0.181 ± 0.069
10016.05	C IV 1548.19	1.477 ± 0.084
10032.71	C IV 1550.77	0.697 ± 0.087
10809.16	Al II 1670.79	0.499 ± 0.079
15165.89	Fe II 2344.21	0.342 ± 0.118
15415.30	Fe II 2382.76	0.469 ± 0.136
16734.33	Fe II 2586.65	0.774 ± 0.145
16821.82	Fe II 2600.17	0.588 ± 0.152
18091.00	Mg II 2796.35	2.264 ± 0.135
18137.44	Mg II 2803.53	1.734 ± 0.164

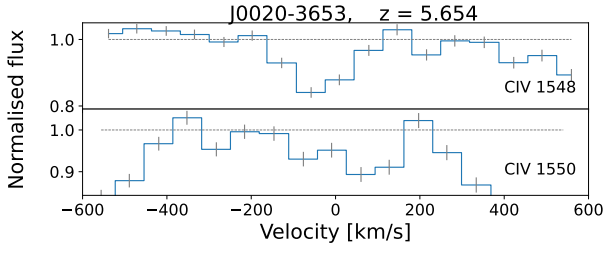

Fig. B.10. Absorption system at $z = 5.654$ toward J0020–3653.

Table B.10. J0020–3653 $z = 5.654$

λ_{obs}	ID	W_{obs}
10301.69	C IV 1548.19	0.805 ± 0.093
10318.82	C IV 1550.77	0.706 ± 0.102

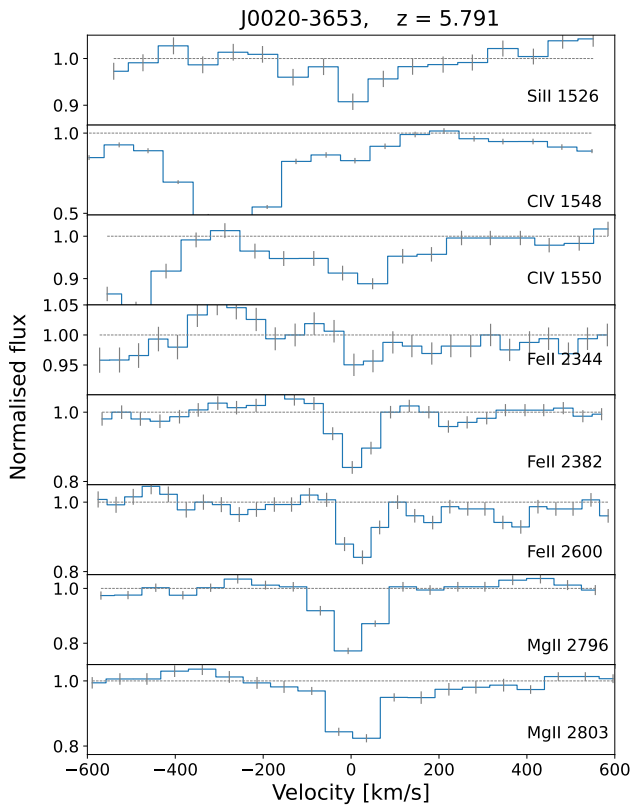

Fig. B.11. Absorption system at $z = 5.791$ toward J0020–3653.

Table B.11. J0020–3653 $z = 5.791$

λ_{obs}	ID	W_{obs}
10367.86	Si II 1526.71	0.501 ± 0.093
10513.79	C IV 1548.19	$2.426 \pm 0.095^{\dagger}$
10531.28	C IV 1550.77	0.936 ± 0.097
15919.56	Fe II 2344.21	0.317 ± 0.132
16181.36	Fe II 2382.76	0.405 ± 0.131
17657.77	Fe II 2600.17	1.029 ± 0.149
18990.03	Mg II 2796.35	1.684 ± 0.168
19038.78	Mg II 2803.53	1.926 ± 0.145

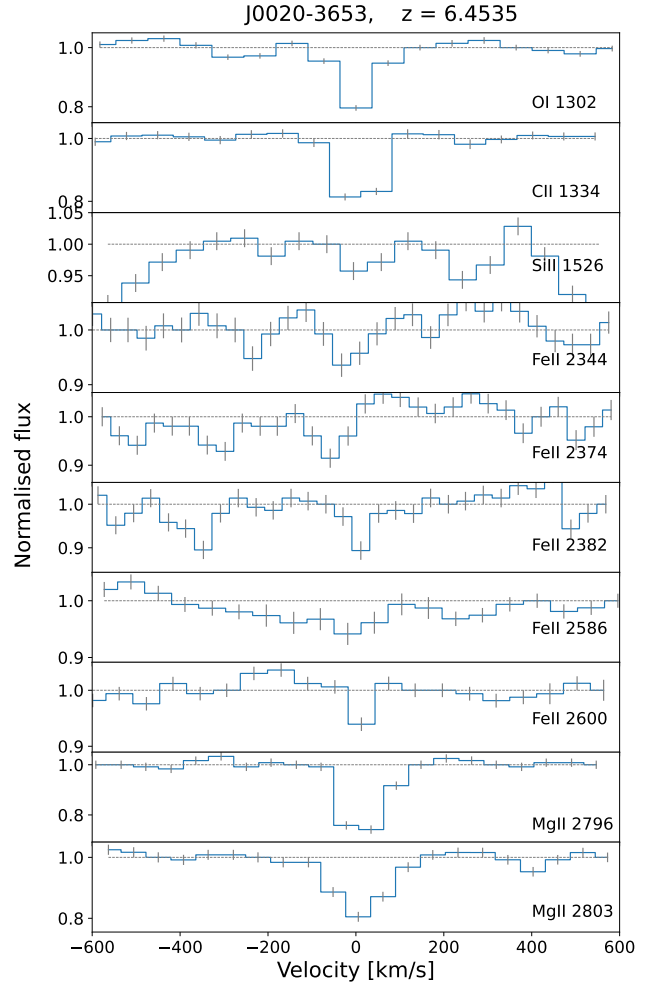
[†] Line partly blended with Fe II λ 2382 at $z = 3.4087$

Fig. B.12. Absorption system at $z = 6.4535$ toward J0020–3653.

Table B.12. J0020–3653, $z = 6.4535$

λ_{obs}	ID	W_{obs}
9705.71	O I 1302.17	0.680 ± 0.050
9946.94	C II 1334.53	0.768 ± 0.077
11379.31	Si II 1526.71	0.212 ± 0.089
17472.60	Fe II 2344.21	0.083 ± 0.159
17698.05	Fe II 2374.46	0.094 ± 0.148
17759.94	Fe II 2382.76	0.406 ± 0.159
19279.60	Fe II 2586.65	0.741 ± 0.187
19380.39	Fe II 2600.17	0.139 ± 0.094
20842.61	Mg II 2796.35	2.301 ± 0.175
20896.12	Mg II 2803.53	1.956 ± 0.170

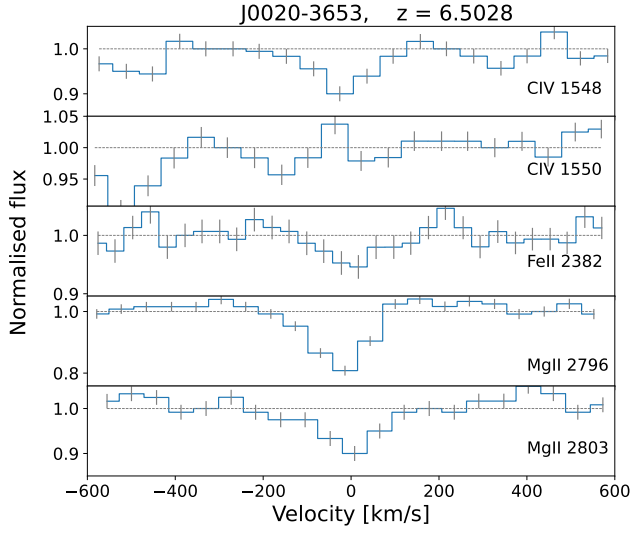


Fig. B.13. Absorption system at $z = 6.5028$ toward J0020–3653.

Table B.13. J0020–3653, $z = 6.5028$

λ_{obs}	ID	W_{obs}
11615.80	C IV 1548.19	0.524 ± 0.096
11635.12	C IV 1550.77	0.114 ± 0.092
17877.41	Fe II 2382.76	0.383 ± 0.150
20980.47	Mg II 2796.35	1.642 ± 0.167
21034.33	Mg II 2803.53	1.086 ± 0.175

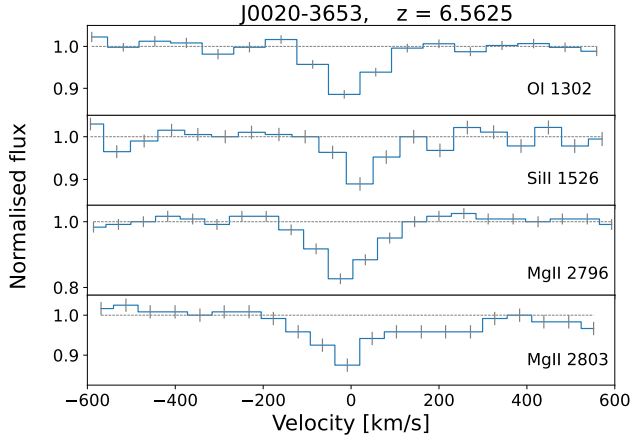
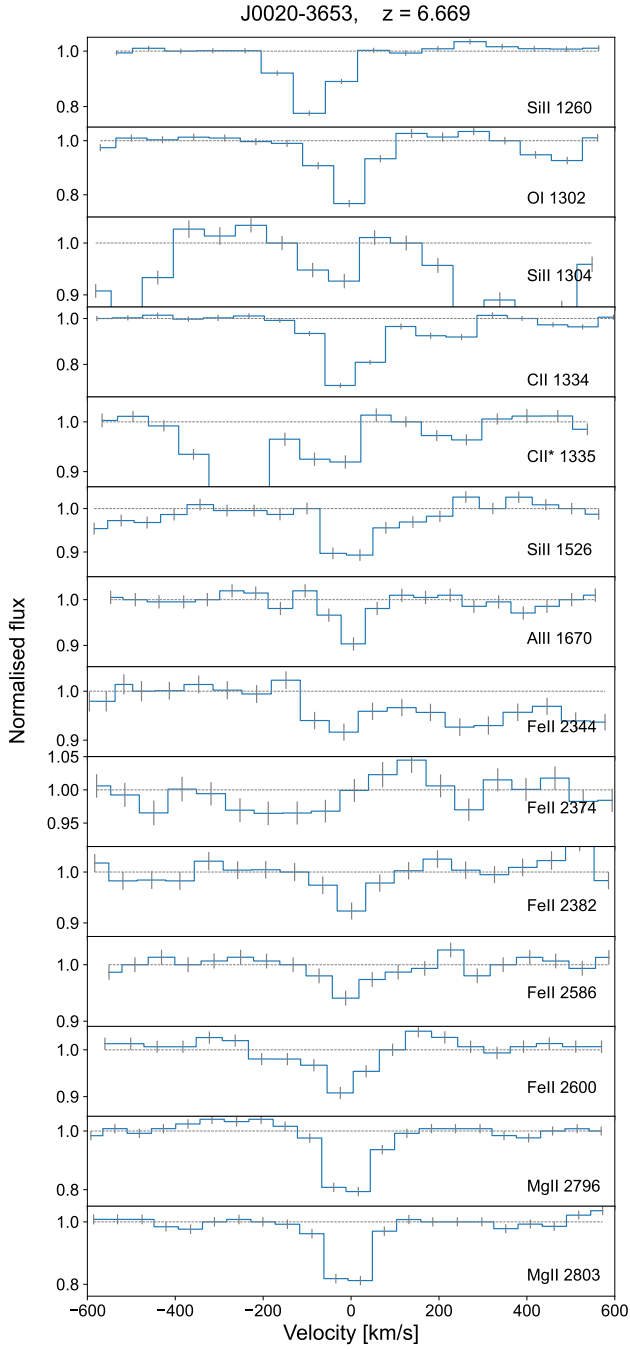


Fig. B.14. Absorption system at $z = 6.5625$ toward J0020–3653.

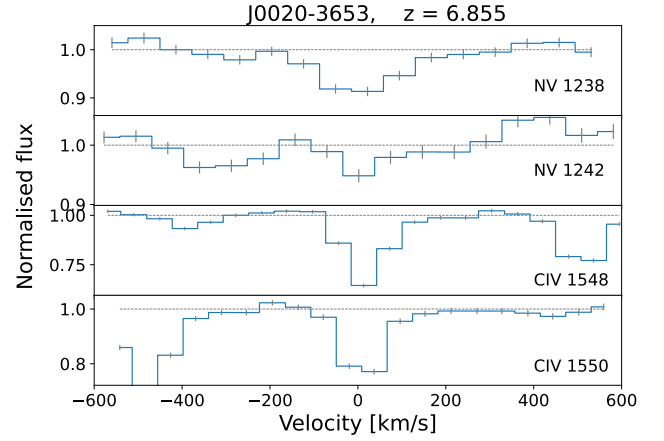
Table B.14. J0020–3653, $z = 6.5625$

λ_{obs}	ID	W_{obs}
9847.65	O I 1302.17	0.472 ± 0.059
11545.72	Si II 1526.71	0.445 ± 0.091
10092.39	C II 1334.53	$< 0.4^\dagger$
21147.41	Mg II 2796.35	1.633 ± 0.185
21201.70	Mg II 2803.53	1.553 ± 0.175

[†]C II is not clearly detected in this system. A 3σ upper limit is listed because the limit is used in Section 5.

**Fig. B.15.** Absorption system at $z = 6.669$ toward J0020-3653**Table B.15.** J0020-3653, $z = 6.669$

λ_{obs}	ID	W_{obs}
9668.71	Si II 1260.75	0.964 ± 0.055
9986.33	O I 1302.17	0.884 ± 0.074
10003.22	Si II 1304.37	0.368 ± 0.081
10234.53	C II 1334.53	1.292 ± 0.078
10243.54	C II* 1335.71	0.447 ± 0.073
11708.31	Si II 1526.71	0.707 ± 0.078
12813.27	Al II 1670.79	0.318 ± 0.090
17977.78 [†]	Fe II 2344.21	0.947 ± 0.171
18209.74	Fe II 2374.46	0.139 ± 0.175
18273.42	Fe II 2382.76	0.362 ± 0.180
19837.02	Fe II 2586.65	0.469 ± 0.137
19940.73	Fe II 2600.17	0.595 ± 0.128
21445.22	Mg II 2796.35	1.857 ± 0.167
21500.28	Mg II 2803.53	1.729 ± 0.157

[†] Line blended with unidentified feature.**Fig. B.16.** Absorption system at $z = 6.855$ toward J0020-3653**Table B.16.** J0020-3653, $z = 6.855$

λ_{obs}	ID	W_{obs}
9730.94	N v 1238.82	0.638 ± 0.056
9762.23	N v 1242.80	0.202 ± 0.058
12161.07	C IV 1548.19	1.582 ± 0.058
12181.30	C IV 1550.77	1.176 ± 0.063

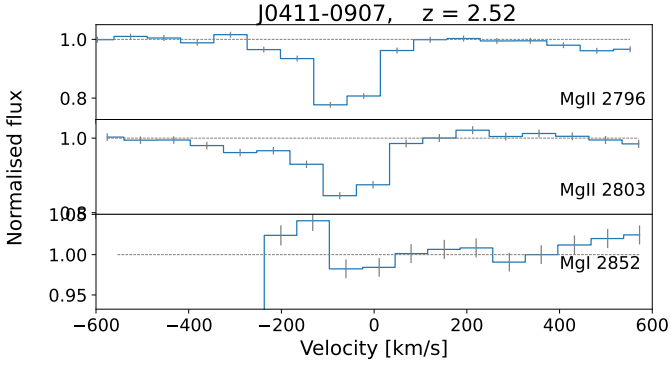


Fig. B.17. Absorption system at $z = 2.52$ toward J0411–0907. Note that the y-axis range changes according to the strengths of the absorption lines in this and all other panels.

Table B.17. J0411–0907, $z = 2.52$

λ_{obs}	ID	W_{obs}
9843.16	Mg II 2796.35	1.315 ± 0.067
9868.43 [†]	Mg II 2803.53	0.967 ± 0.072
10042.43	Mg I 2852.96	0.216 ± 0.084

[†] Line blended with Fe II $\lambda 2374$ at $z = 3.156$

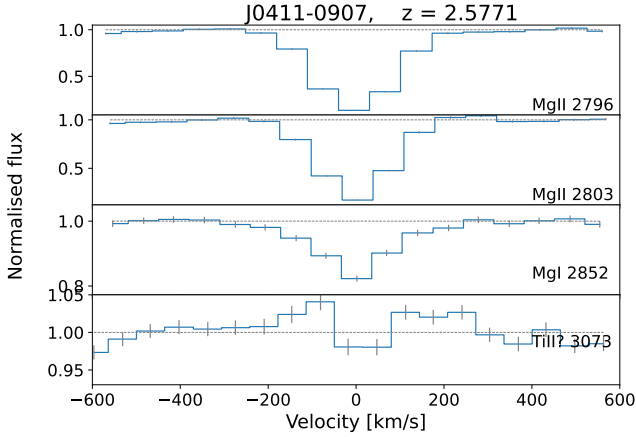


Fig. B.18. Absorption system at $z = 2.5771$ toward J0411–0907.

Table B.18. J0411–0907, $z = 2.5771$

λ_{obs}	ID	W_{obs}
10002.83	Mg II 2796.35	6.342 ± 0.068
10028.51	Mg II 2803.53	5.164 ± 0.075
10205.34	Mg I 2852.96	1.218 ± 0.068
10995.57	Ti II 3073.88	1.340 ± 0.068

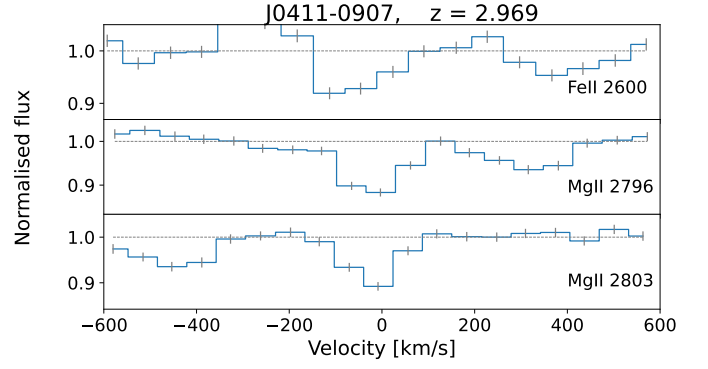


Fig. B.19. Absorption system at $z = 2.969$ toward J0411–0907.

Table B.19. J0411–0907, $z = 2.969$

λ_{obs}	ID	W_{obs}
10320.09	Fe II 2600.17	0.370 ± 0.067
11098.72	Mg II 2796.35	0.804 ± 0.061
11127.21	Mg II 2803.53	0.459 ± 0.062

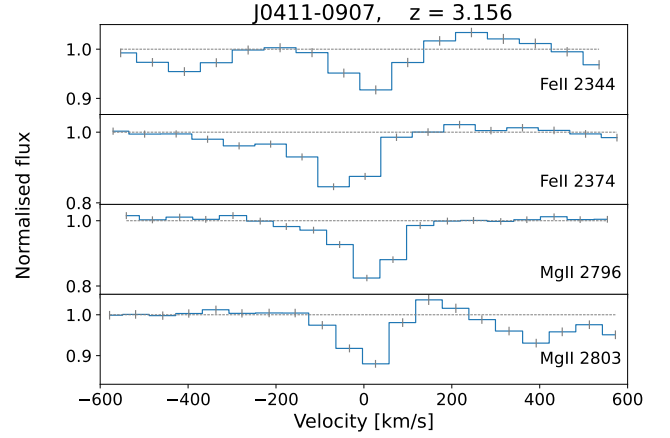


Fig. B.20. Absorption system at $z = 3.1560$ toward J0411–0907.

Table B.20. J0411–0907, $z = 3.1560$.

λ_{obs}	ID	W_{obs}
9742.55	Fe II 2344.21	0.344 ± 0.054
9868.26	Fe II 2374.46	$0.857 \pm 0.053^{\dagger}$
11621.64	Mg II 2796.35	1.012 ± 0.065
11651.47	Mg II 2803.53	0.485 ± 0.061

[†] Line blended with Mg II $\lambda 2803$ at $z = 2.520$

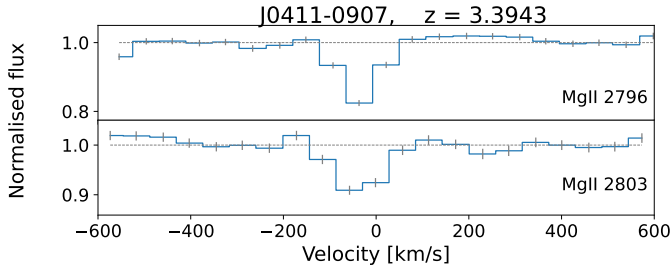

Fig. B.21. Absorption system at $z = 3.3943$ toward J0411–0907.

Table B.21. J0411–0907, $z = 3.3943$

λ_{obs}	ID	W_{obs}
12288.01	Mg II 2796.35	0.596 ± 0.057
12319.56	Mg II 2803.53	0.412 ± 0.059

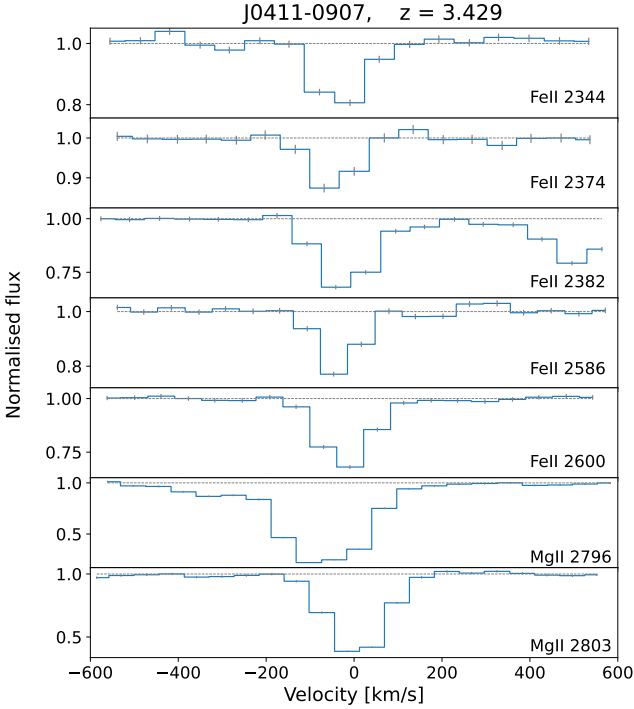

Fig. B.22. Absorption system at $z = 3.429$ toward J0411–0907.

Table B.22. J0411–0907, $z = 3.429$

λ_{obs}	ID	W_{obs}
10382.52	Fe II 2344.21	$0.930 \pm 0.066^{\dagger}$
10516.49	Fe II 2374.46	0.518 ± 0.060
10553.27	Fe II 2382.76	1.827 ± 0.063
11456.27	Fe II 2586.65	1.013 ± 0.057
11516.17	Fe II 2600.17	1.764 ± 0.060
12385.04	Mg II 2796.35	7.222 ± 0.048
12416.84	Mg II 2803.53	$4.273 \pm 0.068^{\ddagger}$

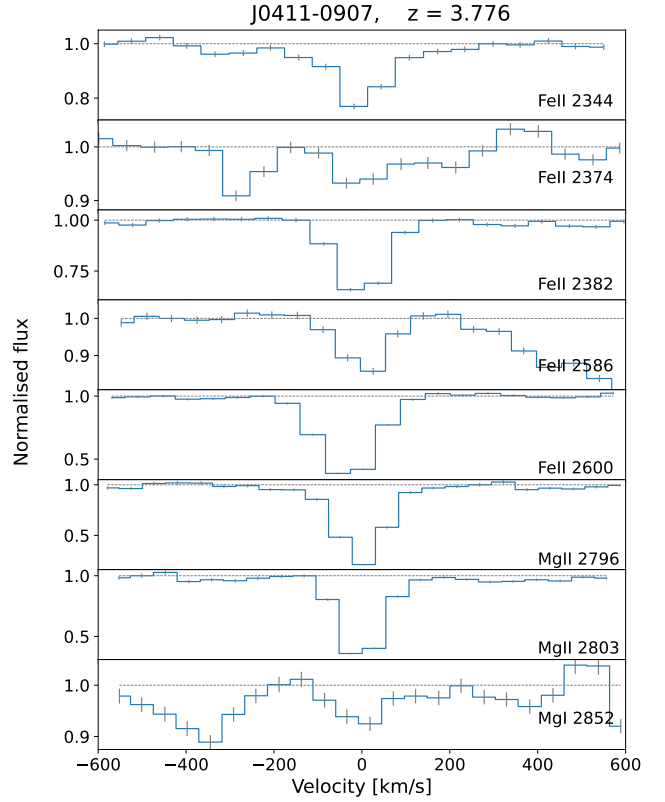
 † Line blended with Mg II $\lambda 2796$ at $z = 4.2814$
 ‡ Line blended with Fe II $\lambda 2600$ at $z = 3.776$

Fig. B.23. Absorption system at $z = 3.776$ toward J0411–0907.

Table B.23. J0411–0907, $z = 3.776$

λ_{obs}	ID	W_{obs}
11195.97	Fe II 2344.21	1.418 ± 0.061
11340.43	Fe II 2374.46	0.475 ± 0.062
11380.09	Fe II 2382.76	1.948 ± 0.053
12353.84	Fe II 2586.65	0.694 ± 0.060
12418.43	Fe II 2600.17	$4.225 \pm 0.054^{\dagger}$
13355.38	Mg II 2796.35	4.777 ± 0.079
13389.66	Mg II 2803.53	3.952 ± 0.072
13625.76	Mg I 2852.96	0.532 ± 0.095

 † Line blended with Mg II $\lambda 2803$ at $z = 3.429$

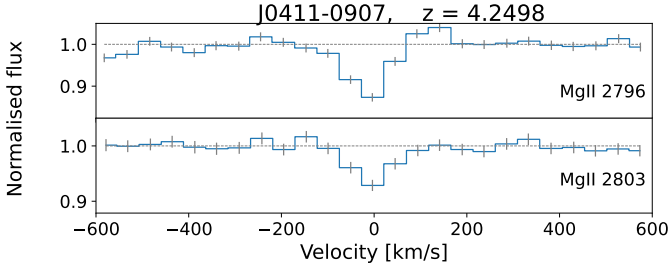


Fig. B.24. Absorption system at $z = 4.2498$ toward J0411-0907.

Table B.24. J0411-0907, $z = 4.2498$

λ_{obs}	ID	W_{obs}
14680.29	Mg II 2796.35	0.493 ± 0.075
14717.98	Mg II 2803.53	0.359 ± 0.074

Table B.25. J0411-0907, $z = 4.2815$

λ_{obs}	ID	W_{obs}
9549.02	Si II 1808.01	0.261 ± 0.053
10091.63	Ti II 1910.75	0.543 ± 0.083
10701.74	Cr II 2026.27	0.365 ± 0.086
10860.10	Cr II 2056.25	0.590 ± 0.068
10891.69	Cr II 2062.23	0.598 ± 0.067
10912.43	Cr II 2066.16	0.465 ± 0.069
11882.72	Fe II 2249.88	0.453 ± 0.070
11940.31	Fe II 2260.78	0.445 ± 0.065
12380.97	Fe II 2344.21	$8.400 \pm 0.065^{\dagger}$
12540.72	Fe II 2374.46	$2.378 \pm 0.072^{\ddagger}$
12584.57	Fe II 2382.76	6.032 ± 0.063
13661.39	Fe II 2586.65	3.979 ± 0.117
13732.81	Fe II 2600.17	6.267 ± 0.105
13702.85	Mn II 2594.50	0.139 ± 0.118
13609.78	Mn II 2576.88	0.983 ± 0.113
14768.93	Mg II 2796.35	13.433 ± 0.066
14806.85	Mg II 2803.53	10.878 ± 0.073
15067.93	Mg I 2852.96	0.875 ± 0.094
17127.53	Ti II 3242.93	0.210 ± 0.131
17876.50	Ti II 3384.74	0.818 ± 0.136

† Line blended with Mg II $\lambda 2796$ at $z = 3.429$

‡ Line blended with Si II $\lambda 1808$ at $z = 5.935$

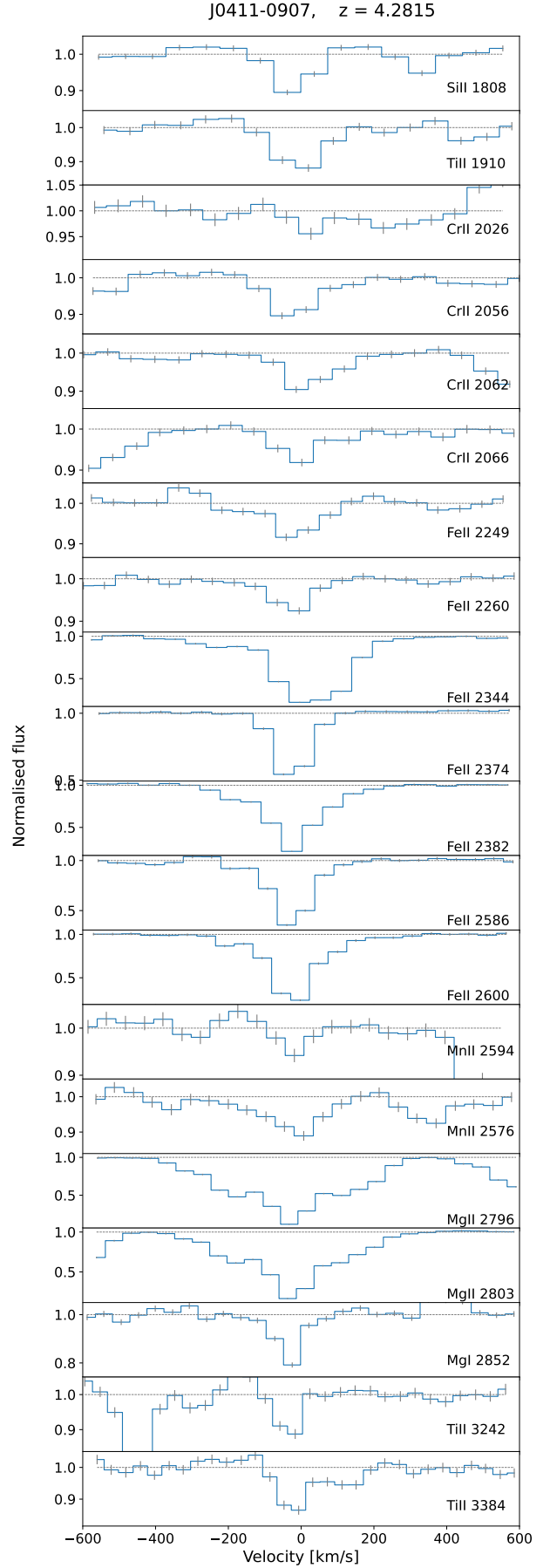


Fig. B.25. Absorption system at $z = 4.2815$ toward J0411-0907.

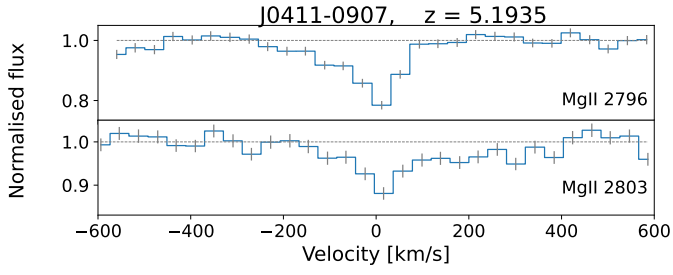

Fig. B.26. Absorption system at $z = 5.1935$ toward J0411-0907.

Table B.26. J0411-0907, $z = 5.1935$

λ_{obs}	ID	W_{obs}
17319.21	Mg II 2796.35	1.740 ± 0.108
17363.67	Mg II 2803.53	1.107 ± 0.112

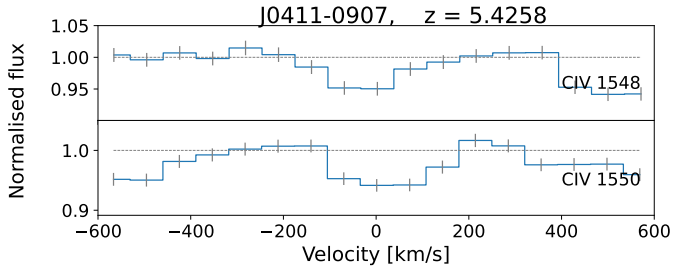
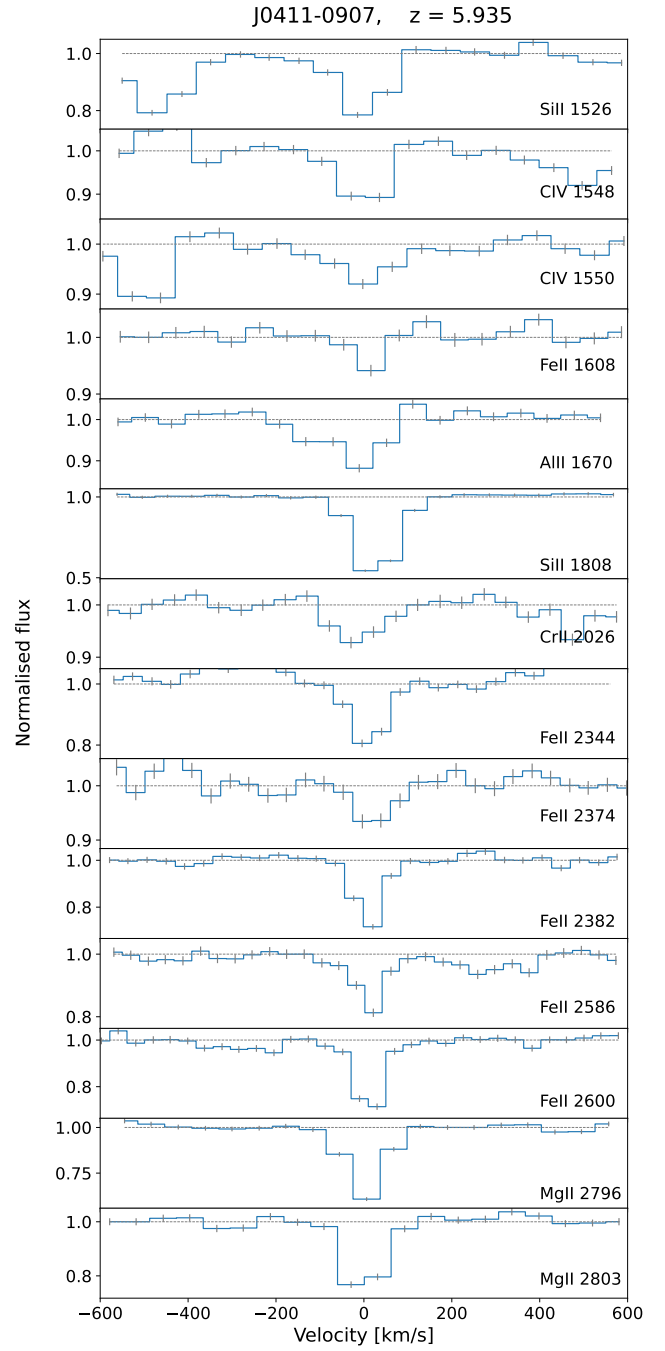

Fig. B.27. Absorption system at $z = 5.4258$ toward J0411-0907.

Table B.27. J0411-0907, $z = 5.4258$

λ_{obs}	ID	W_{obs}
9948.39	C IV 1548.19	0.329 ± 0.057
9964.94	C IV 1550.77	0.434 ± 0.056

Table B.28. J0411-0907, $z = 5.935$

λ_{obs}	ID	W_{obs}
10587.71	Si II 1526.71	0.990 ± 0.068
10736.73	C IV 1548.19	0.464 ± 0.061
10754.59	C IV 1550.77	0.491 ± 0.065
11154.61	Fe II 1608.45	$0.084 \pm 0.061^{\dagger}$
11586.91	Al II 1670.79	0.606 ± 0.066
12538.57	Si II 1808.01	$2.485 \pm 0.056^{\ddagger}$
14052.18	Cr II 2026.27	0.361 ± 0.075
16257.12	Fe II 2344.21	0.974 ± 0.090
16466.89	Fe II 2374.46	0.370 ± 0.096
16524.48	Fe II 2382.76	1.182 ± 0.097
17938.42	Fe II 2586.65	1.068 ± 0.108
18032.20	Fe II 2600.17	1.655 ± 0.107
19392.70	Mg II 2796.35	2.620 ± 0.130
19442.49	Mg II 2803.53	1.823 ± 0.123

[†] Line blended with Mg II $\lambda 2803$ at $z = 2.9791$
[‡] Line blended with Fe II $\lambda 2374$ at $z = 4.2815$

Fig. B.28. Absorption system at $z = 5.935$ toward J0411-0907.

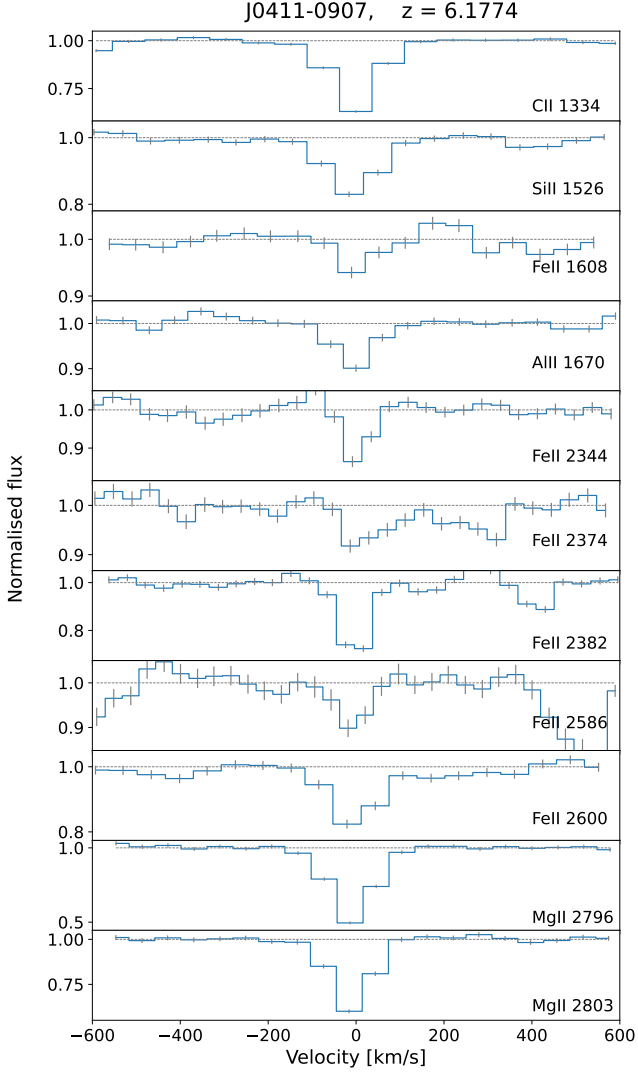


Fig. B.29. Absorption system at $z = 6.1774$ toward J0411–0907.

Table B.29. J0411–0907, $z = 6.1774$

λ_{obs}	ID	W_{obs}
9578.47	C II 1334.53	1.541 ± 0.040
10957.78	Si II 1526.71	0.912 ± 0.057
11544.50	Fe II 1608.45	0.135 ± 0.066
11991.91	Al II 1670.79	0.416 ± 0.053
16825.36	Fe II 2344.21	0.256 ± 0.116
17042.46	Fe II 2374.46	0.670 ± 0.102
17102.06	Fe II 2382.76	1.538 ± 0.111
18565.42	Fe II 2586.65	0.558 ± 0.174
18662.48	Fe II 2600.17	1.655 ± 0.133
20070.54	Mg II 2796.35	4.041 ± 0.128
20122.06	Mg II 2803.53	3.008 ± 0.132

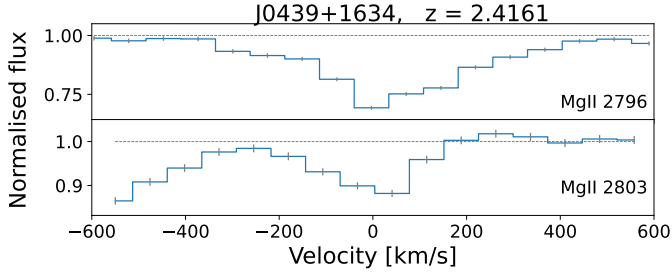


Fig. B.30. Absorption system at $z = 2.4161$ toward J0439+1634.

Table B.30. J0439+1634, $z = 2.4161$

λ_{obs}	ID	W_{obs}
9552.62	Mg II 2796.35	3.401 ± 0.061
9577.14	Mg II 2803.53	0.843 ± 0.058

Table B.31. J0439+1634, $z = 3.170$

λ_{obs}	ID	W_{obs}
9381.99	Fe II 2249.88	1.041 ± 0.044
9427.45	Fe II 2260.78	1.163 ± 0.044
9775.37	Fe II 2344.21	3.118 ± 0.042
9901.50	Fe II 2374.46	$5.010 \pm 0.035^{\ddagger}$
9936.13	Fe II 2382.76	3.662 ± 0.045
10786.33	Fe II 2586.65	2.915 ± 0.042
10842.72	Fe II 2600.17	4.057 ± 0.054
10819.06	Mn II 2594.50	0.764 ± 0.060
10745.58	Mn II 2576.88	0.489 ± 0.041
11660.79	Mg II 2796.35	5.468 ± 0.029
11690.72	Mg II 2803.53	5.410 ± 0.031
11896.86	Mg I 2852.96	1.438 ± 0.042
12818.07	Ti II 3073.88	0.175 ± 0.052
13469.65	Ti II 3230.13	0.020 ± 0.040
13523.01	Ti II 3242.93	0.334 ± 0.038
14114.37	Ti II 3384.74	1.089 ± 0.036
16407.99	Ca II 3934.77	0.721 ± 0.124

‡ Line blended with C IV $\lambda 1548$ at $z = 5.3945$

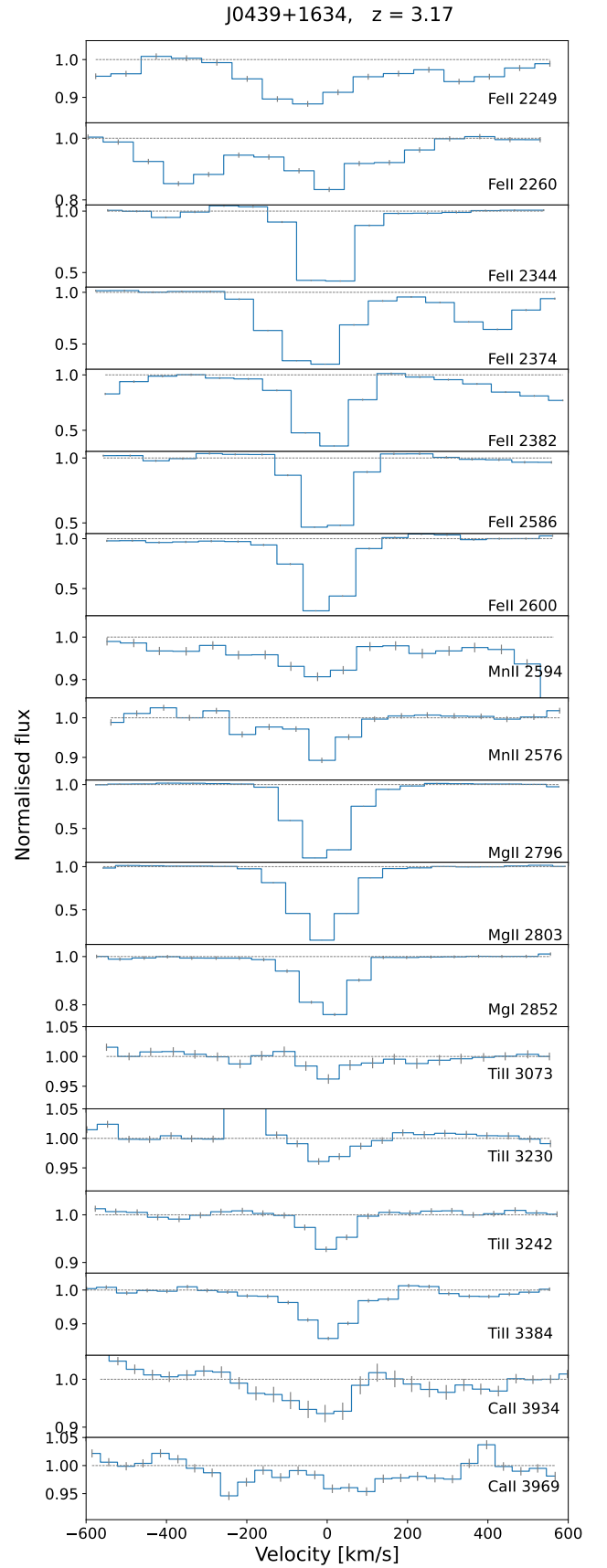


Fig. B.31. Absorption system at $z = 3.170$ toward J0439+1634.

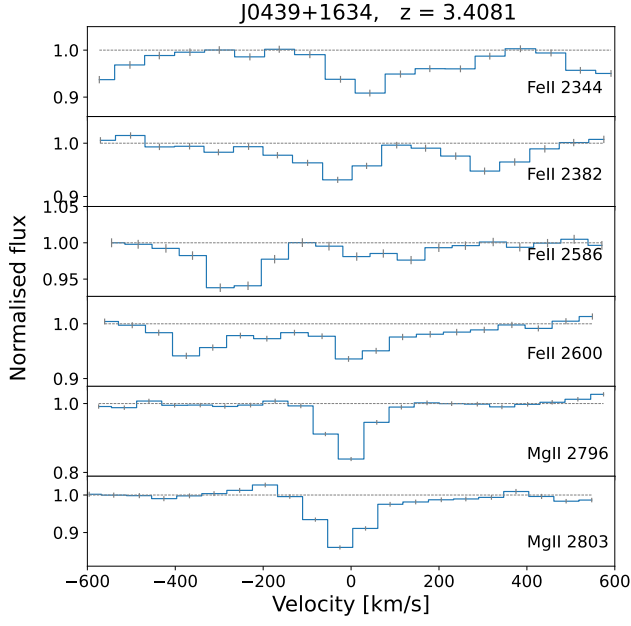


Fig. B.32. Absorption system at $z = 3.4081$ toward J0439+1634.

Table B.32. J0439+1634, $z = 3.4081$

λ_{obs}	ID	W_{obs}
10333.53	Fe II 2344.21	0.593 ± 0.043
10503.47	Fe II 2382.76	0.434 ± 0.035
11402.21	Fe II 2586.65	0.217 ± 0.036
11461.82	Fe II 2600.17	0.526 ± 0.034
12326.60	Mg II 2796.35	0.743 ± 0.042
12358.25	Mg II 2803.53	0.743 ± 0.037

Table B.33. J0439+1634, $z = 4.3445$

λ_{obs}	ID	W_{obs}
12528.65	Fe II 2344.21	0.154 ± 0.031
12690.30	Fe II 2374.46	0.138 ± 0.030
12734.69	Fe II 2382.76	0.595 ± 0.034
13824.35	Fe II 2586.65	0.098 ± 0.035
13896.62	Fe II 2600.17	0.874 ± 0.032
14945.10	Mg II 2796.35	1.052 ± 0.037
14983.47	Mg II 2803.53	0.756 ± 0.043
15247.67	Mg I 2852.96	0.558 ± 0.038

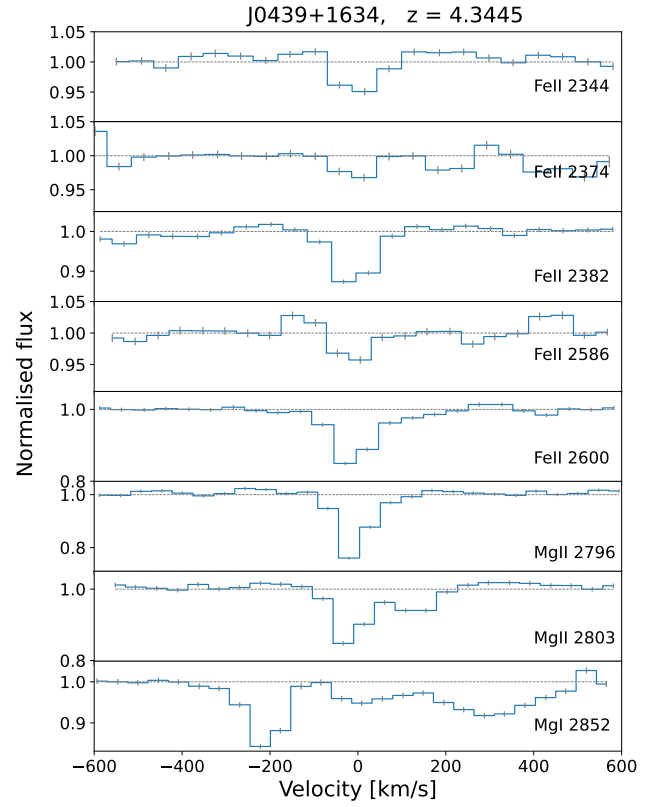


Fig. B.33. Absorption system at $z = 4.3445$ toward J0439+1634.

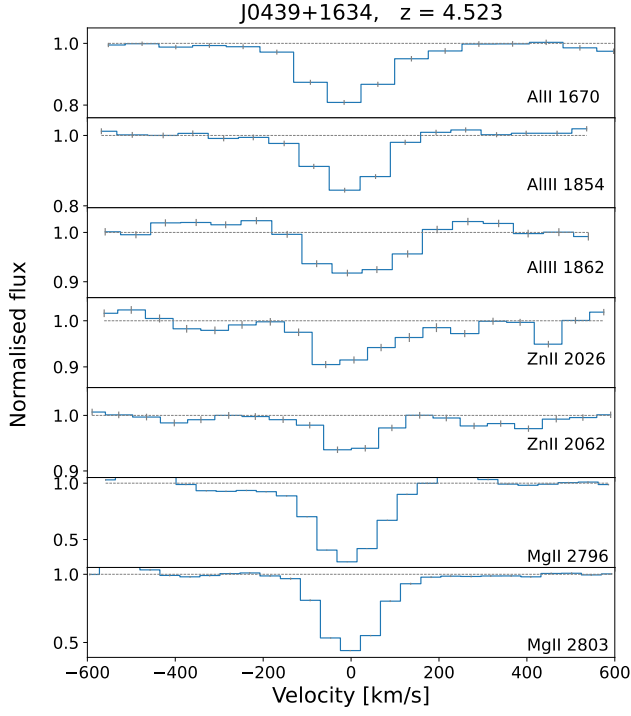


Fig. B.34. Absorption system at $z = 4.523$ toward J0439+1634.

Table B.34. J0439+1634, $z = 4.523$

λ_{obs}	ID	W_{obs}
9227.76	Al II 1670.79	1.304 ± 0.049
10243.60	Al III 1854.72	0.946 ± 0.046
10288.19	Al III 1862.79	$0.561 \pm 0.044^{\dagger}$
11190.35	Zn II 2026.14	0.745 ± 0.053
11392.07	Zn II 2062.66	$0.414 \pm 0.040^{\ddagger}$
15444.25	Mg II 2796.35	6.397 ± 0.042
15483.90	Mg II 2803.53	4.731 ± 0.047

[†] Line blended with Fe II $\lambda 1608$ at $z = 5.3945$

[‡] Line blended with Al II $\lambda 1670$ at $z = 5.8190$

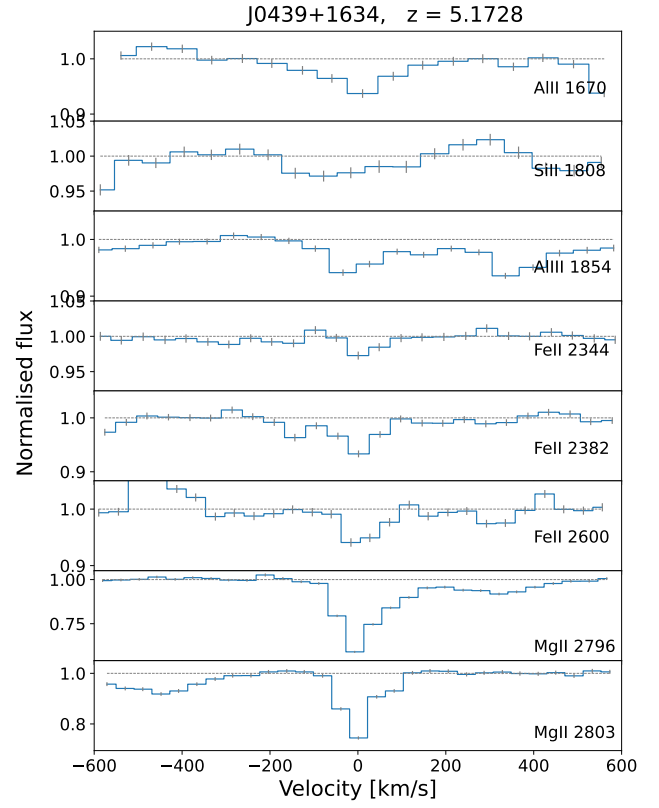


Fig. B.35. Absorption system at $z = 5.1728$ toward J0439+1634.

Table B.35. J0439+1634, $z = 5.1728$

λ_{obs}	ID	W_{obs}
10313.43	Al II 1670.79	0.404 ± 0.046
11160.50	Si II 1808.01	0.245 ± 0.047
11448.79	Al III 1854.72	0.399 ± 0.032
14470.36	Fe II 2344.21	0.139 ± 0.040
14708.33	Fe II 2382.76	0.502 ± 0.046
16050.35	Fe II 2600.17	0.382 ± 0.053
17261.32	Mg II 2796.35	2.945 ± 0.054
17305.64	Mg II 2803.53	1.278 ± 0.051

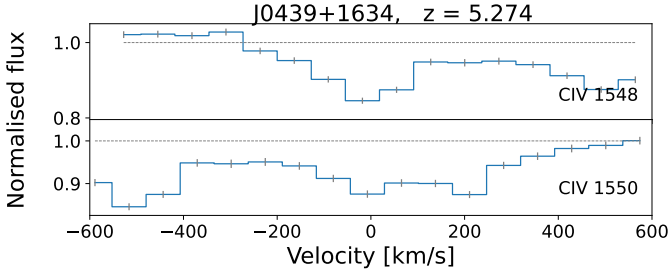


Fig. B.36. Absorption system at $z = 5.274$ toward J0439+1634.

Table B.36. J0439+1634, $z = 5.274$

λ_{obs}	ID	W_{obs}
9713.38	C IV 1548.19	1.124 ± 0.045
9729.53	C IV 1550.77	$1.107 \pm 0.046^{\dagger}$

† Line blended with C II $\lambda 11334$ at $z = 6.288$

Table B.37. J0439+1634, $z = 5.3945$

λ_{obs}	ID	W_{obs}
9762.53	Si II 1526.71	0.062 ± 0.050
9899.93	C IV 1548.19	$5.166 \pm 0.040^{\dagger}$
9916.40	C IV 1550.77	2.331 ± 0.053
10285.24	Fe II 1608.45	$0.437 \pm 0.041^{\ddagger}$
11136.36	Ni II 1741.55	0.251 ± 0.052
14990.08	Fe II 2344.21	0.378 ± 0.032
15236.59	Fe II 2382.76	0.969 ± 0.050
16540.33	Fe II 2586.65	0.252 ± 0.053
16626.81	Fe II 2600.17	0.945 ± 0.053
17881.27	Mg II 2796.35	4.005 ± 0.054
17927.18	Mg II 2803.53	2.164 ± 0.055
18243.28	Mg I 2852.96	$2.691 \pm 0.057^{\S}$

† Line blended with Fe II $\lambda 2374$ at $z = 3.170$

‡ Line blended with Al III $\lambda 1862$ at $z = 4.523$

§ Line blended with Mg II $\lambda 2797$ at $z = 5.5228$

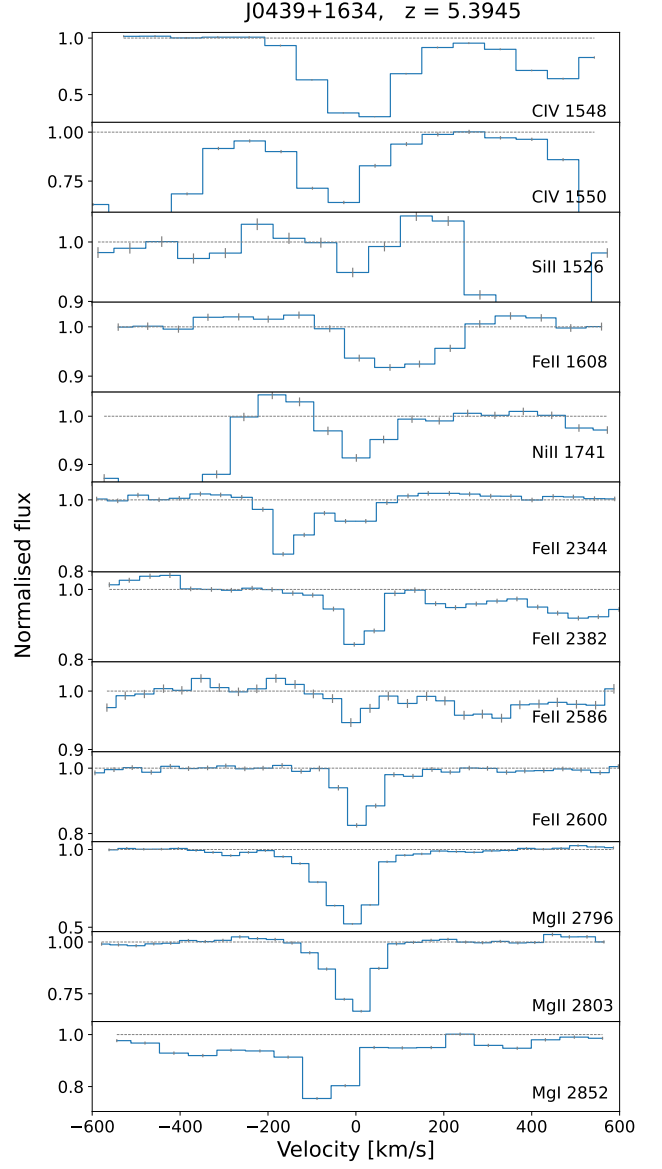


Fig. B.37. Absorption system at $z = 5.3945$ toward J0439+1634.

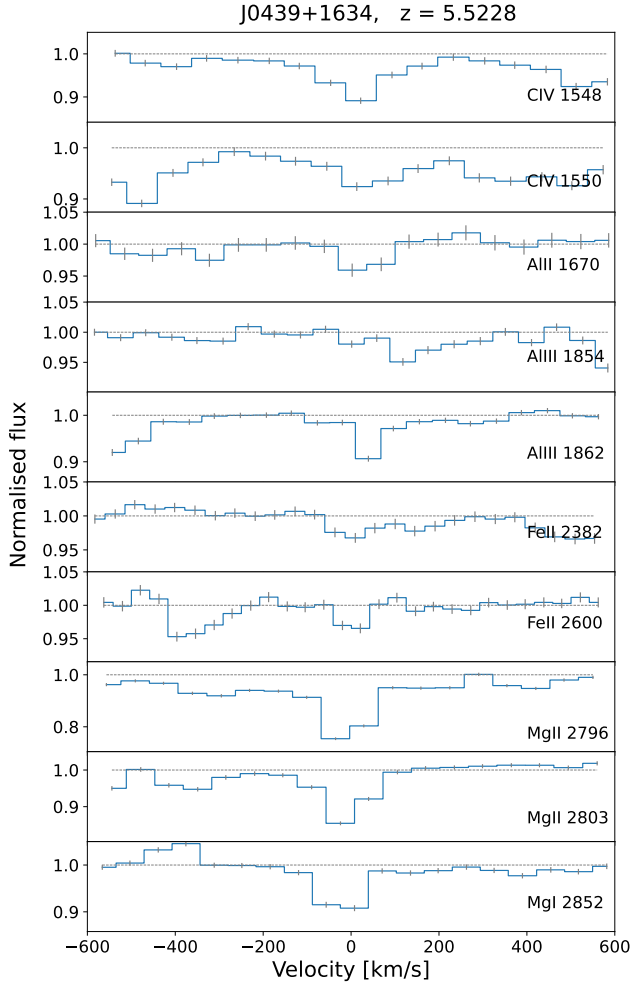


Fig. B.38. Absorption system at $z = 5.5228$ toward J0439+1634.

Table B.38. J0439+1634, $z = 5.5228$

λ_{obs}	ID	W_{obs}
10098.57	C IV 1548.19	0.702 ± 0.043
10115.36	C IV 1550.77	0.612 ± 0.050
10898.21	Al II 1670.79	0.152 ± 0.067
12097.94	Al III 1854.72	0.260 ± 0.039
12150.60	Al III 1862.79	0.380 ± 0.037
15542.30	Fe II 2382.76	0.268 ± 0.052
16960.41	Fe II 2600.17	0.126 ± 0.055
17881.27	Mg II 2796.35	$2.737 \pm 0.057^{\dagger}$
17927.18	Mg II 2803.53	1.131 ± 0.054
18243.28	Mg I 2852.96	0.942 ± 0.061

† Line blended with Mg I $\lambda 2852$ at $z = 5.3945$

Table B.39. J0439+1634, $z = 5.736$

λ_{obs}	ID	W_{obs}
10428.64	C IV 1548.19	0.826 ± 0.037
10445.99	C IV 1550.77	0.496 ± 0.036

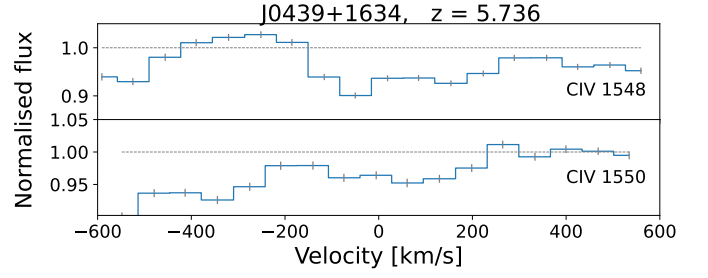


Fig. B.39. Absorption system at $z = 5.736$ toward J0439+1634.

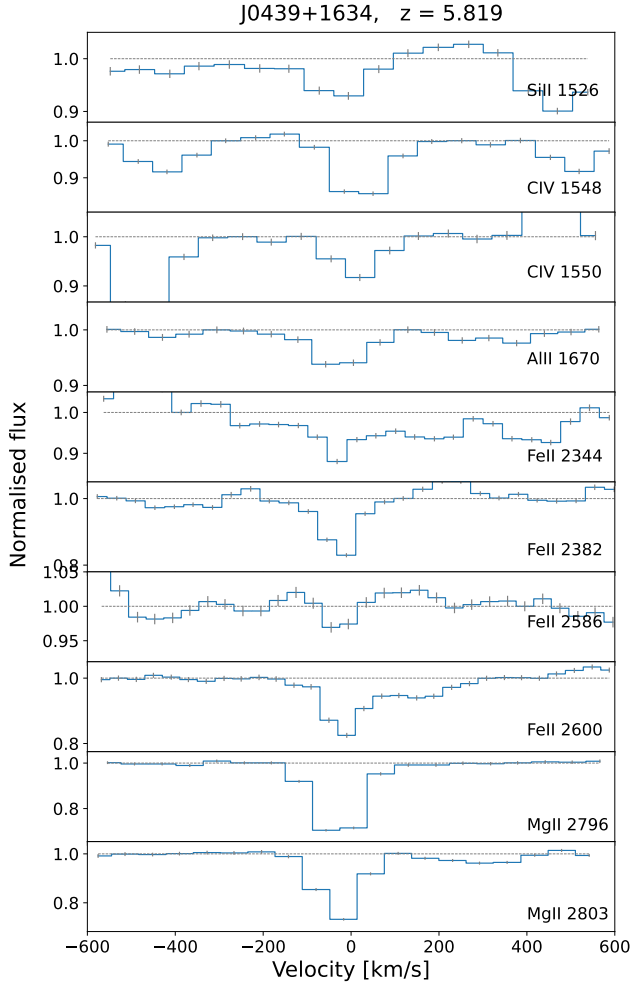


Fig. B.40. Absorption system at $z = 5.819$ toward J0439+1634.

Table B.40. J0439+1634, $z = 5.819$

λ_{obs}	ID	W_{obs}
10410.61	Si II 1526.71	0.323 ± 0.043
10557.14	C IV 1548.19	0.757 ± 0.037
10574.70	C IV 1550.77	$0.387 \pm 0.043^{\dagger}$
11393.10	Al II 1670.79	$0.409 \pm 0.037^{\ddagger}$
15985.20	Fe II 2344.21	1.265 ± 0.047
16248.07	Fe II 2382.76	0.891 ± 0.049
17638.37	Fe II 2586.65	0.220 ± 0.061
17730.58	Fe II 2600.17	1.582 ± 0.061
19068.32	Mg II 2796.35	2.860 ± 0.072
19117.28	Mg II 2803.53	2.062 ± 0.061

[†] Line blended with Si II $\lambda 1526$ at $z = 5.928$

[‡] Line blended with Zn II $\lambda 2062$ at $z = 4.523$

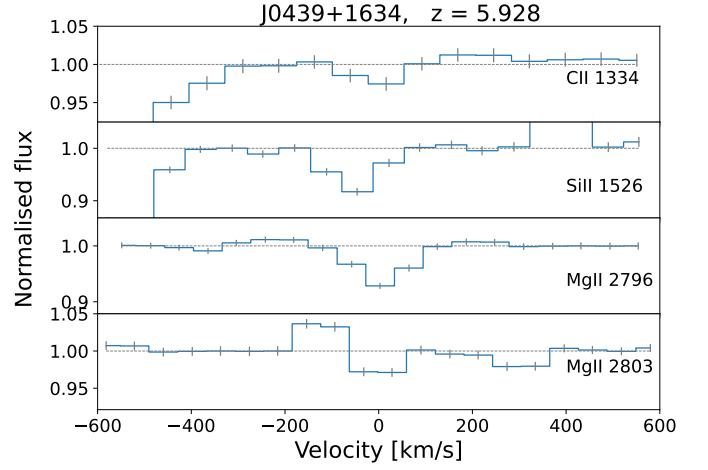


Fig. B.41. Absorption system at $z = 5.928$ toward J0439+1634.

Table B.41. J0439+1634, $z = 5.928$

λ_{obs}	ID	W_{obs}
9245.64	C II 1334.53	0.055 ± 0.047
10577.02	Si II 1526.71	$0.346 \pm 0.044^{\dagger}$
19373.13	Mg II 2796.35	0.518 ± 0.061
19422.86	Mg II 2803.53	0.206 ± 0.042

[†] Line blended with C IV $\lambda 1550$ at $z = 5.819$

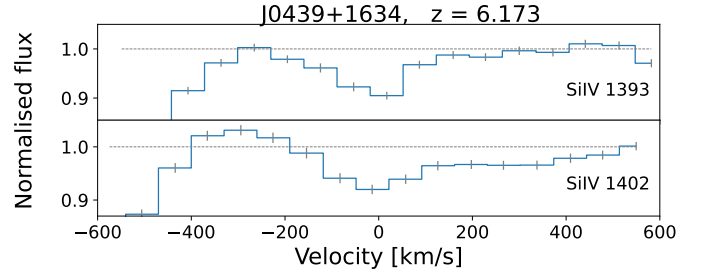


Fig. B.42. Absorption system at $z = 6.173$ toward J0439+1634.

Table B.42. J0439+1634, $z = 6.173$

λ_{obs}	ID	W_{obs}
9997.40	Si IV 1393.76	0.690 ± 0.052
10062.07	Si IV 1402.77	0.617 ± 0.058

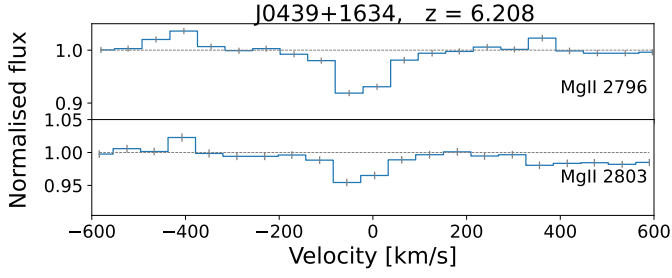


Fig. B.43. Absorption system at $z = 6.208$ toward J0439+1634.

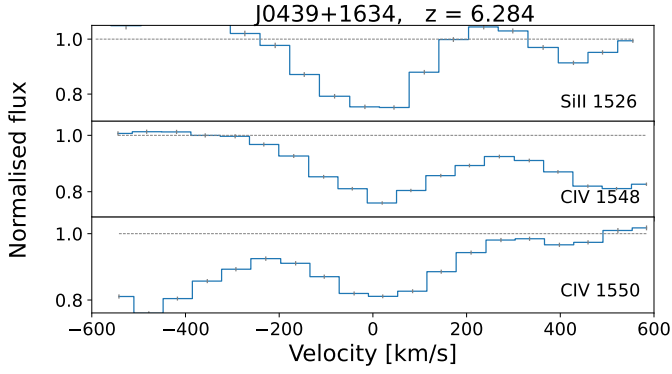


Fig. B.44. Absorption system at $z = 6.284$ toward J0439+1634.

Table B.43. J0439+1634, $z = 6.208$

λ_{obs}	ID	W_{obs}
20156.11	Mg II 2796.35	0.812 ± 0.062
20207.85	Mg II 2803.53	0.434 ± 0.061

Table B.44. J0439+1634, $z = 6.284$

λ_{obs}	ID	W_{obs}
11120.53	Si II 1526.71	2.083 ± 0.066
11277.05	C IV 1548.19	2.843 ± 0.049
11295.81	C IV 1550.77	2.677 ± 0.047

Table B.45. J0439+1634, $z = 6.288$

λ_{obs}	ID	W_{obs}
9188.37	Si II 1260.75	0.444 ± 0.040
9490.20	O I 1302.17	0.864 ± 0.047
9506.25	Si II 1304.37	0.628 ± 0.049
9726.07	C II 1334.53	$1.114 \pm 0.052^{\dagger}$
20379.81	Mg II 2796.35	1.161 ± 0.059

† Blended with C IV 1550 at $z = 5.274$

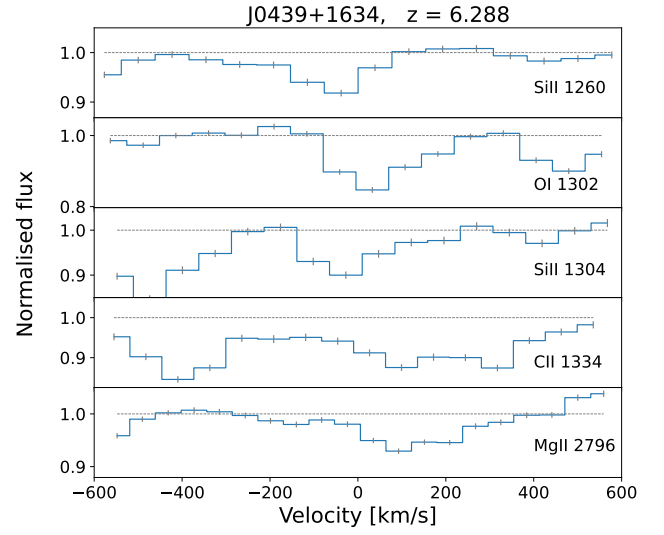


Fig. B.45. Absorption system at $z = 6.288$ toward J0439+1634.

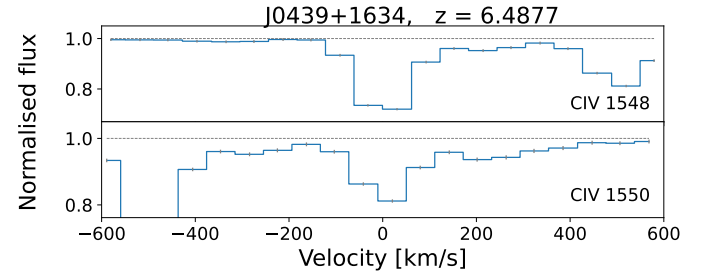


Fig. B.46. Absorption system at $z = 6.4877$ toward J0439+1634.

Table B.46. J0439+1634, $z = 6.4877$

λ_{obs}	ID	W_{obs}
11592.42	C IV 1548.19	1.784 ± 0.030
11611.70	C IV 1550.77	1.206 ± 0.031

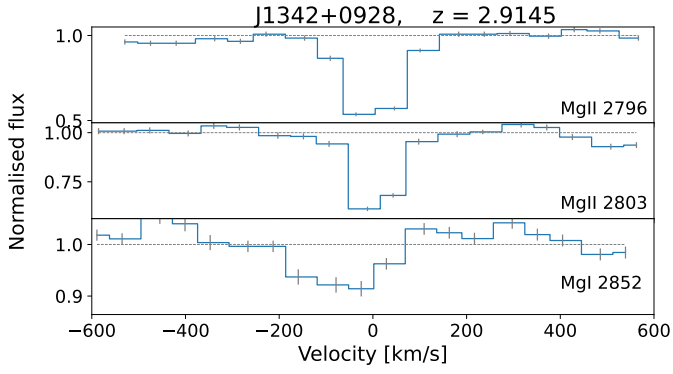


Fig. B.47. Absorption system at $z = 2.9145$ toward J1342+0928.

Table B.47. J1342+0928, $z = 2.9145$

λ_{obs}	ID	W_{obs}
10946.32	Mg II 2796.35	2.797 ± 0.076
10974.42	Mg II 2803.53	1.776 ± 0.084
11167.93	Mg I 2852.96	$0.524 \pm 0.077^{\dagger}$

† Line blended with C II $\lambda 1334$ at $z = 7.368$

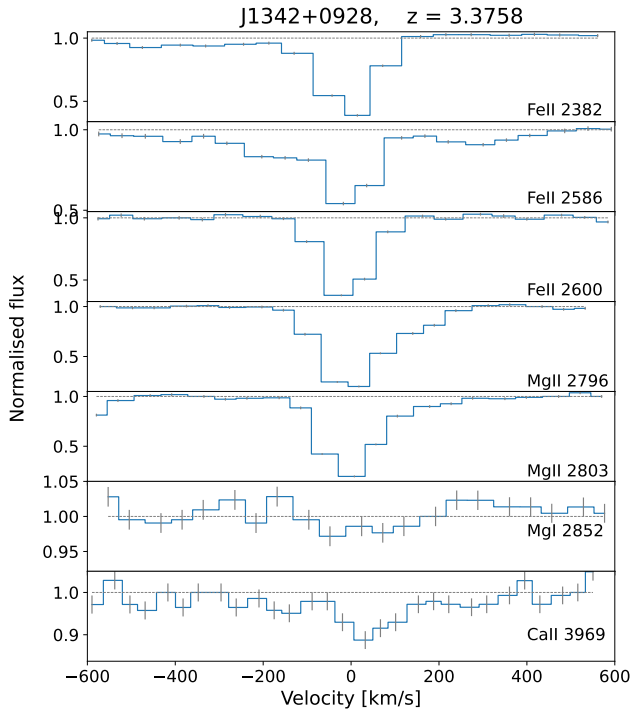


Fig. B.48. Absorption system at $z = 3.3758$ toward J1342+0928.

Table B.48. J1342+0928, $z = 3.3758$

λ_{obs}	ID	W_{obs}
10426.50	Fe II 2382.76	3.166 ± 0.081
11318.66	Fe II 2586.65	3.864 ± 0.081
11377.84	Fe II 2600.17	3.007 ± 0.089
12236.28	Mg II 2796.35	6.490 ± 0.097
12267.69	Mg II 2803.53	5.665 ± 0.102
12484.00	Mg I 2852.96	0.612 ± 0.105
17370.14	Ca II 3969.59	1.520 ± 0.195

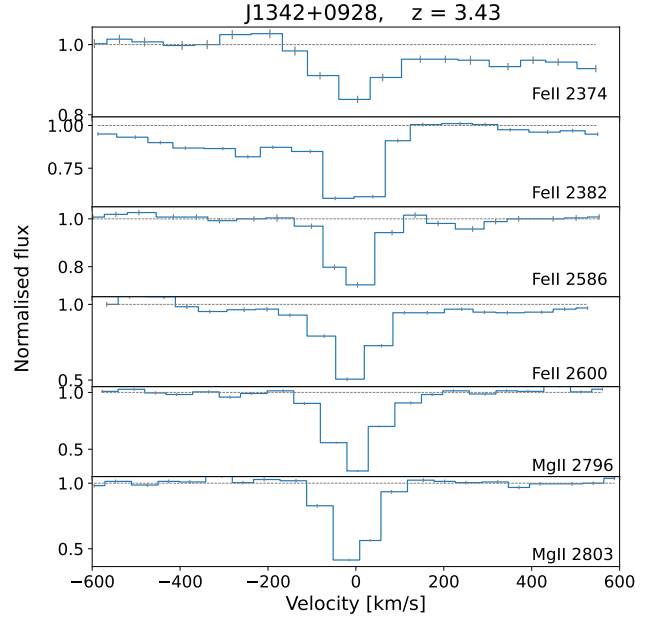


Fig. B.49. Absorption system at $z = 3.430$ toward J1342+0928.

Table B.49. J1342+0928, $z = 3.430$

λ_{obs}	ID	W_{obs}
10518.86	Fe II 2374.46	1.000 ± 0.068
10555.65	Fe II 2382.76	$3.305 \pm 0.074^{\dagger}$
11458.86	Fe II 2586.65	1.424 ± 0.084
11518.77	Fe II 2600.17	3.062 ± 0.084
12387.84	Mg II 2796.35	3.637 ± 0.094
12419.64	Mg II 2803.53	2.563 ± 0.091

† Line partly blended with Si II $\lambda 1260$ at $z = 7.360$

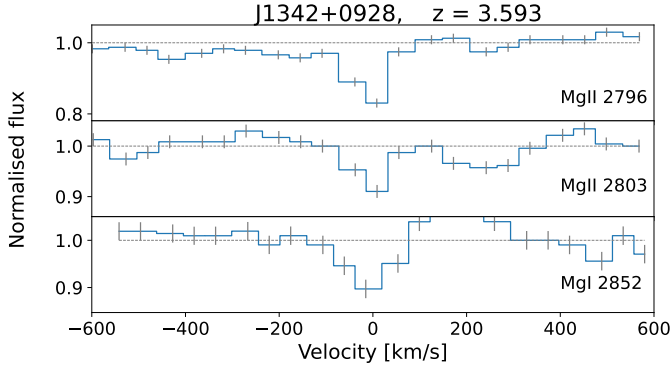


Fig. B.50. Absorption system at $z = 3.593$ toward J1342+0928.

Table B.50. J1342+0928, $z = 3.593$

λ_{obs}	ID	W_{obs}
12843.64	Mg II 2796.35	0.754 ± 0.084
12876.62	Mg II 2803.53	0.397 ± 0.084
13103.66	Mg I 2852.96	$0.336 \pm 0.110^{\dagger}$

† Line blended with Al II $\lambda 1670$ at $z = 6.8427$

Table B.51. J1342+0928, $z = 3.631$

λ_{obs}	ID	W_{obs}
10856.06	Fe II 2344.21	0.260 ± 0.094
10996.13	Fe II 2374.46	0.229 ± 0.091
11034.58	Fe II 2382.76	0.403 ± 0.080
11978.78	Fe II 2586.65	$1.333 \pm 0.090^{\dagger}$
12041.40	Fe II 2600.17	0.422 ± 0.085
12949.91	Mg II 2796.35	2.333 ± 0.087
12983.15	Mg II 2803.53	1.508 ± 0.086
13212.08	Mg I 2852.96	0.475 ± 0.149
18383.18	Ca II 3969.59	3.564 ± 0.268

† Line blended with Si II $\lambda 1526$ at $z = 6.8427$

Table B.52. J1342+0928, $z = 3.6735$

λ_{obs}	ID	W_{obs}
12088.71	Fe II 2586.65	0.675 ± 0.083
12151.91	Fe II 2600.17	0.723 ± 0.086
13068.75	Mg II 2796.35	0.855 ± 0.142
13102.30	Mg II 2803.53	$0.195 \pm 0.134^{\dagger}$
13333.33	Mg I 2852.96	0.797 ± 0.156

† Line blended with Al II $\lambda 1670$ at $z = 6.8427$ and Mg I $\lambda 2852$ at $z = 3.5933$

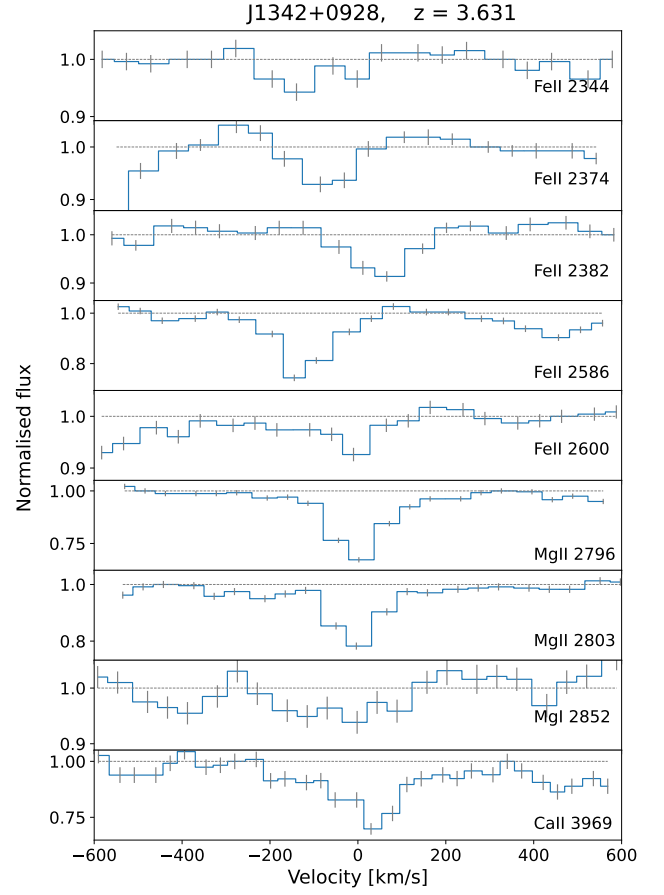


Fig. B.51. Absorption system at $z = 3.631$ toward J1342+0928.

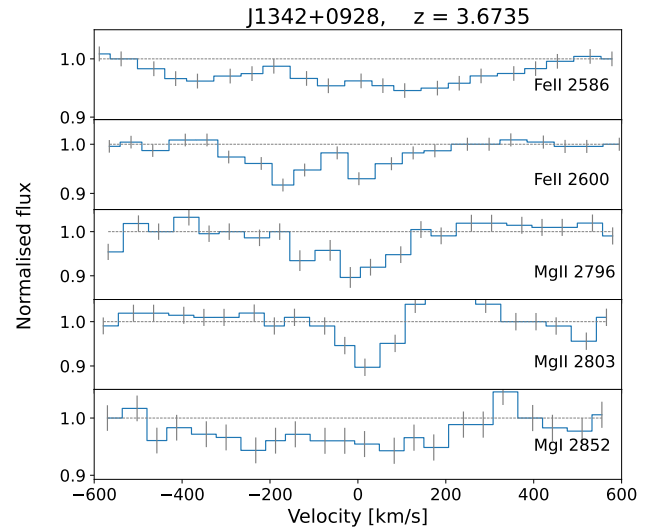


Fig. B.52. Absorption system at $z = 3.6735$ toward J1342+0928.

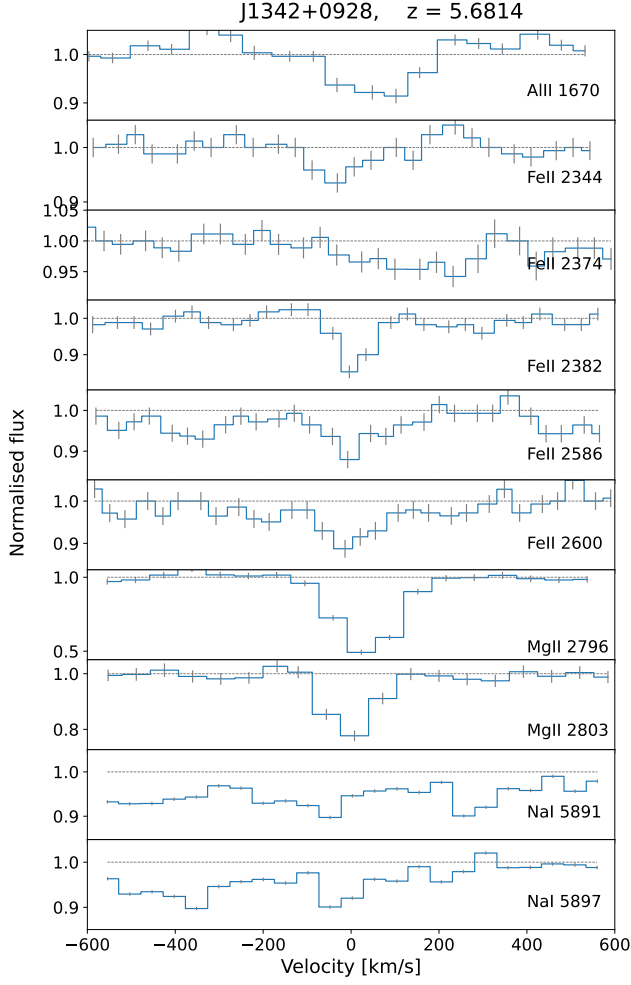


Fig. B.53. Absorption system at $z = 5.6814$ toward J1342+0928.

Table B.53. J1342+0928, $z = 5.6814$

λ_{obs}	ID	W_{obs}
11163.20	Al II 1670.79	$0.644 \pm 0.077^{\dagger}$
15662.63	Fe II 2344.21	0.361 ± 0.126
15864.73	Fe II 2374.46	0.523 ± 0.123
15920.21	Fe II 2382.76	0.559 ± 0.132
17282.44	Fe II 2586.65	1.058 ± 0.152
17372.80	Fe II 2600.17	1.231 ± 0.163
18683.55	Mg II 2796.35	5.253 ± 0.188
18731.51	Mg II 2803.53	1.739 ± 0.196
39362.4	Na I 5891.58	3.301 ± 0.295
39405.3	Na I 5897.56	2.507 ± 0.292

† Line partly blended with C II $\lambda 1334$ at $z = 7.368$

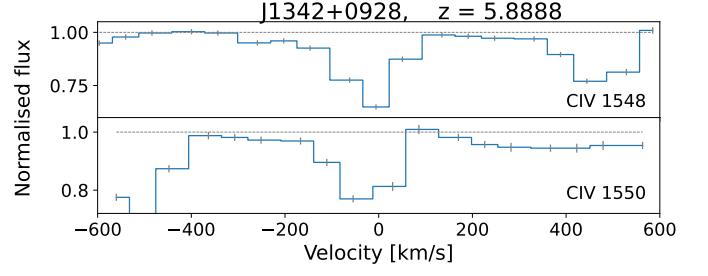


Fig. B.54. Absorption system at $z = 5.8888$ toward J1342+0928.

Table B.54. J1342+0928, $z = 5.8888$

λ_{obs}	ID	W_{obs}
10665.21	C IV 1548.19	1.813 ± 0.072
10682.94	C IV 1550.77	$1.344 \pm 0.079^{\dagger}$

† Line blended with Si II $\lambda 1260$ at $z = 7.476$

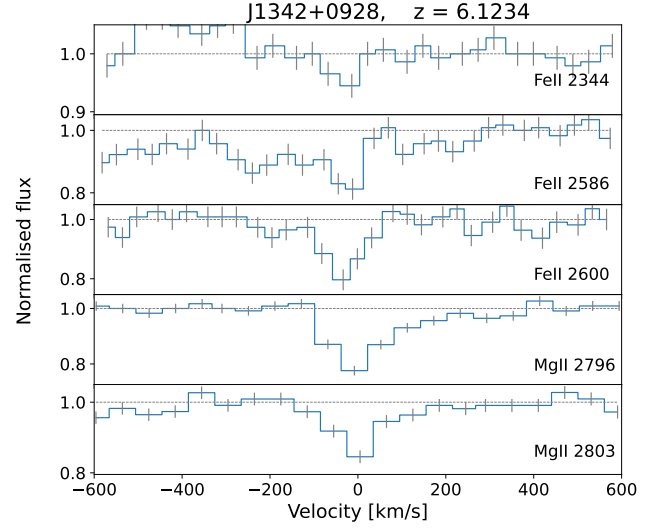


Fig. B.55. Absorption system at $z = 6.1234$ toward J1342+0928.

Table B.55. J1342+0928, $z = 6.1234$

λ_{obs}	ID	W_{obs}
16698.77	Fe II 2344.21	0.200 ± 0.171
18425.74	Fe II 2586.65	2.812 ± 0.300
18522.07	Fe II 2600.17	1.412 ± 0.301
19919.53	Mg II 2796.35	2.390 ± 0.208
19970.67	Mg II 2803.53	1.437 ± 0.212

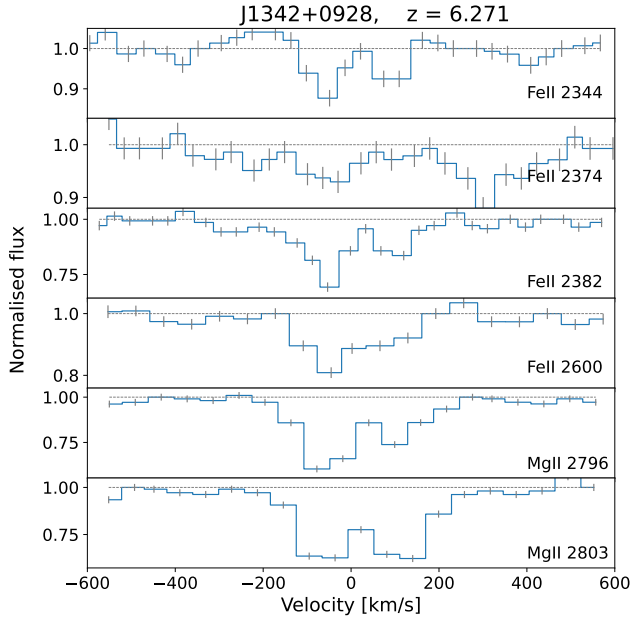

Fig. B.56. Absorption system at $z = 6.271$ toward J1342+0928.

Table B.56. J1342+0928, $z = 6.271$

λ_{obs}	ID	W_{obs}
17044.78	Fe II 2344.21	0.528 ± 0.189
17264.71	Fe II 2374.46	1.160 ± 0.190
17325.08	Fe II 2382.76	3.350 ± 0.197
18905.86	Fe II 2600.17	2.140 ± 0.215
20332.28	Mg II 2796.35	6.020 ± 0.233
20384.47	Mg II 2803.53	$8.021 \pm 0.237^{\dagger}$

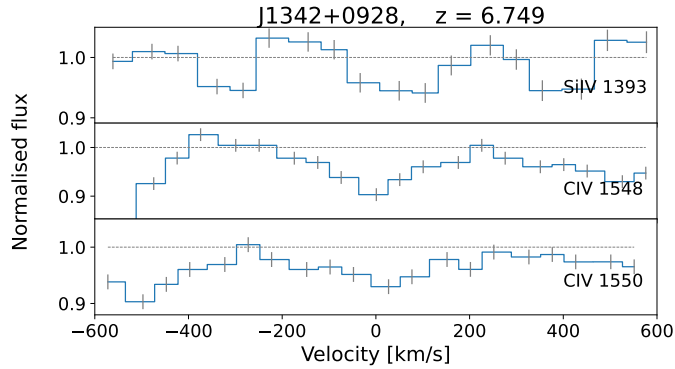
 † Line blended with Fe II $\lambda 2600$ at $z = 6.8427$

Fig. B.57. Absorption system at $z = 6.749$ toward J1342+0928.

Table B.57. J1342+0928, $z = 6.749$

λ_{obs}	ID	W_{obs}
10800.21	Si IV 1393.76	0.316 ± 0.095
11996.96	C IV 1548.19	0.797 ± 0.081
12016.92	C IV 1550.77	0.637 ± 0.077

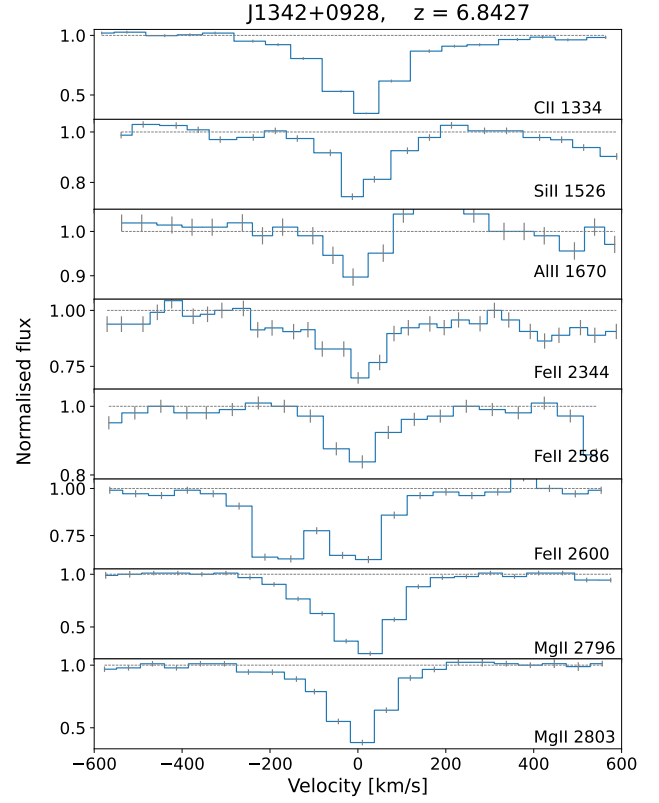

Fig. B.58. Absorption system at $z = 6.8427$ toward J1342+0928.

Table B.58. J1342+0928, $z = 6.8427$

λ_{obs}	ID	W_{obs}
10466.74	C II 1334.53	4.913 ± 0.085
11973.96	Si II 1526.71	$1.458 \pm 0.097^{\dagger}$
13103.98	Al II 1670.79	$0.317 \pm 0.117^{\ddagger}$
18385.67	Fe II 2344.21	3.948 ± 0.318
20287.10	Fe II 2586.65	1.867 ± 0.253
20393.16	Fe II 2600.17	$8.098 \pm 0.238^{\S}$
21931.79	Mg II 2796.35	10.851 ± 0.285
21988.09	Mg II 2803.53	7.690 ± 0.310

 † Line blended with Fe II $\lambda 2586$ at $z = 3.631$
 ‡ Line blended with Mg I $\lambda 2852$ at $z = 3.593$
 § Line blended with Mg II $\lambda 2803$ at $z = 6.271$

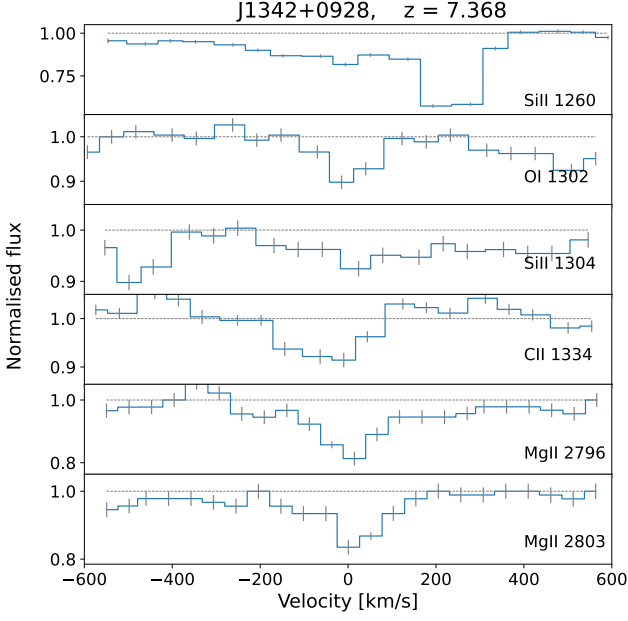


Fig. B.59. Absorption system at $z = 7.368$ toward J1342+0928.

Table B.59. J1342+0928, $z = 7.368$

λ_{obs}	ID	W_{obs}
10547.21	Si II 1260.42	$2.997 \pm 0.066^{\dagger}$
10896.54	O I 1302.17	0.508 ± 0.088
10914.13	Si II 1304.37	0.653 ± 0.088
11167.37	C II 1334.53	$0.531 \pm 0.080^{\ddagger, \S}$
23399.87	Mg II 2796.35	2.851 ± 0.236
23459.95	Mg II 2803.53	2.243 ± 0.220

† Line blended with Mg I 2852 at $z = 2.9145$

‡ Line partly blended with Fe II λ 2382 at $z = 3.430$

§ Line partly blended with Al II λ 1670 at $z = 5.6814$

Table B.60. J1342+0928, $z = 7.443$

λ_{obs}	ID	W_{obs}
10641.74	Si II 1260.42	0.561 ± 0.073
10994.20	O I 1302.17	0.258 ± 0.085
11011.95	Si II 1304.37	0.081 ± 0.076
11267.46	C II 1334.53	0.609 ± 0.077
12889.98	Si II 1526.71	0.154 ± 0.088
13580.15	Fe II 1608.45	1.092 ± 0.136
23609.60	Mg II 2796.35	1.057 ± 0.250
23670.21	Mg II 2803.53	0.524 ± 0.232

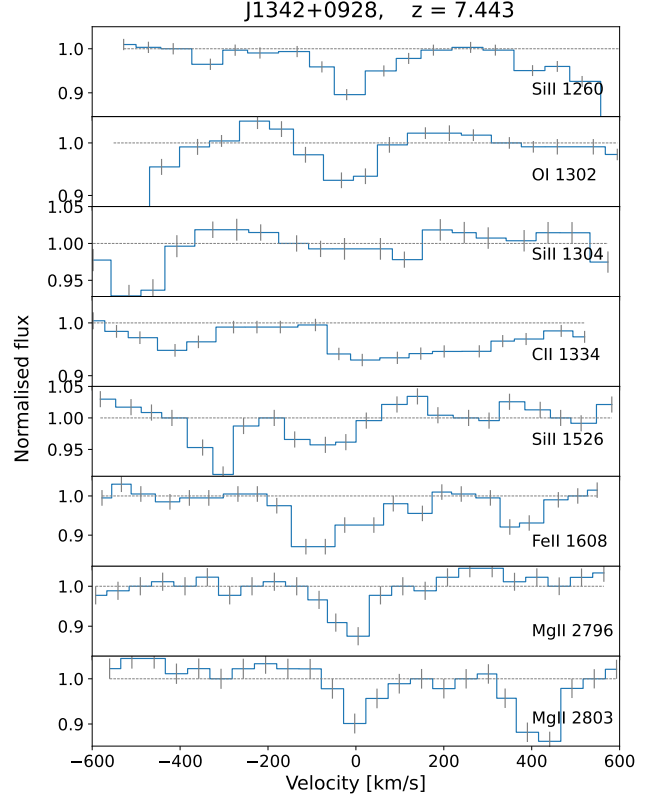


Fig. B.60. Absorption system at $z = 7.443$ toward J1342+0928.

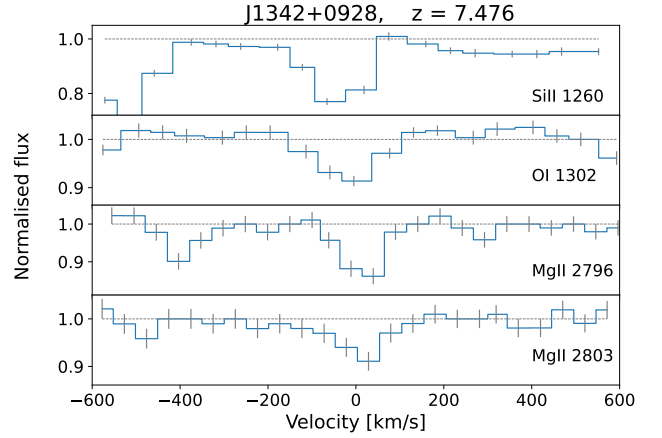


Fig. B.61. Absorption system at $z = 7.476$ toward J1342+0928.

Table B.61. J1342+0928, $z = 7.476^{\dagger}$

λ_{obs}	ID	W_{obs}
10683.34	Si II 1260.42	$1.344 \pm 0.079^{\ddagger}$
11037.18	O I 1302.17	0.378 ± 0.081
23701.88	Mg II 2796.35	1.167 ± 0.235
23762.73	Mg II 2803.53	0.958 ± 0.226

† This absorber lies only $\approx 2000 \text{ km s}^{-1}$ from the quasar systemic redshift, and is considered a proximate system.

‡ Line blended with C IV λ 1550 at $z = 5.8888$